Wind turbine impacts on HF radar ocean surface measurements in Liverpool Bay

Alice Robinson

School of Mathematics and Statistics

The University of Sheffield

A thesis submitted for the degree of

Doctor of Philosophy

November 2013

This thesis is dedicated to my family and friends, without whom it would not have been possible. I give special thanks to my husband for his unwavering support and Lucy Wyatt for never giving up on me.

Acknowledgements

This body of work was undertaken at The University of Sheffield in the School of Mathematics and Statistics. It was made possible through funding from the Natural Environmental Research Council [grant number 14208] and the National Oceanography Centre, Liverpool, formerly the Proudman Oceanographic Laboratory, as well as from the endless help of Seaview Sensing Ltd and Neptune Radar Ltd.

Abstract

This thesis presents results from a series of comparisons between buoy and Acoustic Doppler Current Profiler measurements with the HF radar deployed in Liverpool Bay. They emphasise how current, wind and wave measurements are affected by the presence of the wind farms. The characterisation of the wind turbine interference is assessed and the radar cross section estimated. The modulation frequency within the Doppler spectra is identified. An attempt to mitigate interference effects of the wind farm on the HF radar current and wave measurements is explored and recommendations for dealing with wind turbine interference in a HF radar footprint are made.

Contents

List of Tables

Chapter 1

Introduction

> *The importance of the oceans to the well-being of human society cannot be overstated. We depend on the marine environment to sustain life and support economies; the need to grow our understanding of the oceans' role in climate is ever more urgent.*
>
> Prof. P. Liss, Chair of the National Oceanography Centre Association's Steering Board and Prof. E. Hill, Executive Director, National Oceanography Centre [NOC, 2011a].

In a country founded upon maritime activity and completely surrounded by the sea, never has it been more important to understand the driving forces behind changes to our aquatic environment. This allows informed decisions on policy for coastal monitoring and management. The prediction of coastal waters reduces journey times and increases efficiency and safety in coastal based industries. Numerous bodies exist to protect our invested interest in the coast. The National Oceanography Centre (NOC) is one such organisation. Founded on April 1st 2010, NOC combined two branches of the Natural Environmental Research Council (NERC): 1) the National Oceanography Centre, Liverpool (NOCL), formerly the Proudman Oceanic Laboratory (POL), and 2) the National Oceanography Centre, Southampton (NOCS). Their mission statement and current strategy [NOC, 2011b] reflects regional, national and global policy initiatives on environmental issues. Multi-layered, interdisciplinary problems require inter-agency collaboration. This is an important part of enhancing capability, quality and understanding to achieve their vision of being *"a world leader in the measurement and prediction of changing sea level and the physics of coastal and shelf seas"* [NOC, 2011b].

NOC has collaborated on numerous projects such as the National Marine Monitoring Programme (NMMP) [Cefas, 2004] and WaveNet [Wyatt *et al.*, 2006] both in association with Cefas [Cefas, 2011]. They have a working partnership with the Environment Agency developing the UK's Tide Gauge Network [Rickards, 2001] which itself is part of the Global Sea Level Observing System (GLOSS). They are also part of the Oceans 2025 partnership to understand the interaction between the oceans, atmosphere, sea and land ice and the Earth's crust. This involves working with organisations including the Scottish Association for Marine Science, The Marine Biological Association and the Sea Mammal Research unit. Their aim is to answer the bigger questions on climate change to allow informed preparation, and perhaps mitigation, for the future sustainability of our quality of life.

NOCL research branches into two main programmes: 1) sea level and climate and 2) shelf sea physics, an overview of which is given by NOC [2011b]. Part of NOCL's contribution to understanding shelf sea physics includes operating the Coastal Observatory for Liverpool Bay and the Irish Sea. Liverpool Bay is considered a rich research environment. The region is affected by multiple coastal sea processes with dominant tidal forcing, shallow water depths of less than 50 m and a tidal range which can exceed 10 m [Howarth *et al.*, 2007]. Multiple sensing and measurement techniques, including tide gauges, wave buoys, ferry measurements, X-band radar, high frequency (HF) radar, gliders and more, have been used to collect and record data on numerous oceanic parameters. This is done in as near to real time as possible. One of the key uses of data at NOCL is with the Proudman Oceanographic Laboratory Coastal Ocean Modelling System (POLCOMS), incorporating tides, currents, temperatures, and other conditions. Outputs from POLCOMS and measurement data are combined to assess the response of both physical and biological processes to climate change and anthropogenic influence [Holt & James, 2001]. The effects of climate change on all Earth systems are currently driving scientific and environmental research and influencing the development of government policy worldwide. The comprehension of such large scale problems relies heavily on the amalgamation of smaller research experiments. This project focuses on the reliability and validity of measurements made with the HF radar deployed as part of the Liverpool Bay Coastal Observatory.

Ocean measurements have historically been taken in situ with instruments such as wave buoys, current meters, pressure gauges and the manual reading and recording of staff gauges. These instruments, although useful and well established, were limiting in developing the understanding of coastal dynamics as they only provide a single point temporal observation. Measurements of this nature continue today [Graber *et al.*, 1997; Woodworth & Smith, 2003] however it can prove logistically challenging to deploy and operate such scientific equipment. Regions of interest frequently experience hostile environmental conditions and as such measurement concentration has traditionally been heavily localised to the near-shore. This was revolutionised by the advent of remote monitoring and sensing. It was Crombie [1955] who first identified coherent scattering of electromagnetic (EM) waves off the ocean surface, attributed to waves of half the transmit wavelength. This first-order scattering mechanism was shown to give reasonable estimates of current and wind direction measurements. Later second-order scattering effects were linked to the general sea state and the theory for wave measurement. A formal introduction to the field of oceanography was achieved by Barrick [1972a,b, 1973] using radars developed within the National Oceanic and Atmospheric Administration (NOAA) throughout the 1970's. HF radar, $3-30$ MHz, for measuring ocean currents is now in common practice and has continued to develop allowing large regions of coastal ocean to be simultaneously and continuously observed. HF radar has enabled maps of near-surface currents, of the type shown in figure 1.1, as well as wind directions, wave heights and associated spectra to allow us to understand large scale coastal dynamics [Crombie, 1971; Haus *et al.*, 1997; Paduan & Graber, 1997; Ward, 1969; Wyatt, 2002, 2006; Wyatt & Green, 2009; Wyatt *et al.*, 2003, 2006, 2011]. Wave measurements are currently a less frequently pursued area of continuous development and research.

Radar oceanography has emerged as the worldwide field of study utilising radar systems to remotely observe oceanographic parameters. It has been embraced due to its continuous, non-invasive, shore-based nature. Easy access allows for maintenance at a relatively low cost with reduced risk and no disturbance of the system it is observing [Trinza & Jensen, 1997]. Many military and civilian applications of radar oceanography exist today. These range from commercial harbours [Helzel *et al.*, 2010], shipping [Dzvonkovskaya *et al.*, 2009], coastal erosion, sediment and pollution transport studies, search and rescue [Valentin *et al.*, 2010] and inclusion in national monitoring programmes such as WaveNet [Wyatt *et al.*, 2006]. Applications are expanding as systems become more adaptive and allow for rapid deployment. Recently oil disasters have brought HF radar into the limelight proving valuable to oil spill containment where the mapping of currents and model assimilation allows for targeted, more effective, operational efforts [Abascal *et al.*, 2009; Kjelaas & Whelan, 2011; Mariano *et al.*, 2011; Valentin *et al.*, 2010].

The Liverpool Bay HF radar system, operational from March 2004 to December 2011, used a HF WERA radar consisting of two sites, Llanddulas and Formby, shown on figure 1.1. Each site included a transmit antenna and a phased array

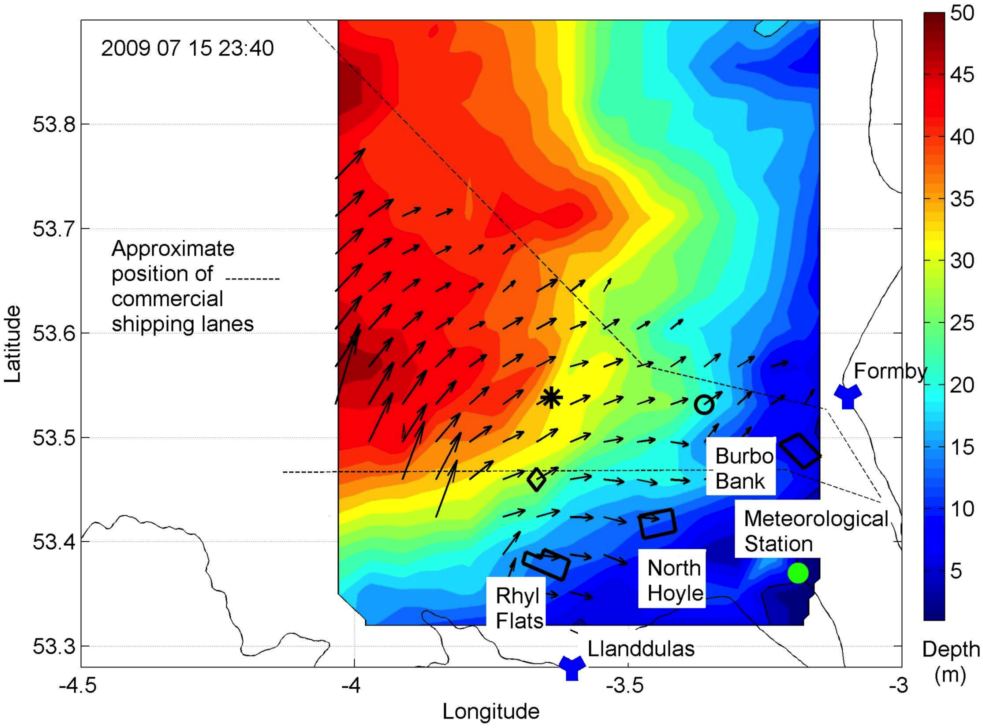

Figure 1.1: A surface current vector map generated using HF radar data from Liverpool Bay, July 15th 2009 23 : 40. Features include two HF radar sites, Llanddulas and Formby, and Hilbre Island Meteorological Station. The co-location of radar cell 234, the wave buoy and Acoustic Doppler Current Profiler (ADCP) A is indicated with the symbol 'o'. The $\diamond$ represents radar cell 136 and the position of ADCP B in 2009. Location $*$ marks ADCP B in 2010. The background colour map displays bathymetry data as the average depth in meters above the sea floor. North Hoyle, Burbo Bank, and Rhyl Flats wind farms are also indicated.

receive antenna, see figure 1.2. The HF WERA radar provided surface current, wind and wave measurements from Liverpool Bay and the Irish sea covering an area up to 1600 km^2 every 20 minutes. Operating at different frequencies, just offset from 13 MHz, allowed simultaneous data acquisition from each radar.

This thesis aims to provide a review of the operational performance of the HF radar deployed in Liverpool Bay. Different aspects of the radar's ability to deliver data consistently and accurately are assessed. At each stage a specific focus on how the presence of wind turbines within a measurement cell affects its capability is considered. The Liverpool Bay region has seen extensive wind farm development over the last decade. This presents an increasing challenge to delivering high quality reliable current and wave measurements with the radar. There are currently three operational wind farms in Liverpool Bay, North Hoyle (NHWF), Burbo Bank

Figure 1.2: HF WERA radar 16 antenna linear receive array at Formby (March 2010).

(BBWF) and Rhyl Flats (RFWF). Their position relative to the radar can be seen in figure 1.1. Within the radar footprint NOCL maintains 3 in situ measurement devices. These are two bed-mounted 600 kHz Acoustic Doppler Current Profilers (ADCPs) and a Waverider Buoy, as shown on figure 1.1. This allows several comparative checks to be made on the HF WERA radar current and wave measurements. Current measurements are compared at both NHWF and RFWF with ADCP measurements and wave measurements from RFWF with those of the buoy, a common practice for radar evaluation.

To enable meaningful assessment, principles of radar are discussed. HF radar, as a remote ocean sensing tool for measuring currents and waves, is reviewed in chapter 2 and the WERA radar data processing considered in detail in chapter 3. System noise, data availability and frequency of operation were assessed during various operational conditions to establish performance expectations, the results from which are presented in chapter 5.

Tidal dominance in Liverpool Bay is confirmed using tidal analysis and comparing the amplitude and phase measurements obtained using HF WERA radar and ADCP data. It is shown in chapter 6 that a large percentage of any current measurement can be accounted for by specific tidal frequencies and their associated amplitude and phase. There is also shown to be excellent agreement between parameters obtained using ADCP and HF WERA radar.

The accuracy of the HF radar when extracting ocean parameters in the vicinity of the wind farm is assessed. Quantification of performance due to such features such as the cell locations, radar operating frequency and wind turbine radar cross section are investigated in developing a clear picture of the HF radar capability. A focus is made on two of the wind farms, NHWF and RFWF. BBWF, shown in figure 1.3, from the Formby receive antenna, has not been assessed in any detail as the region is outside the operational parameters of the HF radar.

NHWF is the oldest wind farm in Liverpool Bay, operational since before the HF radar installation. It lies at the edge of the coverage area and roughly along line of sight between the radars. The location of NHWF is shown by Robinson *et al.* [2011] to introduce significant errors when resolving for vector currents or extracting wave parameters regardless of the wind turbine presence. This results in the wind farm impacts being more difficult to distinguish. This is discussed in detail in chapter 7 and has been presented by Robinson *et al.* [2011].

RFWF was the third offshore wind farm to become operational in Liverpool Bay. Construction began in 2007 and the official opening of RFWF was in December 2009. Robinson *et al.* [2013] utilise this opportunity to gain an understanding of radar performance and measurement accuracy before and after installation at the co-located HF radar measurement cells, and this is presented in chapter 8.

Figure 1.3: An ocean view from the Formby receive antenna showing Burbo Bank wind farm on the horizon (March 2010).

Current government policy will promote continued wind turbine development in Liverpool Bay. A planned extension of BBWF is under consultation and the Gwynt y Môr (GYMWF) wind farm, due to be fully operational by 2015, is currently being constructed. GYMWF will have a capacity 10 times that of NHWF with 160 turbines in an area of 79 km^2 dwarfing the preceding wind farms in Liverpool Bay. This will be a significant problem for the future availability of HF radar data in the region.

As with any radar system, challenges arise in being able to select backscatter from what you want to observe, the target, and dismiss backscatter from things you don't, clutter. Examples of clutter to the HF radar in Liverpool Bay are wind turbines, which strongly influence backscatter signals in any radar system. This is a well researched problem at the gigahertz frequencies used by aviation [Butler, 2003; Christiansen & Hasager, 2005; Kent *et al.*, 2008]. Studies specific to HF radar have also been carried out [Riddolls, 2005] and some assessment within Liverpool Bay has focused on the effects to communication and navigation [Howard & Brown, 2004].

This thesis is the first study that has assessed the impact of wind farms on oceanographic HF radar systems. Wind turbine interference (WTI) is discussed in chapter 9 where Doppler spectra from RFWF are used to determine amplitudes attributed to the blade rotations. A comparison is then made of current and wave measurements prior to and after WTI reduction.

Chapter 2

HF radar remote ocean sensing

This chapter considers the development of HF radar measurement tools in the field of oceanography. The operational and measurement principles of radar are first discussed. A general characterisation of clutter and an object's radar cross section (RCS) is given along with a detailed description of an approximation for the RCS of a wind turbine, the focus of clutter mitigation in later chapters. The definition of noise is considered in the broad sense and then specifically how it is determined from HF radar Doppler spectra. The first and second-order radar spectral cross sections are presented within the context of HF radar theory development for measuring ocean currents and waves.

2.1 Radar

An early pioneer, R. A. Watson-Watt, is credited for laying out the basic principles of RAdio Detection And Ranging, or radar, in an unpublished memorandum which is summarised by Austin [1999]. Radar was developed in the mid 1930's for military applications. It is now fundamental to shipping, aviation and missile operations, including detection and tracking. Civil applications include shipping, aviation, environmental remote sensing, law enforcement, communication and much more.

Radar operation is categorised into bands of different frequencies specific to the use, details of which can be found in any book on radar. Specific radar systems vary considerably in complexity, however the basic radar principles, as summarised in figure 2.1, are fairly straightforward.

Radar is based on the transmission of an EM wave at a known radio frequency, f, from a transmit antenna, T. These waves are scattered, or absorbed and re-radiated,

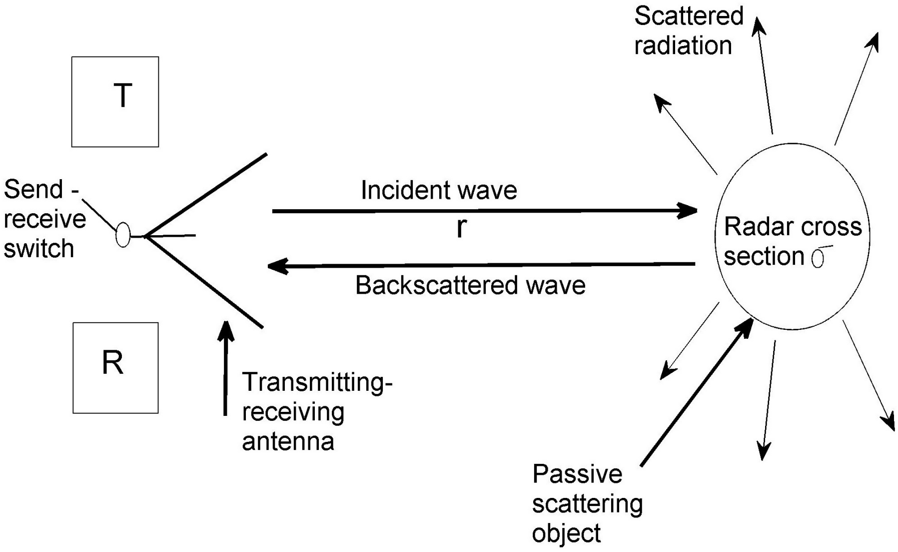

Figure 2.1: A two-way radar path, adapted from Kraus & Fleisch [1999]. T and R are the transmit and receive antenna, respectively and r is the distance from the radar to the scattering object.

by objects in their path at distances r from the radar, as illustrated in figure 2.1. Some of the signal will reach a receive antenna, R. When T and R are co-located this part of the echo is called backscatter. For pulse radars the time delay between transmitting and receiving the signal, t, can be used to determine the distance r as r $= 0.5ct$ where c is the speed of light. Any relative velocity of the object, v, is evident in the presence of Doppler frequency shift, δf, in the backscattered signal, given by Young & Freedman [2000] as

$$\frac{\delta f}{f} = \frac{v}{c} \tag{2.1}$$

For frequency modulated radars, like CODAR [Barrick *et al.*, 1977], WERA [Gurgel *et al.*, 1999a] and Pisces [Shearman & Moorhead, 1988], range is determined from frequency differences in the received signal. Using geometry and direction of the backscatter the location of the object can be determined. Simple systems may have rotating antenna where the bearing angle of objects relative to the radar can be determined from the directivity of the radar beam itself and the direction of the radar when receiving. More complicated, multi-antenna, phased array systems will use processes like beamforming, outlined in chapter 3, or direction finding to determine direction.

Optimum radar design is specific to its purpose and is a balance of several operational parameters. These are summarised by the radar range equation, a version of which can be found in Skolnik [1990] and is given by equation 2.2.

$$R_{max}^4 = \frac{P_t G_t^2 \lambda^2 \sigma}{(4\pi)^3 S_{min}} \tag{2.2}$$

where ...

- R_{max} = maximum radar range
- P_t = power of pulse transmitted by the radar
- S_{min} = minimum detectable signal
- G_t = antenna gain
- λ = transmitting wavelength
- σ = the radar cross section (RCS)

Maximum range, R_{max}, and minimum detectable signal, S_{min}, are key defining characteristics of a radar's capabilities. The power of the transmitted pulse, P_t, wavelength, λ, and the antenna gain, G_t, are determined by the radar configuration and are generally fixed during operation. This leaves the RCS, σ, described by equation 2.3, as the most variable and unpredictable parameter.

2.2 Radar Cross Section

The RCS is a property of the interacting object or 'target'. It is a highly variable parameter depending on the radar operating frequency and it is an important measure in determining radar capabilities. A physical interpretation, as given by Butler [2003], is

$$RCS(\sigma) = Geometric\ size\ x\ Reflectivity\ x\ Directivity \tag{2.3}$$

where ...

- Geometric size is the area presented to the radar
- Reflectivity is an efficiency measure of the reflected energy to incident energy
- Directivity is the direction in which energy is reflected

RCS is regarded as giving a measure of an object's visibility to radar and can be difficult to calculate except for very specific shapes. The simplest example is a sphere. This presents the same geometric size from whichever angle it is viewed and the directivity is assumed equal in all directions. This is easier for modelling purposes as the RCS may depends only on the reflectivity, a property of the material and surface texture. An approach to defining the RCS based on this idea is given by Skolnik [1990] where the RCS is defined as

$$\sigma = \lim[R \rightarrow \infty] 4\pi R^2 \frac{|E_s|}{|E_0|} \tag{2.4}$$

where R is the target to antenna range, E_s is the scattered electric field strength at the radar and E_0 is the incident electric field strength. For highly complex objects such as aircraft the RCS can be modelled at the small scale or measured at full scale in an anechoic chamber [L. Zhang, 2010; Tice, 1990]. More typically the RCS is modelled by computer or by breaking down an object into several simpler shapes with known RCS values. In practice the efficiency of the scattered to incident power for a unit area is more commonly used [Dybdal, 1987; Kraus & Fleisch, 1999], rather than detailed modelling for complex shapes, as it can be easily measured. This interpretation of the RCS expressed in decibels is also referred to as the electromagnetic scattering coefficient [Jones *et al.*, 1997] or normalised RCS (NRCS) [Gommenginger *et al.*, 2000; Power & Randell, 1999]. It is related to 2.4 using Poynting's theorem that relates the power density to the electric and magnetic fields. For a full mathematical discussion on the radar cross section the reader is directed to Skolnik [1990] chapter 11.

2.3 Clutter

Clutter is a radar term encompassing any signal returns to the radar not from the desired object of interest. The extent to which any clutter will degrade the desired measurement is highly dependent on its RCS, what is being measured and the radar it is being measured with.

Clutter can come from a number of sources and can either be fixed or dynamic with respect to time. Common examples include radio frequency interference (RFI) from nearby radio transmissions, ionospheric propagations, stationary returns from land and buildings, flocking birds, ships and wind turbine interference (WTI). Figure 2.2 shows the view from the Liverpool Bay Coastal Observatory Formby radar to be a particularly clutter-laden picture on occasions with flocking birds, land, wind turbines and a ship in clear view.

Figure 2.2: A view from the Liverpool Bay Coastal Observatory Formby radar showing multiple clutter sources (March 2010).

What is clutter to one system will often be the object of interest to another. This results in clutter mitigation being as specific as the problem itself. Different approaches are used in different industries and applications vary in complexity depending on the relative movement of the clutter and object. One example is the Doppler frequency shift caused by the rotation of the tip of a turbine blade as measured by aviation radar. This will cause a frequency shift associated with a speed of 400 m/s, similar to the speeds of approaching aircraft. Having a knowledge of the physical situation can then narrow down processing validity as an object moving at 400 m/s that never changes location is clearly not an aircraft. In aviation this is easily removed using a process referred to in the industry as Moving Target Indicator (MTI) [Skolnik, 1990].

2.4 The Radar Cross Section of a Wind Turbine

To fully describe the effect clutter will have on a radar system it is then important to understand the RCS presented by the clutter. As the main clutter sources investigated in later chapters are wind turbines a mathematical description of their RCS is given here.

A typical wind turbine, as shown in figure 2.3, is constructed of three main components, the rotator hub or nacelle, blades, and the support tower. Varying backscatter signals can be expected from each component. Materials, shape, nominal operating speed and orientation of the blades will combine to give the wind turbine RCS. The tower, typically made of steel, will dominate the stationary return from the combined backscatter of the nacelle and tower where overloading of the receive antenna can occur if the power of the backscatter is too high.

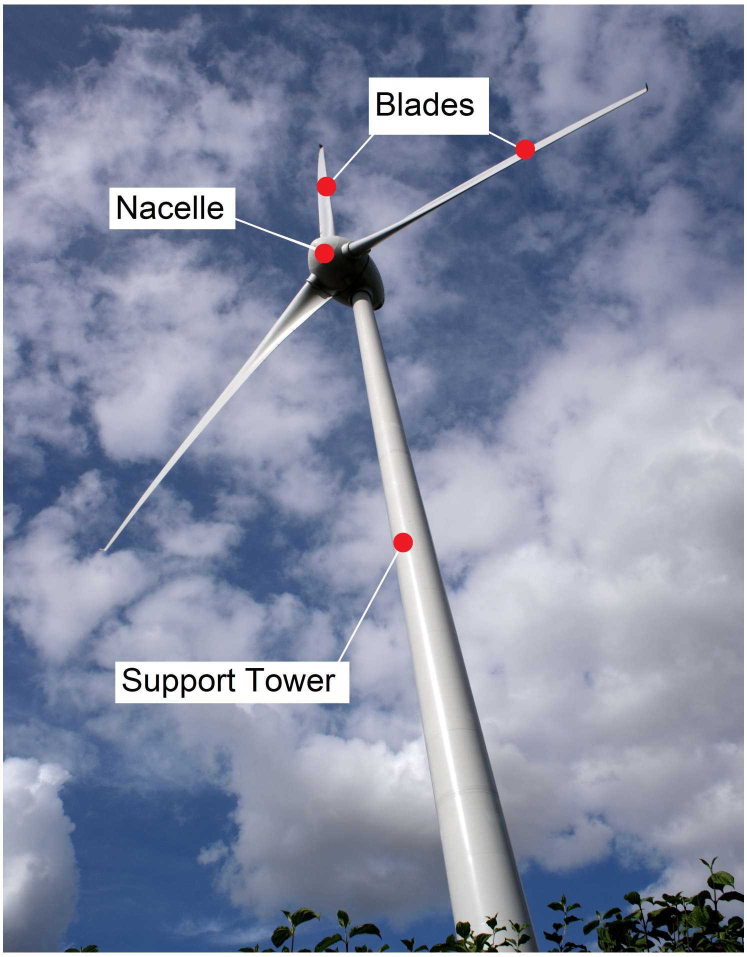

Figure 2.3: A typical wind turbine.

The blades are made from lightweight materials, for example fibreglass. Their construction is hollow with thin tips, wide base and a lightning conductor running the length of the blade. Blade speed varies anywhere from 0 m/s at the nacelle to 80 m/s at the tip. Frequency shifts associated with these speeds will also vary accordingly. Butler [2003] found at gigahertz frequencies blade rotation also imposes a modulation on the signal and results in possible spreading in frequency of the power spectra.

The wind turbine RCS estimate can be made by treating the structure as a combination of cylinders of different sizes. By considering an incident plane wave polarised along the cylinder axis Riddolls [2005] shows that the scattering electric field, E_s, for a thin highly conducting cylinder (an approximation for the lightning conductor) of length L and radius a at distance r from the transmit radar is

$$\mathbf{E}_s \approx -\hat{\theta}\frac{ELe^{ikr}\mathsf{sinc}(\delta)\sin(\theta)}{2rlog(\gamma ka/2)} \tag{2.5}$$

where $\gamma = 1.7810$, k is the free space wavenumber, θ is the aspect angle, $\hat{\theta}$ is the unit vector in the direction of θ and $\delta = (kL/2)\cos(\theta)$.

For the case of a thin dielectric cylinder (an approximation for the tower and blade) Riddolls [2005] also shows the scattering electric field to be given by

$$\mathbf{E}_s \approx -\hat{\theta}\frac{EL(ka)^2(N^2-1)e^{ikr}\mathsf{sinc}(\delta)\sin(\theta)}{4r} \tag{2.6}$$

where N is the dielectric refractive index. Substitution of equation 2.5 into equation 2.4 and taking $|E_0| = E$ the RCS of the thin highly conducting cylinder is then

$$\sigma(\theta) = \frac{\pi L^2\mathsf{sinc}^2(\delta)\sin^2(\theta)}{log^2(\gamma ka/2)} \tag{2.7}$$

For the RCS of the dielectric cylinder we can substitute equation 2.6 into equation 2.4, again taking $|E_0| = E$, to get

$$\sigma(\theta) = \frac{\pi L^2(ka)^4(N^2-1)^2\mathsf{sinc}^2(\delta)\sin^2(\theta)}{4} \tag{2.8}$$

The angular velocity and direction of turbine blades results in a time-varying RCS. Both the RCS of the highly conducting and dielectric cylinders is proportional to $sin^2(\theta)$ which has two maxima within one 2π rotation at $\theta = \pi/2$ and $\theta = 3\pi/2$, or every 180^o. For 3 blades, which align themselves normal to the electric field 6 times during one rotation, this maximum would then be expected every 60^o of one full rotation. We can combine the response of the 3 blades in the time domain using equations 2.7 and 2.8 assuming a constant angular velocity $\theta(t)$ to get

$$\sigma(t) = \sum_{i=1}^{3} \frac{\pi L^2 \sin^2(\theta(t)+\alpha_i)}{log^2(\gamma ka/2)} \left[\frac{\sin(\frac{kL}{2}\cos(\theta(t)+\alpha_i))}{\frac{kL}{2}\cos(\theta(t)+\alpha_i)} \right]^2 \tag{2.9}$$

$$\sigma(t) = \sum_{i=1}^{3} \frac{\pi L^2 (ka)^4 (N^2-1)^2 \sin^2(\theta(t)+\alpha_i))}{4} \left[\frac{\sin(\frac{kL}{2}\cos(\theta(t)+\alpha_i))}{\frac{kL}{2}\cos(\theta(t)+\alpha_i)} \right]^2 \tag{2.10}$$

where the angular offset α_i is described by Tennant & Chanbers [2006] as ($\alpha_0 = \frac{-2\pi}{3}$ $\alpha_2 = 0$ and $\alpha_0 = \frac{2\pi}{3}$). This description of the time varying RCS is used later in chapter 9 to estimate the RCS of the different wind turbines in Liverpool Bay.

2.5 Noise

Like clutter, noise is an unwanted influence on the backscatter signal possibly perturbing the desired measurements from the target object. A white Gaussian noise distribution is often used to model two dominant forms, thermal and vibrational noise. Electrical circuitry is a source of thermal noise and requires some active cooling to maintain a consistent minimum level. In radio telescopes where the desired signal is particularly low, liquid nitrogen is used to minimise thermal noise. Small vibrations in the earth will cause noise to be introduced to the radar system which may come, for example, from traffic sources, train tracks, mining works and seismic tremors. Electromagnetic interference from unknown outside sources is also classified in this way.

Noise is particularly noticeable when the strength of the backscatter signal is low. Below a certain spectral power density the spectrum will become dominated by system noise. Hildebrand & Sekhon [1974] refer to this as the noise threshold and it is the point where the backscatter signal strength has just fallen below the minimum detectable signal, S_{min}.

Several approaches have been applied to determine the precise noise threshold within the HF radar Doppler spectra. A set increment below the spectral peak is among the most operationally simplistic but easily introduces measurement errors [Hildebrand & Sekhon, 1974]. Hildebrand & Sekhon [1974] obtains reasonable results through applying a more sophisticated method to weather radar spectra that makes use of the properties of white Gaussian noise. Heron & Heron [2001] successfully use a cumulative probability of ranked HF radar spectral data which enables the identification of contributions to the spectrum arising from different sources. What is particularly evident is where a spectrum deviates from a white Gaussian noise distribution allowing for subtraction prior to processing for ocean measurements. However to achieve the desirable real-time processing a specific location in the ranked Doppler spectrum can be an effective approximation. As discussed in detail in chapter 5, establishing the signal to noise ratio is a common approach of data quality to sift out processable data.

2.6 HF radar

Over the past 50 years HF ($3-30$ MHz) radar has become a well proven and researched tool for measuring ocean surface parameters with excellent spatial and temporal resolution. Ocean surface spectral analysis was however first put to regular use as far back as 1945. The Admiralty Research Laboratory developed one of the early examples of an analyser utilised in processing wave motion records taken near Lands End [Barber *et al.*, 1945]. Based on a 'ticker-tape' design it was capable of producing up to 15 frequency spectra a day, a very small number relative to capability today.

Early experimental observation by Crombie [1955] first identified wave features in frequency spectra of vertically polarised 13 MHz HF radar ocean backscatter. Crombie [1955], accredited with the 'birth' of HF radar, showed resonant coherent backscatter from ocean wave trains resulted from waves of half the radar transmitting wavelength, λ_T, with the sea acting as a diffraction grating. This scattering mechanism, which Barrick [1972a] later confirmed theoretically (see equation 2.26), is referred to as Bragg scattering.

The frequency spectra of the backscatter signal, also called Doppler spectra, an example of which is shown in figure 2.4, are a representation of the average energy of returned scatter at different frequencies. Due to coherent scattering at the Bragg wavelength λ_b, where $\lambda_b = 0.5\lambda_T$, a modulation of the backscattered signal occurs from first-order scattering mechanisms. This results in a large Doppler spectrum amplitude.

In the absence of any current these relatively high amplitude peaks are present in the Doppler spectra at a precise frequency. This is referred to as the Bragg frequency ($\pm\ \omega_b$ rads/s) as given by equation 2.11. This shows what is referred to as the dispersion relationship and connects wavenumber with angular frequency.

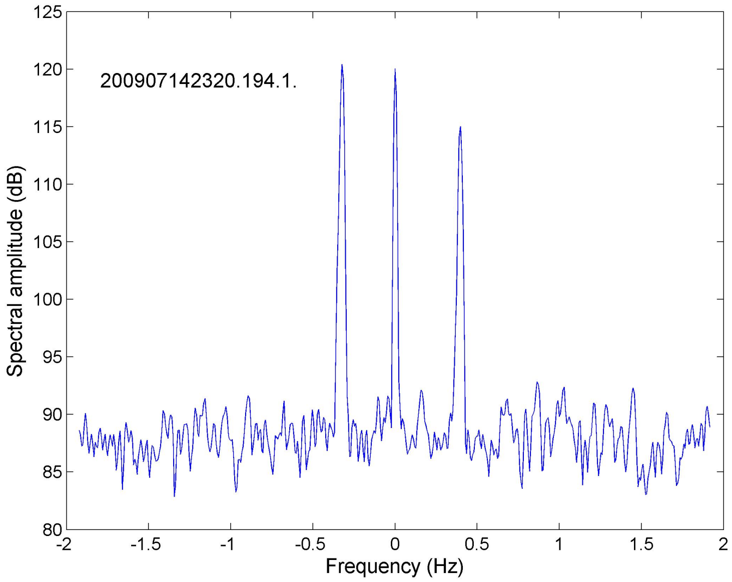

Figure 2.4: A Doppler Frequency spectrum example from the Liverpool Bay Coastal Observatory HF radar at Formby for cell 194 on July 14^{th} 2009 at $23:30$.

$$\omega_b = \sqrt{g k_b \tanh(k_b h)} \tag{2.11}$$

where g is the gravitational constant, 9.81 m/s^2, h is the water depth and k_b is the wavenumber specific to the Bragg scattering wavelength, $\lambda_b = \frac{\lambda_T}{2}$, related by equation 2.12.

$$k_b = \frac{2\pi}{\lambda_b} \tag{2.12}$$

The phase velocity, c_p, of this coherent scattering is given by:

$$c_p = \sqrt{\frac{g}{k_b} \tanh\left(k_b h\right)} \tag{2.13}$$

Current motion is apparent through any Doppler frequency shift, Δf, when an EM wave is returned from a moving object, in this case the waves of wavelength λ_b. This allows for a current measurement, u, in the look direction of the radar, referred to as the radial current, given by equation 2.14. With two or more radars a vector current can then be calculated from the individual radial measurements.

$$u = \frac{\Delta f \lambda_b}{2\pi} \tag{2.14}$$

Figure 2.5 highlights the expected Bragg frequency location (± 0.374 Hz) within a Doppler spectrum from the Llanddulas radar in Liverpool Bay. As can be seen on figure 2.5 and 2.6 the maximum amplitude peak is slightly offset from this line. Figure 2.6 shows the positive frequency expected Bragg scattering line and maximum amplitude peak zoomed in for the same Doppler spectrum as 2.5. The frequency shift highlighted on figure 2.6 is Δf allowing the measurement of the current component in the look direction of the radar using equation 2.14. As Doppler theory tells us, if the current is moving radially towards the radar then the expected frequency will be higher than the Bragg frequency and if moving away it will be lower, an effect more commonly known as blue and red shift, respectively.

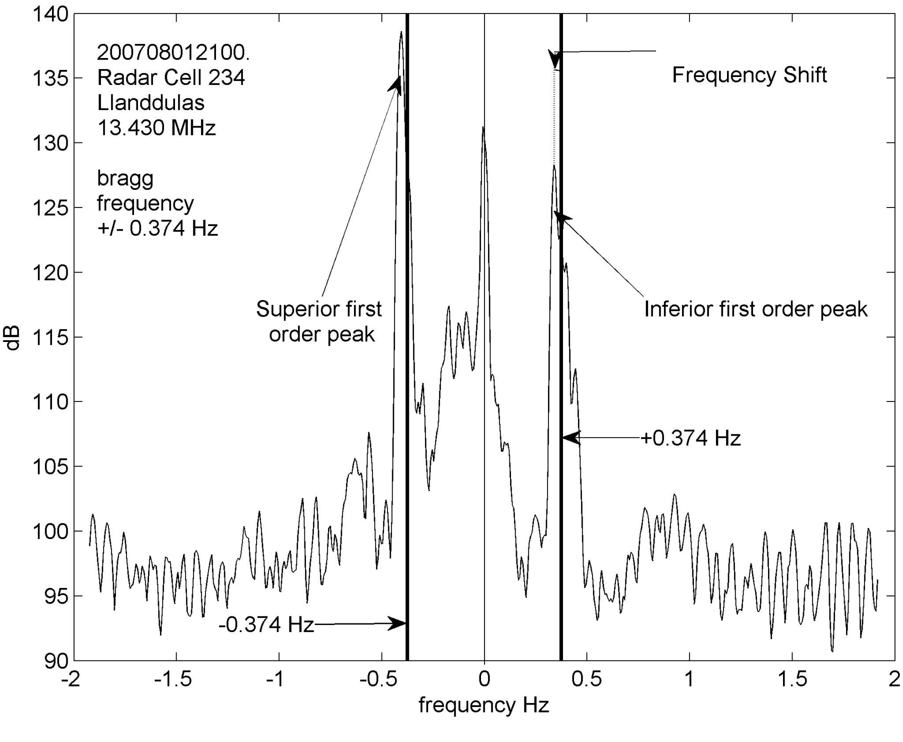

Figure 2.5: Doppler spectra current measurement.

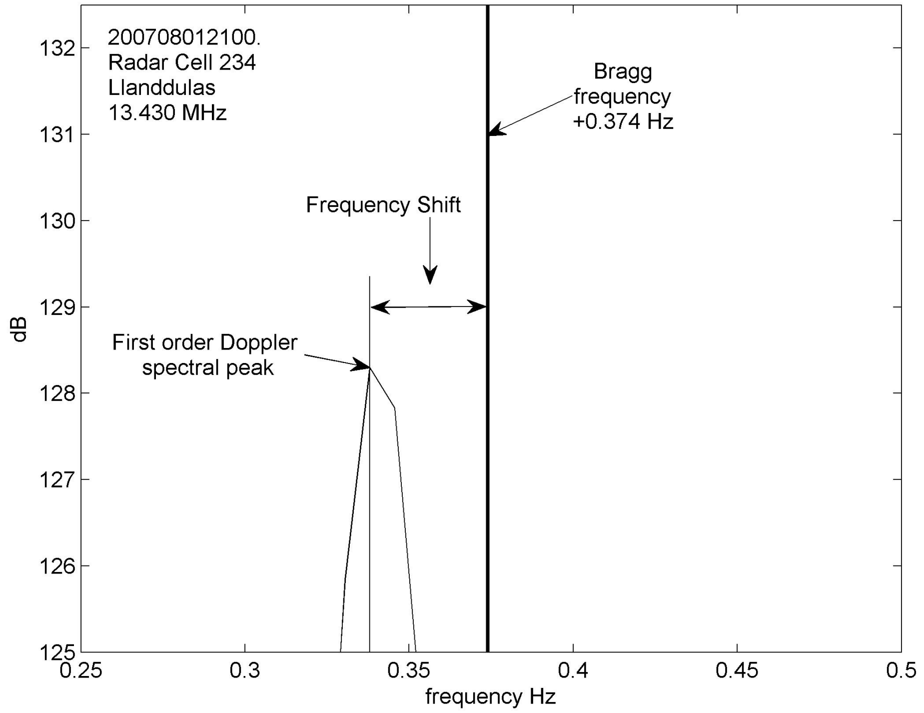

Figure 2.6: Typical Doppler spectra features.

2.7 Ocean wave theory

As defined by Young & Freedman [2000] "a mechanical wave is a disturbance that travels through some material or substance called the medium". Figure 2.7 shows some of the general properties used for describing a wave, which include:

- Wavelength (λ) - the distance between consecutive wave peaks
- Period (T) - the time taken for one complete cycle of the wave
- Frequency (f) - the fraction of a wave occurring in one second, ($f = 1/T$)
- Angular frequency, often denoted ω where $\omega = 2\pi f$
- Wave speed (v) - the distance travelled by one complete wave / the time taken for one complete wave, ($v = \lambda/T$)
- Amplitude (A) - the magnitude of the maximum displacement from equilibrium
- Phase (θ) - the stage of the wave relative to its cycle.

Mechanical waves, whose travelling paths intersect, combine at the point of intersection to form a resultant wave. There is no limit to the number of waves that can combine. What we see on the ocean surface is then a resultant of many

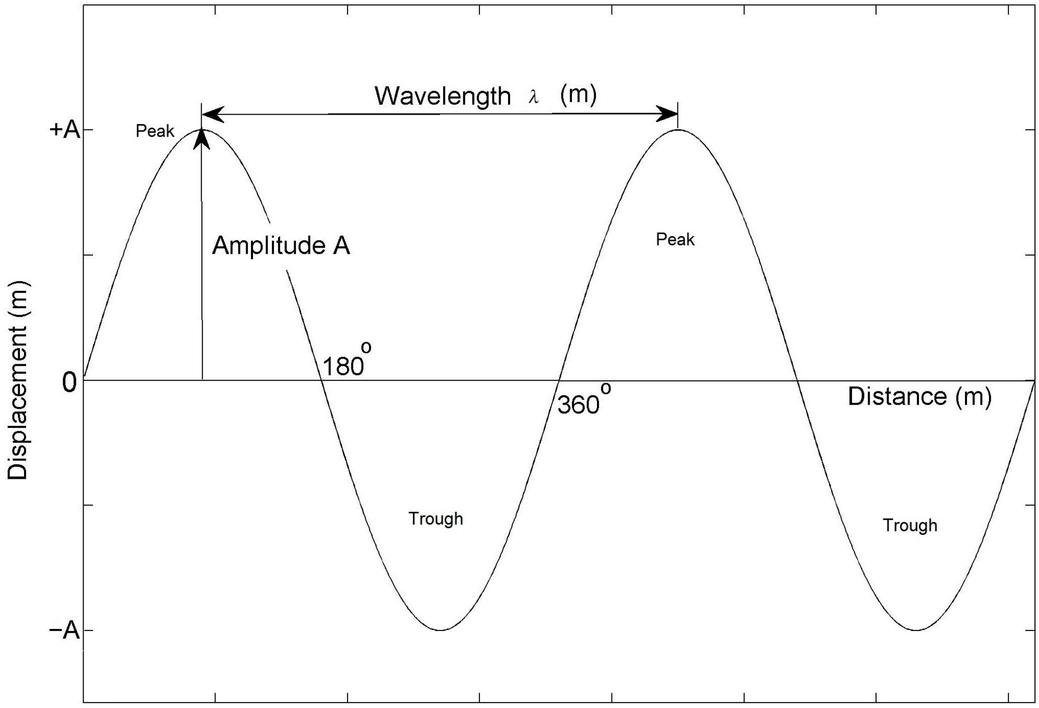

Figure 2.7: Defining properties of a wave.

waves with differing frequency and amplitude travelling from multiple directions interfering at a specific point. These can be either locally generated wind waves, see figure 2.8, or swell waves from distant storm events.

Figure 2.8: Wind driven ocean surface waves showing multiple directions of travel and wave height.

A linear sum of an infinite number of cosine waves can then be assumed, as done by Hauser *et al.* [2005]. This allows the principle of superposition to give the sea surface elevation, η, at a fixed point in space, $\mathbf{x}$ and time, t, as

$$\eta(\mathbf{x},t) = \sum_{n=1}^{N} a_n cos(\mathbf{k}_n \cdot \mathbf{x}_n - \omega_n t + \varphi_n) \tag{2.15}$$

where φ is the phase defining the surface elevation at a specific point and time, and $\mathbf{k}_n$ and ω_n are the wavenumber and angular velocity of the nth wave related by the dispersion relationship, equation 2.11. The general idea of a sea surface spectrum can then be developed from equation 2.15 following Hauser *et al.* [2005] chapter 2. Due to the unpredictable nature of the ocean surface caused by the interaction between so many different waves, statistical properties are used to describe the sea state. The independent and uniformly distributed phases allow estimates to be made of sea state conditions such as the mean, or expectation ($\mathbb{E}$), and variance of $\eta(\mathbf{x},t)$. Substituting equation 2.15 into equations 2.16 and 2.17, respectively.

$$\mathbb{E}(\eta(\mathbf{x},t)) = \frac{1}{2\pi} \int_{0}^{2\pi} \eta(\mathbf{x},t) d\varphi \tag{2.16}$$

$$Var(\eta(\mathbf{x},t)) = \mathbb{E}([\eta(\mathbf{x},t)]^2) \tag{2.17}$$

The solutions for equations 2.16 and 2.17 are given by

$$\mathbb{E}(\eta(\mathbf{x},t)) = 0 \tag{2.18}$$

$$Var(\eta(\mathbf{x},t)) = \mathbb{E}(\eta^2(\mathbf{x},t)) = \sum_{n=1}^{N} \frac{a_n^2}{2} \tag{2.19}$$

To obtain a basic expression for a spectrum, $\Psi(\mathbf{k})$, of $\eta(\mathbf{x},t)$ as given in equation 2.15, we multiply equation 2.19 by the Dirac $\delta-$ function satisfying $\int \delta(\mathbf{k}) f(\mathbf{k}) d\mathbf{k} = f(\mathbf{0})$ to get

$$\Psi(\mathbf{k}) = \sum_{n=1}^{N} \frac{a_n^2}{2} \delta(\mathbf{k} - \mathbf{k}_n) \tag{2.20}$$

The wavenumber spectrum, representing a variance density, is then

$$Var(\eta(\mathbf{x},t)) = \int_{\mathbf{k}} \Psi(\mathbf{k})d\mathbf{k} \tag{2.21}$$

where peaks in the wave spectrum for a particular wavenumber indicate significant contributions from waves moving in the direction of that wavenumber. Using the relationships of equations 2.11 and 2.12 as well as moving from Cartesian to polar coordinates allows equation 2.20 to be expressed as the directional wave spectrum, $S(\omega,\theta)$, equation 2.22 , in term of angular frequency ω and direction θ.

$$S(\omega,\theta) = \Psi(k(\omega),\theta)\frac{k(\omega)}{c_g(k)} \tag{2.22}$$

where c_g is the group phase velocity $\frac{\delta\omega}{\delta k}$. This can also be expressed as equation 2.23 in terms of the frequency spectrum $E(\omega)$ as

$$E(\omega) = \int_0^{2\pi} S(\omega,\theta)d\theta \tag{2.23}$$

and direction spectra in terms of directional distribution, D, where

$$\int_o^{2\pi} D(\theta,\omega)d(\theta) = 1 \tag{2.24}$$

is given by

$$S(\omega,\theta) = E(\omega)D(\omega,\theta) \tag{2.25}$$

The directional spectrum, an example of which is shown in figure 2.9, is a way of describing the irregular and unpredictable superposition of waves on the sea surface. It is characterised by the mean wave direction and directional spreading at the peak of the spectra, an in depth description of which is given by Hauser *et al.* [2005].

2.8 First and Second order sea states

It was the generalisation of Stokes' techniques for perturbation of an infinite field of two dimensional gravity waves by Barrick & Weber [1977] and Weber & Barrick [1977] that laid the groundwork for the mathematical theory for the first-order and second-order radar spectral cross section [Barrick, 1972a; Holden & Wyatt, 1992;

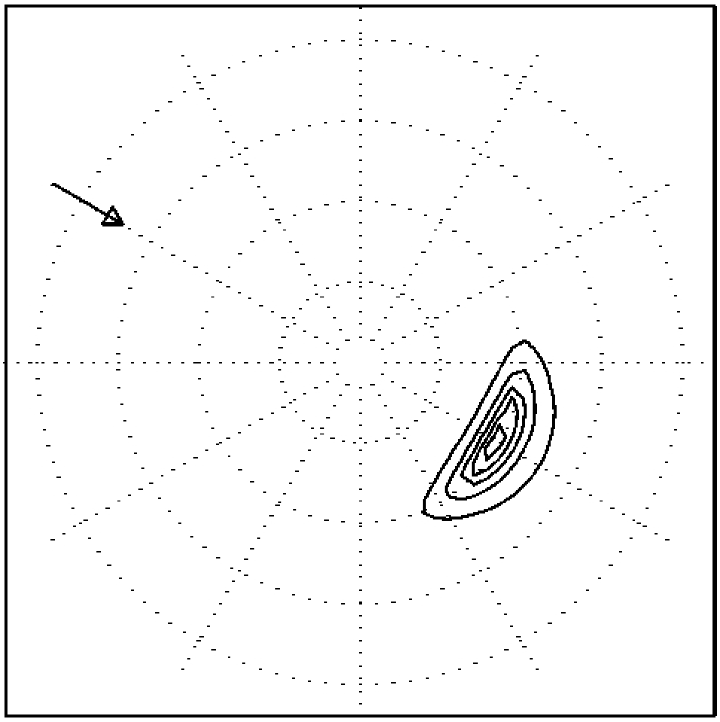

Figure 2.9: Directional spectrum, linear contour plot. The frequency scale circles have 1 rad/s steps. The circles correspond to approximately 60 m, 15 m, 7 m, and 4 m wavelengths. Figure 1.5:(a) taken from Hauser *et al.* [2005].

Lipa & Barrick, 1986]. Collectively referred to as the Barrick-Weber equations, they describe how the ocean directional wavenumber spectrum relates to the power spectrum of the demodulated backscatter. The first-order radar cross section is summarised by equation 2.26.

$$\sigma_1(\omega,\phi,d) = 2^6\pi k_0^4 \sum_{m'=\pm 1} S(-2m'k_0)\delta(\omega - m'\omega_b) \tag{2.26}$$

where $S(\mathbf{k})$ is the directional wave number spectrum, $\mathbf{k}_0$ is the ocean wave vector of magnitude k_0 in the look direction of the radar, ω_b is given by equation 2.11 and m' denotes the waves moving towards $(+m)$ and away $(-m)$ from the radar.

Non-linear surface interactions and second order Bragg scattering contribute to the second-order Doppler spectral region where wave parameters can be resolved. The theory of relating the second-order Doppler spectra to the sea state parameters is given by equation 2.27.

$$\sigma_2(\omega,\phi,d) = 2^6\pi k_0{}^4 \sum_{m,m'=\pm 1} \int_{-\infty}^{+\infty}\int_{-\infty}^{+\infty} |\Gamma_T|^2 S(mk_s)S(m'k_s') \tag{2.27}$$
$$\delta\{\omega - m\omega_b(k_s) - m'\omega_b(k_s')\}dpdq$$

where m equals ± 1, p and q are the parallel and perpendicular wavenumber components, respectively, to k_0 and Γ_T a coupling function encompassing linear scattering from non-linear waves plus non-linear (i.e multipath) scattering interactions [Holden & Wyatt, 1992].

The estimates are an average for the near surface and surface sea state up to a depth of *d* meters. For transmit wavelength λ_T this is given by Stewart & Joy [1974] as

$$d = \frac{\lambda_T}{8\pi} \tag{2.28}$$

At the approximate 13 MHz transmit frequency utilised in Liverpool Bay, current measurements are then depth averaged to approximately 1 m, where the transmit frequency ν_t and wavelength λ_t are related by $c = \nu_t\lambda_t$, where *c* is the speed of light.

2.9 Doppler spectra statistics

The ocean wave height (H) is defined as $2A$, or the height difference from peak to trough of a wave, and is highly variable in nature, as seen on figure 2.8. Due to this a mean of the third highest waves, referred to as the significant wave height, Hs, is more commonly used and Hs is sometimes thought to be roughly the height that a sailor might estimate by eye. A statistical descriptor for Hs in the time domain is calculated from the variance of the surface displacement. In the frequency domain Hs is given by equation 2.29.

$$Hs = 4\sqrt{\int_0^{\infty} E(\omega)d\omega} \tag{2.29}$$

where the radicand is the zeroth moment, m_0, for $n = 0$ given by

$$m_n = \int_{-\infty}^{\infty} E(\omega)\omega^n d\omega \tag{2.30}$$

where $E(\omega)$ is the ocean wave spectrum as a function of ocean wave frequency ω.

Another important statistical descriptor of the sea state is the mean, or first moment period T_1, as set out in equation 2.31 and determined from m_0/m_1.

$$T_1 = \frac{\int_{-\infty}^{\infty} E(\omega)\omega^0 d\omega}{\int_{-\infty}^{\infty} E(\omega)\omega^1 d\omega} \tag{2.31}$$

The frequency of the wave with maximum energy is referred to as the peak period T_p corresponding to $\frac{1}{\omega_p}$. Other statistical quantities can also be obtained from higher order Doppler spectral moments, examples of which are listed by Tucker [2000].

2.10 HF radar systems

Many comparative studies have been undertaken between HF radar and in situ measurements to gauge HF radar performance and accuracy. The operational principles of each HF radar type are relatively similar and variants tend to be operating frequency, transmission mode, antenna configuration and processing methods.

Current and wave measurement with HF radar were first achieved in the early 1970's by the NOAA Environmental Research Laboratories lead by Barrick [1972a]. The antenna utilised was a 500 m phased array that was quickly superseded by the CODAR system. Three other systems developed over the last 30 years are Ocean Surface Current Radar (OSCR), Pisces and WERA radars. Each radar has a wide range of working spatial resolutions and antenna configurations that, combined with a large frequency range, allow for different applications.

CODAR has progressed over the last 40 years utilising several different antenna designs [COS, 2010a]. CODAR can resolve first-order spectral bands and is specifically designed for current mapping. Wave measurement with the second-order Doppler spectra can also be achieved although it is more difficult and less common. The original CODAR system used a pulsed waveform with approximately a 3 km blind range and performs azimuthal resolution by direction finding. CODAR has now been superseded by the SeaSonde system. SeaSonde has been utilised in multiple HF radar operations [Fernandez & Paduan, 1996; Kaplan *et al.*, 2005; Kelly *et al.*, 2003; Paduan & Rosenfeld, 1996] and continually achieves good correlations with in situ measurements. SeaSonde is compact in design and can deliver real-time data up to 200 km off shore [Kjelaas & Whelan, 2011]. Designed to operate within a network of 2 or more radars for 2D current vectors, the SeaSonde has an average output power of 80 watts radiated as a pulsed frequency modulated, interrupted, continuous wave (FMICW) with up to 360^o coverage [COS, 2010b].

OSCR was developed during the 1980's at the Rutherford Appleton Laboratory of the United Kingdom Science and Engineering Research Council [King *et al.*, 1984]. With the option to operate at HF and VHF frequencies, the OSCR system was designed for short range surface current measurement [Prandle, 1985]. OSCR is a phased array radar using a pulsed waveform to determine range and a linear receive antenna array with beamforming for resolving direction, see section 3.2.2

The Pisces radar [Shearman & Moorhead, 1988; Wyatt, 1990] was developed in the 1980's by Neptune Radar Ltd., UK from a University of Birmingham prototype. Pisces radar operates at lower HF frequencies, $5 - 15$ MHz, to minimise high sea state limitations and allow for long range wave measurement. Pisces is a phased array radar using FMICW operation with a peak power output of 1200 W [Wyatt *et al.*, 2006].

The WERA radar was developed by the University of Hamburg in 1996 as part of the EU funded project SCAWVEX (surface current and wave variability experiment) [Wyatt *et al.*, 1995]. The WERA HF radar design allows for operating frequencies from 5 to 50 MHz. A frequency value for operation is selected for either local conditions or range requirements. A frequency sweep before transmission can detect a large RFI. This can aid the selection of the frequency to be transmitted from within the operating licence bandwidth and is starting to be utilised with WERA systems [Dzvonkovskaya *et al.*, 2009].

WERA radar uses FMCW chirps avoiding a blind range in front of the radar. The transmit and receive antenna are co-located but ideally separated in height and orientated so as to minimise direct signal transmission. Both phased array beamforming and direction finding capability [Helzel *et al.*, 2011] are supported for azimuthal resolution allowing for current mapping and sea state resolving [Gurgel & Antonischki, 1997; Gurgel *et al.*, 1999a].

The radar which is the focus of this thesis is a HF WERA radar system, the configuration and signal processing for which is discussed next in chapter 3.

Chapter 3

WERA Signal and data processing

In order to link measurements with meaningful scientific theory it is important to understand the temporal and spatial averaging that results from the method and signal processing. This gives the HF radar measurement physical meaning and allows it to be accurately compared with other methods of measuring the same parameter.

WERA radar is a highly adaptive system. At installation multiple antenna configurations are possible and a wide range of operating frequencies and chirp lengths can be selected. These operating parameters are not fixed and can be altered. Also with such diverse antenna configurations different processing methods can be applied. As such, the performance and accuracy of each HF WERA radar system will be unique.

In this chapter the methods involved with the signal processing of data from WERA radar will be discussed following methods given by Gurgel *et al.* [1999a].

3.1 Hardware

A square array of 4 transmit antennas, operating at a power of 30 W, emit a vertically polarised electromagnetic wave of wavelength λ_T. Vertical polarisation is used as attention of the signal is much less than for horizontally polarised EM waves. The signal is transmitted as a linear frequency chirp of T seconds with signal form

$$s(t) = \sin\left[2\pi\left(\nu_0 + \frac{b}{2T}t\right)t\right] \tag{3.1}$$

where during the chirp period T of 0.26 seconds, t ranges from 0 to T seconds and ν_t increases linearly from ν_0 (the frequency at $t = 0$) to $\nu_0 + b$ (the frequency at

$t = T$). The chirp length T is the rate at which the sea surface variability is sampled. The band of frequencies used is characterised by the bandwidth, b, in Hertz, as

$$b = f_{high} - f_{low} \tag{3.2}$$

where b is the difference between the highest and lowest frequency, f_{high} and f_{low}, respectively. The bandwidth selection, of which several are available using the WERA system, determines the range resolutions, Δr, by

$$\Delta r = \frac{c}{2b} \tag{3.3}$$

where c is the speed of light and b is the selected frequency bandwidth [Gurgel *et al.*, 1999a]. In Liverpool Bay, where the bandwidth is 50 kHz, there is a range resolution of 3 km on the initial radial grid. This is then interpolated to a 4 km range grid for current and wave measurements.

The transmit signal of equation 3.1 travels over the horizon via ground-wave propagation. This is along the sea and atmospheric boundary. The incident radar wave, given by equation 3.1, scatters off any surface or object with which it interacts and backscatter at the linear array of 16 receive antennas, co-located with the transmit antennas, is the summation of scatter from multiple directions. The signal received by the radar, $r(t)$, is then given by

$$r(t) = \int \alpha(\tau) \sin\left[2\pi\left(\nu_0 + \frac{b}{2T}(t-\tau)\right)(t-\tau) + \varphi(\tau)\right] d\tau \tag{3.4}$$

where $r(t)$ is a superposition of HF waves scattered from all distances over the measurement area and τ is the propagation time from the radar to the scattering point and back again. Variations of the scattering surface waves causes small variations at any given time τ in amplitude, $\alpha(\tau)$, and phase, $\varphi(\tau)$, but are considered constant for the duration of any one chirp. The backscatter signal given by equation 3.4 contains modulations in amplitude and phase.

A phase coherent demodulation of the signal is performed with independent direct-conversion receivers at each receive antenna. The quadrature and in-phase time series are achieved by phase-coherent demodulation. The resulting complex series, $z(t)$, for each antenna is then

$$z(t) = \int \frac{\alpha(\tau)}{2} \exp\left[i\left(-2\pi\frac{b\tau}{T}t+\phi(\tau)+\varphi(\tau)\right)\right] d\tau \tag{3.5}$$

For the complex time series from each receive antenna a high pass filter is used to attenuate signals received directly from the transmit antenna and a low pass filter removes frequencies above the Nyquist (half the sample rate frequency or 2b).

Hardware operations, provided by Helzel Messtechnik, cease with a 16−bit analogue to digital conversion on the signal from each individual antenna with an over-sampling of 13 times. At this point signal processing using software routines commences, as summarised by figure 3.1.

3.2 Signal processing

Figure 3.1 is adapted from Gurgel *et al.* [1999a] and gives an overview of the signal processing steps for WERA radar.

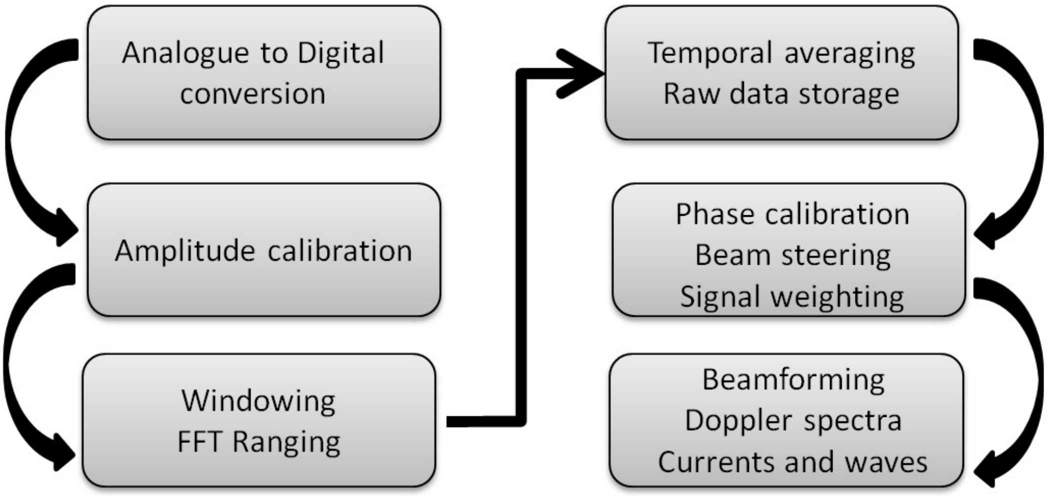

Figure 3.1: Signal processing steps implemented in the Liverpool Bay WERA Radar, adapted from Gurgel *et al.* [1999a].

The analogue to digital conversion is followed by an amplitude calibration to account for any gain variation between antennas [Gurgel *et al.*, 1999a]. The N chirps are sectioned into M data points per section which are then processed independently applying a Blackman-Harris window, the equation for which is given by:

$$\omega(nT) = a_0 - a_1\cos\left(\frac{2\pi nT}{M}\right) + a_2\cos\left(\frac{4\pi nT}{M}\right) + a_3\cos\left(\frac{6\pi nT}{M}\right) \tag{3.6}$$

where n is the n^{th} sample out of the total N samples, M is the number of samples in each segment, T is the sample period, $a_0 = 0.35875$, $a_1 = 0.48829$, $a_2 = 0.14128$, and $a_3 = 0.01168$. The application of the Blackman-Harris window in the time domain before the Fourier transform minimises spectral leakage caused by wavelengths that do not divide exactly into the window size of the individual chirps.

The signal samples $z(nT)$ are multiplied by the window function to give the product

$$z^k(nT) = z^k(nT)\omega(nT) \tag{3.7}$$

3.2.1 Range Resolution

The Fourier transform, as given by Emery & Thomson [2001], for $z^k(nT)$, of M samples, is then applied to each chirp giving

$$Z^k\left(\frac{2\pi m}{MT}\right) = \sum_{m=0}^{M-1} z^k(nT)\exp\left[\frac{-2\pi imn}{M}\right] \tag{3.8}$$

This resolves the data into different range bins containing information on the sea surface variability, counted by n. The complex voltages recorded in the .sort files are given by Gurgel *et al.* [1999b] as

$$\upsilon(n\Delta r, t) = \alpha(n\Delta r, t)\exp[i\varphi(n\Delta r, t)] \tag{3.9}$$

The data at this point in processing are then a superposition of backscattered signals from different azimuthal directions at given range cells for each individual antenna. Range resolved data are then stored by NOCL for approximately 2 years in case of the possibility of future reprocessing.

3.2.2 Azimuthal Resolution

The optimum angular resolution achievable is given by λ_t/D where D is the length of the antenna array and λ_t is the transmit wavelength [Gurgel *et al.*, 1999b]. For a 13 MHz radar, with transmit wavelength of 23 m and a 16 antenna linear receive array at optimum spacing $\lambda_t/2$, as in Liverpool Bay, the angular resolution of each antenna is then 7.6^o.

In Liverpool Bay the process of beamforming, pictured in figure 3.2, is used to combine range-resolved data into azimuthal bins. Neptune Radar Ltd provide the RMAN software used for the beamforming.

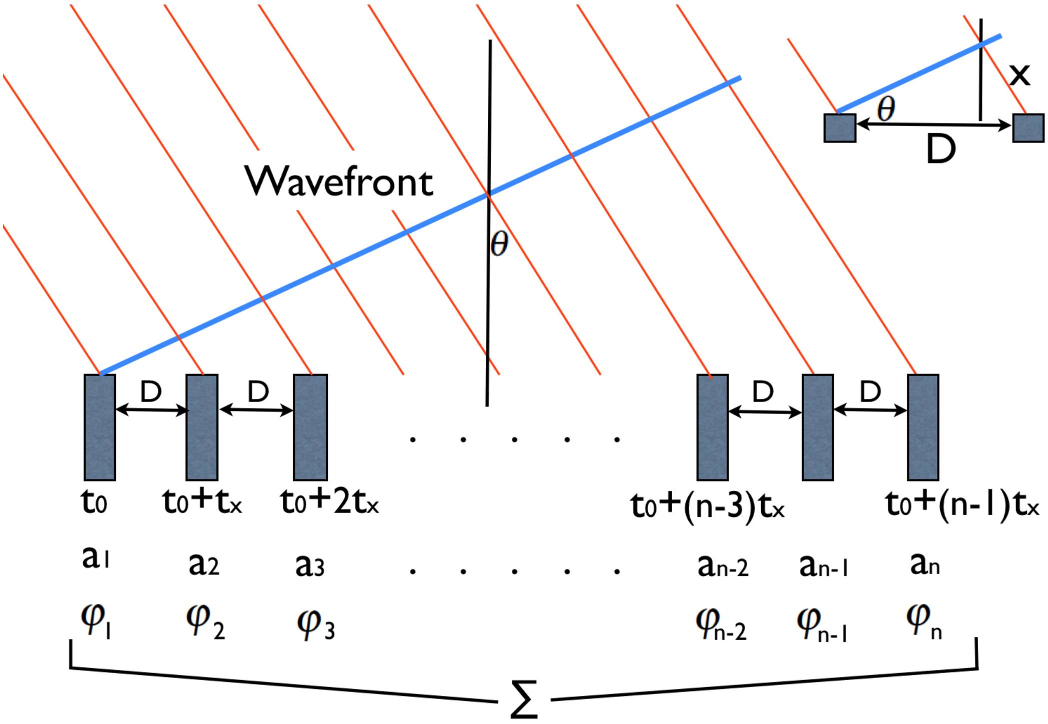

Figure 3.2: A representation of beamforming for n antennas with spacing D, signal weighting amplitude a and phase φ. Adapted from Gurgel *et al.* [1999a].

The signal, as given by equation 3.9, is first phase calibrated then phase-shifted before the electronic steering of the receive antenna to a particular direction. The basic idea stems from the varying arrival time of a wavefront along a linear antenna array. A wavefront from a given patch of sea that approaches the receive array with angle θ equal to zero, or broadside to the array, will arrive at each individual antenna simultaneously and in phase. When θ does not equal zero the wavefront will arrive at adjacent antenna, distance D away, with a time delay equal to t_x, the time it takes to travel distance x, as depicted in figure 3.2. This time is given by

$$t_x = \frac{x}{c} = \frac{\mathrm{D}\sin(\theta)}{c} \tag{3.10}$$

where c is the speed of light. The signals from each antenna are weighted by amplitude a to reduce any sidelobe effects. For backscatter arriving from a particular bearing the additional travel time to each antenna is known and the associated phase shift can be made. When the amplitude contributions from each antenna are then summed in phase the resultant amplitude will have maximum value.

For the most used 532 seconds measuring period in Liverpool Bay, temporal averaging of the received signal is done over the coherent measurement period and the resulting 2048 chirps, as selected in the radar configuration. Temporal averaging for 1064 seconds is also an option and has been utilised for some measurements in Liverpool Bay. To obtain the Doppler spectra Fast Fourier Transforms are carried out for each set of 512 samples with a 75 % overlap. The resulting 13 Doppler spectra are then averaged for statistical stability. The data are stored at this last step in the RMAN signal processing as averaged Doppler Spectra for each cell for a given time. The Doppler spectra are then processed for current, wind, and wave parameters.

Chapter 4

The Liverpool Bay Coastal Observatory

> *We need to ensure that the oceans are fully recognised for their ability to provide solutions to the big challenges facing society, which concern sustainable use of natural resources and the management of environmental risks and hazards.*
>
> Prof Ed Hill, NOC Executive Director (http://noc.ac.uk)

In this chapter the motivation driving NOCL in their measurement capability is discussed along with operational and deployment details of the HF radar, ADCPs and Waverider buoy analysed in this thesis. Results from previous studies comparing HF radar measurements to those of in situ devices are presented so as to set out the expectations of good measurement values within the field.

The Liverpool Bay Coastal Observatory (LBCO) has been operational since 2002 serving as part of the national and international scientific infrastructure to address associated questions of what will result from our changing climate. Environmental issues have gained significant momentum on the political agenda of recent times. Climate change and its effects top the list of current concerns. This has resulted in measurement, monitoring and prediction of environmental indicators globally over long time periods.

Utilising many measurement and observation techniques LBCO is part of taking coastal monitoring to new heights in the UK. The inter-related complexity of all coastal processes and the value of quality time series data is addressed with the LBCO. The data collected from the multitude of measurement devices, detailed in table 4.1 and 4.2 and shown on figure 4.1, has contributed to modelling the interaction of coastal processes with the aim to forecast and hindcast accurately.

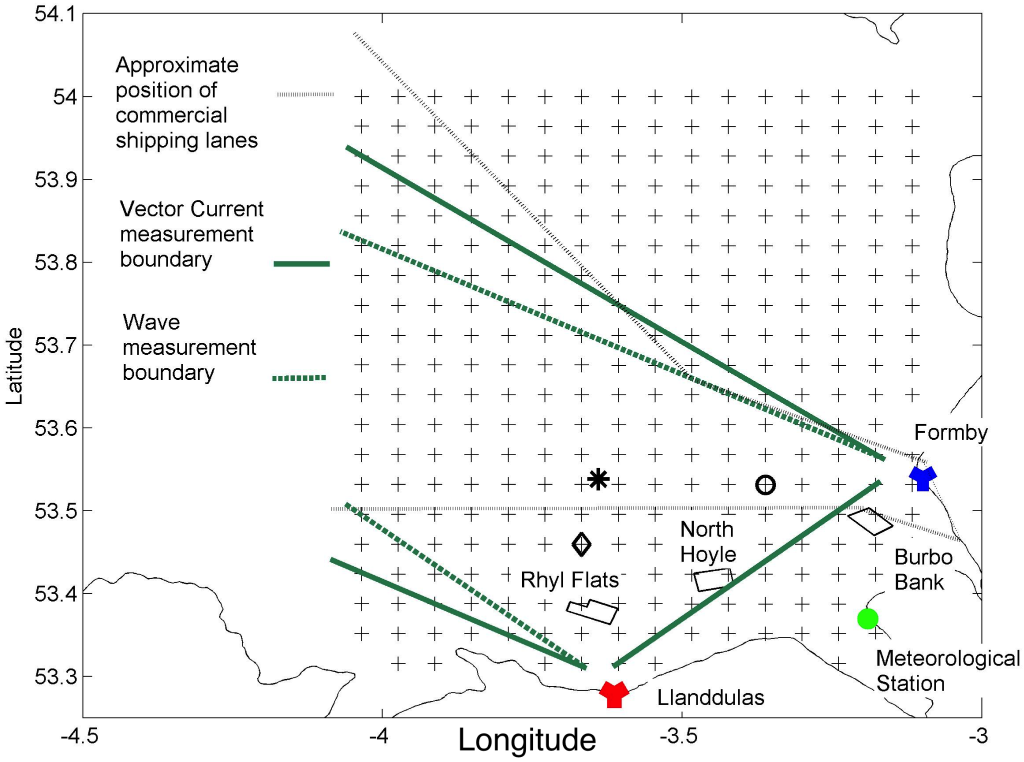

Figure 4.1: The Liverpool Bay HF radar measurement footprint for current and wave measurements. The co-location of radar cell 234, the wave buoy and ADCP A is indicated with the symbol ’o’. The ◇ represents radar cell 136 and the position of ADCP B in 2009. Location $*$ marks ADCP B in 2010. North Hoyle, Burbo Bank, and Rhyl Flats wind farms are also indicated as well as the two radar sites and Hilbre Island Meteorological Station.

LBCO, based at the University of Liverpool, contributed a large part to the monitoring capability of NOCL with consistent and long time series data. Modelling at the LBCO is done collaboratively with the MET Office providing outputs from the POLCOMS, Wave and North Atlantic European (NAE) (used as inputs to POLCOMS) models. Together they aim to:

1. Integrate near real-time measurements with coupled models
2. Understand a coastal sea’s response to natural and anthropogenic forcing
3. Research into the functioning of a shelf sea in a changing climate

To achieve this they work with a multitude of partnership organisations, some of which are listed in tables 4.1 and 4.2, and over time have collected a large array of measurement parameters. A summary of their in situ deployments, measurement capability and data availability is given in table 4.1 and their remote sensing capability in table 4.2.

Equipment	Location	Measurement parameter	Data Availability	Relevant partnerships
Tide gauge network 1	Port Patrick, Bangor(NI), Port Erin, Workington, Heysham, GL, Llandudno, Holyhead, Barmouth	tidal sea levels	Real time	National Tidal and Sea Level Facility network (NTSLF)
Tide gauge network 2	Alfred Lock, BB, Eastham Lock, GL (Mersey Estuary)	tidal sea levels	Real time	Mersey Docks and Harbour Company network
'Liverpool Seaways' ferry	Currently inactive	Temperature, salinity, turbidity and chlorophyll,	Archived data only. Inactive	DFDS Seaways
MET station	Hilbre Island	Wind, Temperature, Pressure, Humidity, Solarity, Rainfall	Archived data only	
Glider	South of the Isle of Man	temperature, conductivity, salinity	Archived data only	
ADCP	A53^{o}32.04N 3^{o}21.49W, B153^{o}26.97N 3^{o}38.53W, B253^{o}32.42N 3^{o}38.63W	current profile, temperature, conductivity, turbidity, pressure, nutrients, fluorescence, oxygen	Archived data only	
Datawell directional waverider buoy (DWR)	53^{o}32N 003^{o}21.8W	Hs, Tp and direction, Phytoplankton concentration, nitrate and silicate concentration	Real time and Archived data	Cefas, WAVENET
SmartBuoy	A53^{o}32.017'N 3^{o}21.491'W, B53^{o}26.896'N 3^{o}38.313'W	Fluorescence, turbidity, salinity, Sea water temperature, Oxygen saturation	Near-real time	CEFAS, National Monitoring Programme
Wave Buoy	Dee Estuary	Hs, Mean spectral period, Tp, Wave direction, Maximum wave height, Surface water temperature	Archived data only	

Table 4.1: Liverpool Bay Coastal Observatory in situ measurement capability overview. Nomenclature includes significant wave height (Hs), peak period (Tp), Acoustic Doppler current profiler (ADCP), Meteorological (MET) Burbo Bank (BB) and Gladstone Lock (GL).

Equipment	Location	Measurement parameter	Data Availability	Relevant partnerships
X-Band Radar	Hilbre Island	surface currents, Significant wave height peak wave period and direction	Currently inactive, Real/near-real time up to January 2012	
HF WERA Radar	Llanddulas and Formby	surface currents wind measurements Significant wave height peak wave period and direction	weekly, Real/near-real time up to December 2011	Helzel Messtechnik, Neptune Radar Ltd, Seaview Sensing Ltd
Satellite	N/A	Average Sea surface: temperature, Chlorophyll, Suspended sediment	Archives data only	NERC Earth Observation Data, Acquisition and Analysis Service

Table 4.2: A summary of the Liverpool Bay Coastal Observatory remote sensing measurement capability.

4.1 HF WERA radar

The HF WERA radar system operated by NOCL has been providing data since 2004. Real time data was available via the NOCL website every 20 minutes from August 2005 to April 2011 and thereafter hourly up to the end of the deployment in December 2011. The radar system was located on two sites, Llanddulas and Formby. Each site consisted of a square array of 4 transmit antenna, as shown in figure 4.2, a linear array of 16 receive antennas (figure 1.2 and 4.3) parallel to the coast and a cabin housing the radar control equipment, see figure 4.1 for locations.

Llanddulas is situated on a mitigated landfill site on the North Wales coast. The transmit and receive antenna, shown in figure 4.2 and 4.3 respectively, are separated by 0.5 km in distance and 0.5 m in height. This physical separation helps to reduce direct transmit to receive antenna transmission.

Currents in Liverpool Bay are dominated by the M_2 tidal constituent in an east-west direction. This is clearly seen in figure 4.4 where 2 years worth of current measurements have been split into their direction bins. Only a small component of the vector current is in the north-south direction. As a result of this the Llanddulas radar, which has its boresight 12.2^o from north, is predominantly measuring this

Figure 4.2: HF WERA radar square transmit antenna array, Llanddulas March 2003. Image taken from the NOC archive at http://cobs.pol.ac.uk/wera/photos/.

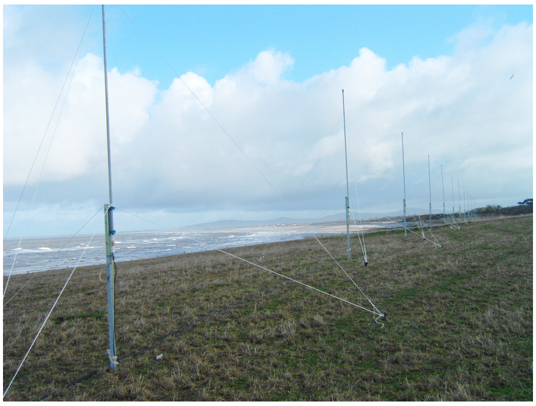

Figure 4.3: HF WERA radar, 16 linear receive antenna array, Llanddulas March 2003. Image taken from the NOC archive at http://cobs.pol.ac.uk/wera/photos/.

north-south, smaller, current component.

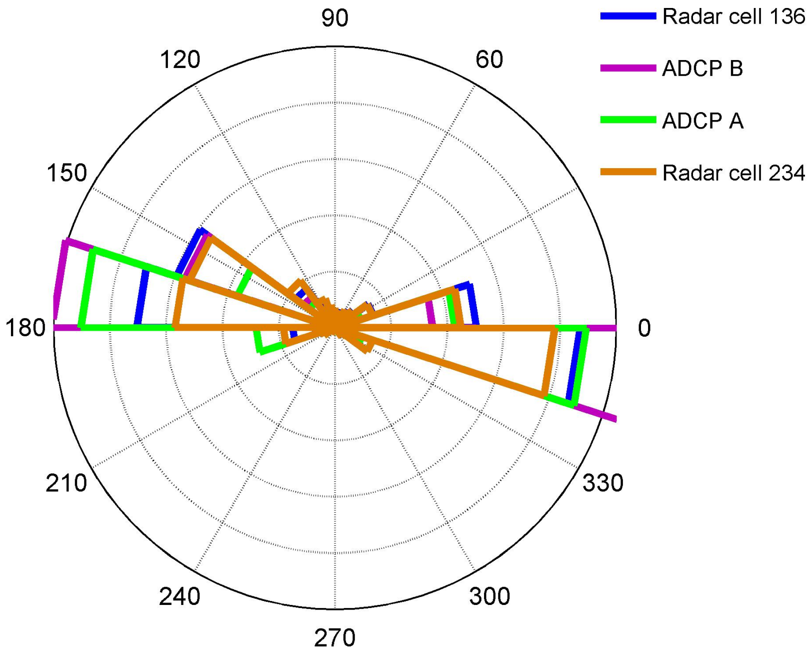

Figure 4.4: A directional histogram for 2 years of current measurements from radar cells, 234 and 136 and 2 in situ ADCPs.

Llanddulas has a higher noise floor than Formby and on occasions over the experiment has experienced power surges, cables being eaten by rodents and the accidental cutting of the guy lines supporting the antennae. The exact cause of the increased noise floor is unknown but is thought in part to be due to nearby metal fencing, a busy A road and some direct transmission from the transmit antenna.

The Formby radar is located in an open access area for the public owned by Sefton Borough council. It is situated on active sand dunes just off the beach. There are 0.4 km in distance and 11 m in height separating the transmit and receive antenna and its boresight is 231.7^o from north. As such it is predominantly measuring the east-west current, a much larger component than the north-south. Problems inherent from the nature of the site can reduce data quality. Sand has been known to sporadically bury sensors, extensive sandbanks potentially cause signal distortion and there is a range limitation due to the attenuation across the extensive shallow gradient beach. The noise differences between the radar sites are discussed in more detail in chapter 5.

During the HF radar deployment measurements were taken every 20 minutes with both the Llanddulas and Formby radar. Transmit frequency, as detailed in table 4.3, was different at each radar site to allow for simultaneous data acquisition. NOCL has made use of different measurement options available with the HF WERA radar at various times throughout the deployment. Most recently data was temporally averaged over 8 minutes and 52 seconds starting at 00 and 40 minutes past the hour and 17 minutes 44 seconds at 20 past the hour. Pre November 2009 the measurement at 20 minutes past the hour was taken over 8 minutes and 52 seconds but was then changed to a longer averaging time for better second-order spectral measurements.

Time past the hour	Ldl Frequency MHz	Fby Frequency MHz
00	13.430	12.450
20	13.465	12.465
40	13.395	12.435

Table 4.3: Llanddulas (Ldl) and Formby (Fby) radar operating frequencies.

Backscattered data received by the radar were processed in near real-time and recorded on a 4 km rectangular grid up to a 75 km range. Various quality control parameters are set to filter the radar data even before the calculation of current or wave parameters. NOCL applied default criterion as set out in their processing software supplied by Seaview Sensing Ltd. This includes criteria based on signal to noise ratios within the Doppler spectra and is discussed in chapter 5.

Prevalent unwanted backscatter when measuring ocean parameters includes radar returns from ships and offshore structures, such as wind turbines. If moving at a similar speed to those of the ocean parameters of interest they produce a similar Doppler signature possibly corrupting the measurements. Ships are floating on the ocean surface and so will exhibit motion influenced by waves and may also move at speeds similar to those of ocean currents. Figure 4.5 shows a Doppler spectrum produced by the Llanddulas radar. The first-order Doppler spectra region for determining currents is shown in black and the second-order region for determining waves is shown in grey. On the superior side the second-order region is determined as frequencies up to $1.6\omega_b$, where ω_b is the Bragg frequency, from the first-order Doppler spectrum peak. On the inferior side frequencies up to $0.4\omega_b$ are included. A Doppler frequency amplitude characteristic of a ship is identified in figure 4.5 and is clearly seen to fall within the frequency range used for wave measurement.

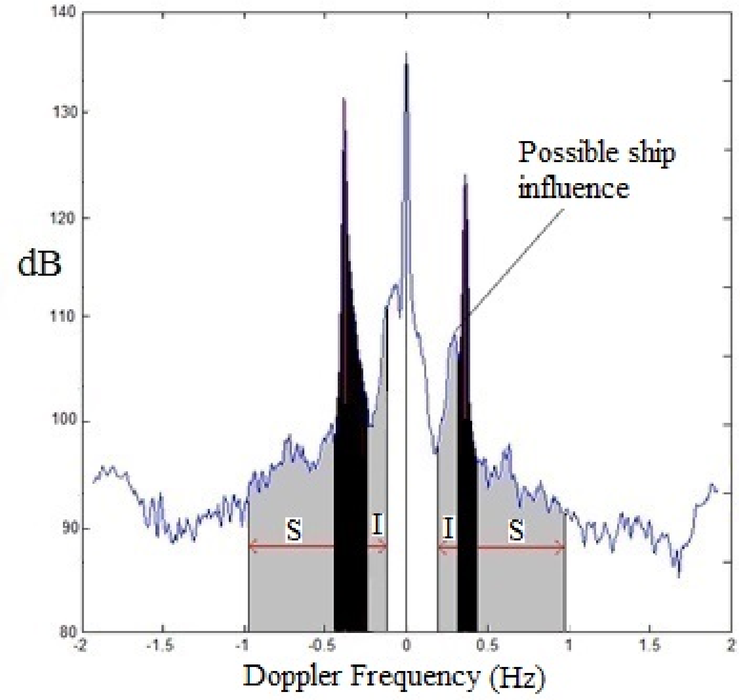

Figure 4.5: Doppler spectra measured by Llanddulas HF radar for cell 158 pre Rhyl Flats wind farm. S and I are the superior and inferior second order regions, respectively. The buoy Hs measurement at this time is 0.6 m.

Typical ship velocities in the Liverpool Bay area range from 2 to 12 knots (1 m/s to 6.2 m/s), up to a maximum of around 19 knots (9.8 m/s). Figure 4.6 shows the Doppler frequency shifts that would be expected for speeds up to 9.7 knots, or 5 m/s. For example a 3.9 knots speed in a direction of 232^o south-west has an westward velocity of 1.2 m/s and a southward velocity of 1.6 m/s. These speeds would appear at a frequency of $\omega_b \pm 0.3$ Hz and $\omega_b \pm 0.4$ Hz. Figure 4.6 shows that ships moving up to about 4 knots will appear in the frequency range used for measuring ocean currents and waves. Although these speeds are relatively slow, ships approaching the coast will be reducing speed. This can cause problems for current and wave measurement in its co-located radar measurement cell. Ships travelling at a faster speed further away from the coast may also fall within the first and second-order Doppler spectra region depending on the first-order spectral width.

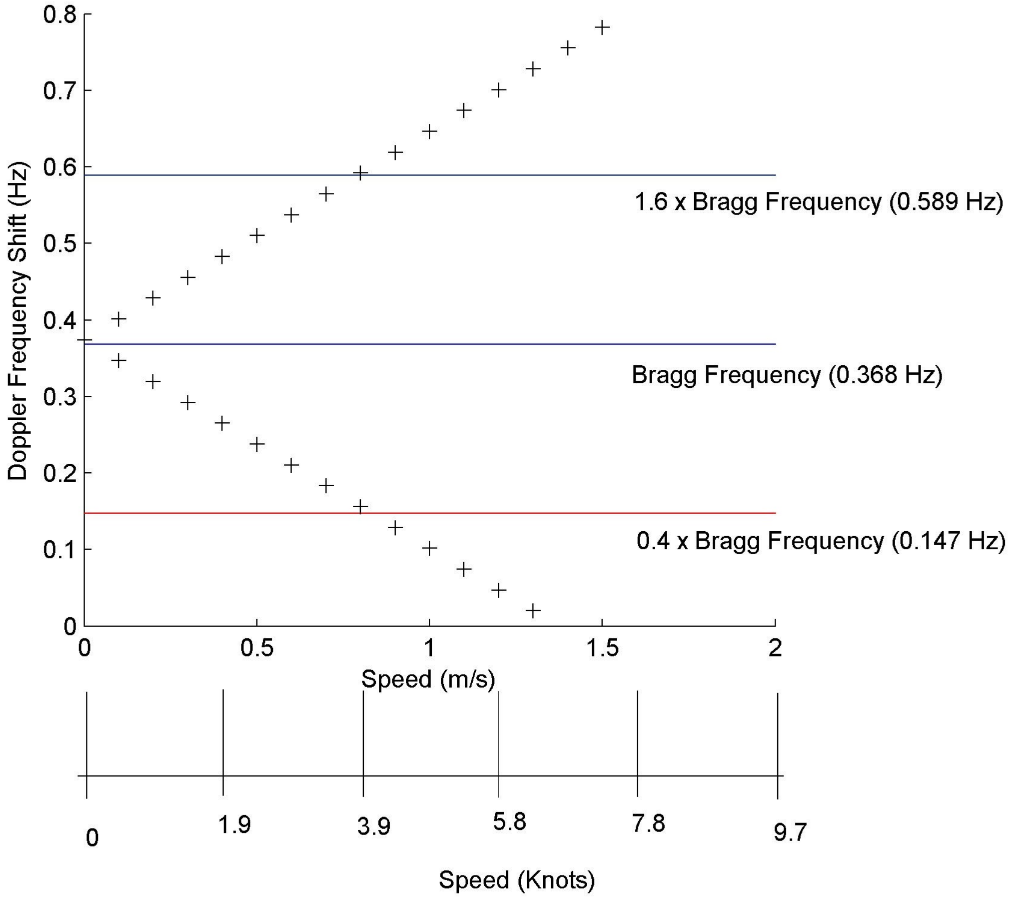

Figure 4.6: Doppler frequency shifts in the Liverpool Bay WERA radar Doppler frequency spectra caused by objects moving at speeds ranging from 0 to 1.5 m/s.

4.2 Waverider Buoy

Wave buoys are widely used and well established in the oceanic community. Their measurements are often used as the industry standard from which model outputs and other instrumentation are tested. The Liverpool Bay Datawell directional waverider buoy (DWR) is co-located with radar cell 234 at mooring site A, as shown on figure

4.1. It provides a single point measurement, recorded every 30 minutes, for the near shore wave monitoring network (WaveNet) [Hawkes *et al.*, 2001] (WMO ID 62287).

Direction ranges from 0^o to 360^o with a 1.5^o resolution and typical 0.5^o heading accuracy. The buoy is designed for a maximum current speed of 3 m/s and has wave height range of ± 20 m with a resolution of 1 cm. The accuracy is then better than 3% of the measured value, with expected degradation over time. The accelerometer housing, electronics and batteries have a shockproof mounting to minimise any effects from collisions.

The buoy provides an estimate of the ocean wave frequency spectrum and Fourier coefficients of the directional spectrum by using on-board microprocessors to combine horizontal and vertical accelerometer measurements with pitch and roll data [Teague *et al.*, 2001]. Transmitting in the upper HF band ($27-40$ MHz) the data are available in close to real time via telemetry at:

http://map.cefasdirect.co.uk/wavenetmapping/StaticMapPage.asp.

The results from the previous 24 hours are displayed and archived data is available from the Centre for Environment, Fisheries and Aquaculture Science (CEFAS) archives.

Quality control of the buoy data is done at several levels and all procedures are set out in the CEFAS QA/QC procedure list available at http://www.cefas.defra.gov.uk. Accelerometer measurements are digitally integrated with a cut-off at 0.6 Hz. Corruption from the use of telemetry is examined to ensure what was measured is what was transmitted. For each parameter a range of physically acceptable values have been identified and measurements falling outside of this are dismissed. An example of this is defining within the data a maximum rate of change between consecutive measurement values.

4.3 Acoustic Doppler Current Profiler

NOCL operates two 600 kHz RDI (RD Instruments) ADCPs positioned as shown in figure 4.1. Denoted sites A and B and shown on figure 4.1, ADCP A is colocated with radar cell 234 and ADCP B with cell 136 prior to January 2010 and 134/154 thereafter. These ADCPs are bed-mounted, emitting four orthogonal high frequency sonar beams inclined 20^o from the vertical. ADCPs transmit multiple signal pulses that are then scattered from particles in the water column. Range-gating is then used to determine the position of the scattering particles. Any phase shift of the backscatter is used to determine current velocity in the direction of the beam, calculated at various depths throughout the water column. Ensembles of 100 pings every 10 minutes are recorded in 1 m bins. These go from 2.5 m above the bed through the height of the water column to 2 m below the surface, a limiting depth due to increasingly prevalent side-lobes.

Accuracy is generally considered to be 0.2% of the measured current magnitude ± 0.5 cm/s [Lane *et al.*, 1999]. This does depend on several factors including the installation characteristics. For non-zero pitch and roll angles, individual beam velocities are at different vertical depths in the water column and a roll of just 1^o and a current magnitude of 50 cm/s typically introduces errors of 1 cm/s [Ott, 2002], which is 10 times more than the desired 0.2%.

Servicing schedules of the fixed mornings vary seasonally. Regular servicing every 4 – 6 weeks [Howarth *et al.*, 2006] during the summer becomes less frequent during winter when access is weather restricted. For the same reasons the logistics of maintenance and repair have resulted in large gaps within the time series at both locations. Inconsistencies in the current time series can also occur due to different ADCP devices having been deployed at locations A and B.

4.4 Measurement Comparisons

In situ buoy and ADCP measurements have been in common use for a long time now and with familiarity and time grows trust. The agreement between their measurement parameters, taken to be the true value, and those of HF radar is considered a measure of how accurately the HF radar is measuring that particular parameter.

Appendix A table 1, also presented by Robinson *et al.* [2011], shows just a sample of the studies carried out on this topic, some of which are discussed below. Experiments listed utilise a variety of HF radars but generally have either technical, physical or measurement features in common with Liverpool Bay, the NOCL HF WERA radar or their in situ measurement devices. Establishing the industry standards of agreement between measurement devices is important to assess operational working accuracies, not just those based on the sampling and averaging detail of the measurement method.

Robinson *et al.* [2011] and Howarth *et al.* [2007] both showed HF radar and ADCP correlations in Liverpool Bay are > 0.9 for dual current vectors at the ADCP locations and still good, > 0.8 [Robinson *et al.*, 2011], at NHWF. Root mean square (rms) differences of $12-15$ cm/s [Robinson *et al.*, 2011] are found in Liverpool Bay with $2-4$ cm/s attributed to cross-over angles at the ADCP locations.

High correlations between radar and ADCPs are not uncommon, particularly in a region with large tidal amplitudes. High correlations have also been reported for CODAR radars: Kaplan *et al.* [2005] and Kelly *et al.* [2003] calculated correlations > 0.87 at 12.5 and 25 MHz, respectively. Kaplan *et al.* [2005] also found similar rms differences although these are thought to be a larger percentage of the mean current speed than is the case for Liverpool Bay.

Howarth *et al.* [2007] found what they considered to be a reasonable correlation of 0.6 between the phased array HF WERA radar and buoy significant wave height (Hs) in Liverpool Bay. Wolf *et al.* [2007] reported large spatial variability in the Hs measured by the radar in Liverpool Bay reflecting the large variability in local water depth and currents. Other HF radars have however reported much better Hs, for example the Pisces radar used by Wyatt *et al.* [2006] reports Pisces/buoy correlations of up to 0.94. Wyatt & Green [2002] compared measurements between several dual radar experiments using WERA, OSCR, and Pisces radar systems at varying locations. Wyatt & Green [2002] included data from the European Radar Ocean SEnsing (EuroROSE) project [Wyatt *et al.*, 2003], where WERA was tested extensively. In this case WERA HF radar was found to have excellent overall Hs and mean direction correlations of 0.93 and 0.79, respectively, with Hs root mean square errors (rmse) of 0.49 m and mean direction rmse of 27.9^o.

The Hs correlations between radar and buoy in Liverpool Bay are therefore relatively low. This is likely to be due to the absence of long period swell, a Hs with limited range, rarely achieving 5 m, and generally low sea state conditions [Howarth *et al.*, 2007; Kelly *et al.*, 2003]. This is partially confirmed by Wyatt & Green [2009] who report a Hs correlation of 0.82 with rms difference of 0.37 m for a four month period in the winter of 2005 – 2006. During this time an increased number of storm events increased the sea state and validity of the Hs measurement.

Chapter 5

Liverpool Bay HF WERA radar performance

This chapter attempts to characterise the data availability for the HF WERA radar current and wave measurements in Liverpool Bay. As discussed in chapter 2 noise and clutter can both infringe upon a radar's ability to accurately observe its intended target. The characterisation and different sources of noise are discussed along with the definition of noise within the Doppler spectra. Quality control parameters to determine data availability based on noise levels are investigated. The signal to noise ratio for the first and second-order Doppler spectra is also assessed and the spatial differences across the radar footprint are, for the first time, quantified at all operating frequencies, as well as during the day and night. Understanding how the noise levels and signal to noise ratios fluctuate in different operational conditions at different locations will help in the assessment of individual cells where measurements are difficult. Reviewing these parameters spatially will also allow for specific regions of interest to be identified for further investigation.

5.1 Noise

Radar performance is determined from measurement criteria dependent on the noise level and resulting signal to noise ratios of the first and second-order Doppler spectra. Figure 5.1 demonstrates the ideas behind establishing the noise level as done in the Seaview Sensing Ltd. software utilised by NOCL. First the Doppler spectral amplitudes have been ranked in order. The median value of the smallest 10% of data is then found and taken to be the noise level of the Doppler spectra. This is effectively the average of the 486^{th} and 487^{th} value when ranked as in figure 5.1.

Spectral amplitudes are a combination of all scattering objects and surfaces

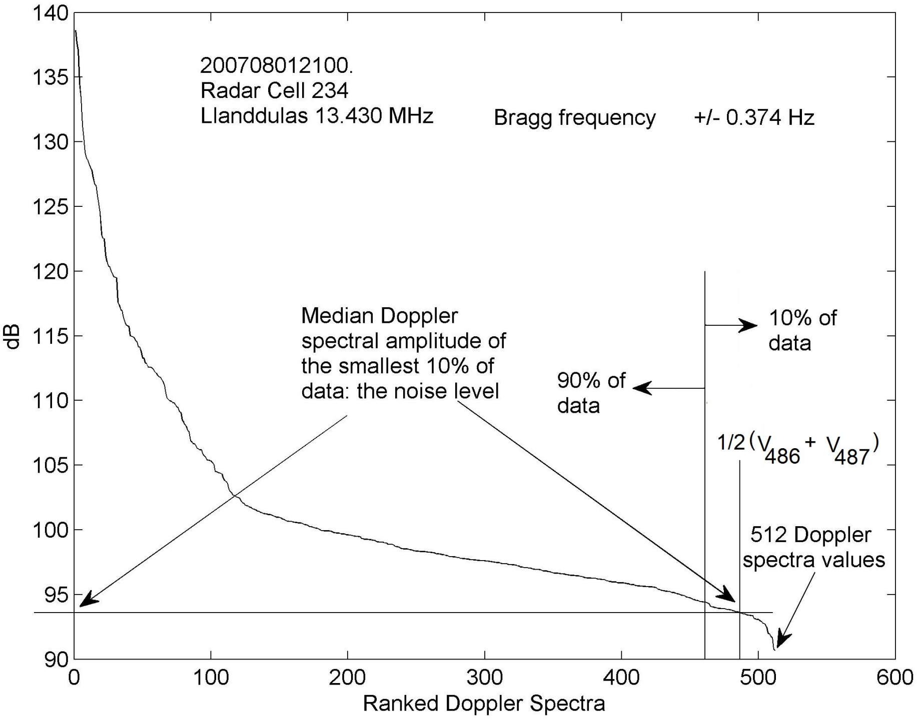

Figure 5.1: A ranked Doppler spectrum for establishing the noise level for WERA HF radar data processing at the Liverpool Bay Coastal Observatory.

within the radar footprint as well as thermal electrical noise and any other outside influences. By observing the spatial plots of average noise, figures 5.2, 5.3 and 5.4, it can be seen that in the presence of wind turbine interference (WTI) noise levels are significantly elevated.

Three main subsets of the radar time series have been investigated:

- January 2006 to January 2007, for pre BBWF construction.
- October 2007 to July 2009, for post BBWF but pre RFWF.
- October 2009 to June 2010, for post BBWF and post RFWF.

Figure 5.2 shows the Formby and Llanddulas average noise for 2006. Each is plotted on the same scale making it exceptionally clear that the Formby noise levels are roughly 6 dB lower than Llanddulas. This is across the entire footprint including at the NHWF location, the source of peak average noise for this period.

To investigate the individual radar's response to the same noise level change, each data set was broken up into two subsets of day and night. The height of the ionosphere and concentration of the ions within it varies between day and night.

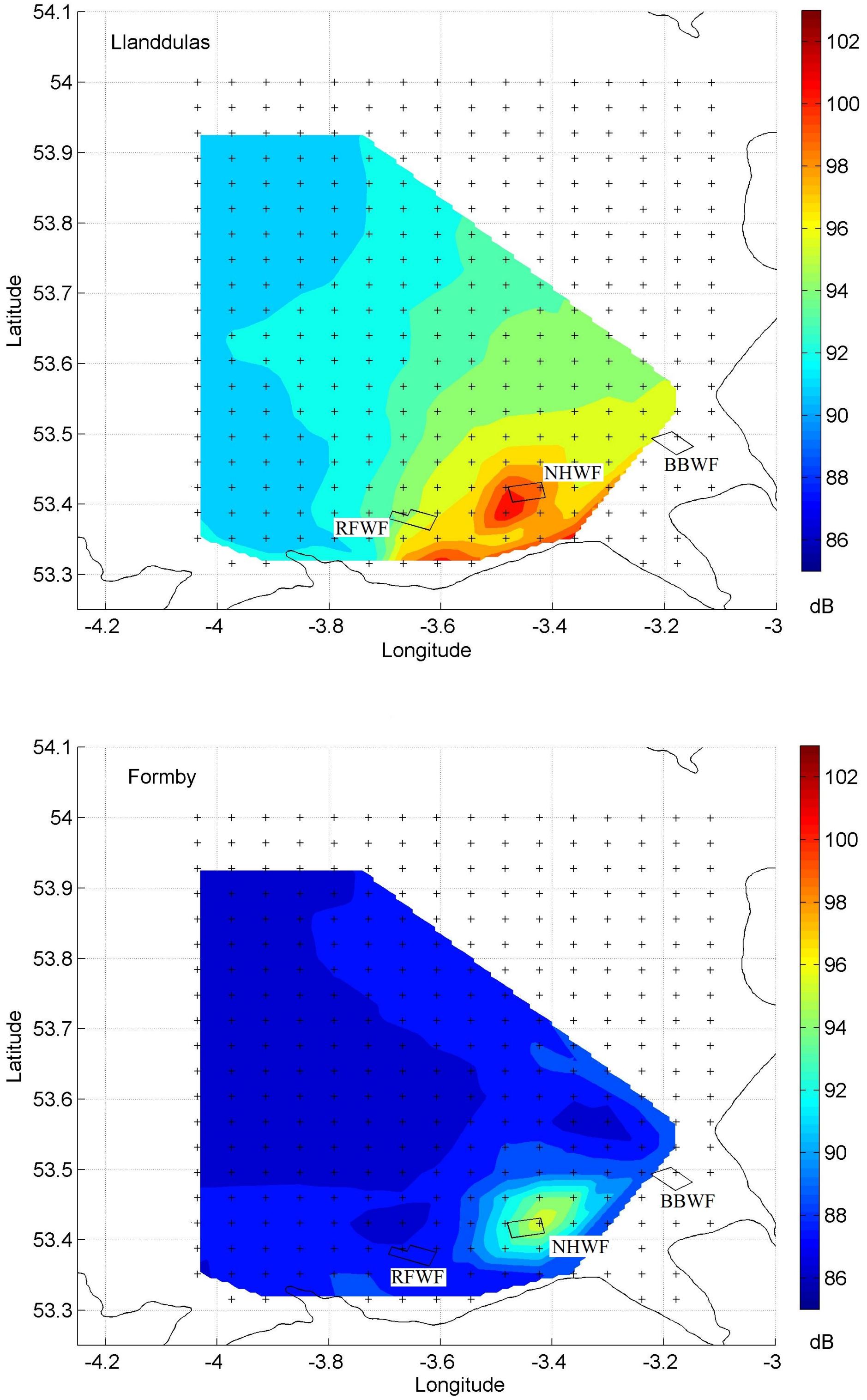

Figure 5.2: Average Doppler spectra noise levels for the HF WERA radar at Llanddulas and Formby for the year 2006.

This is caused by a fluctuation in the amount of ionising radiation reaching a particular section of the Earth's atmosphere, as such it will also vary with solar output [Hulburt, 1957]. Ionospheric effects are expected to cause less interference at night due to fewer ions in the ionosphere. The difference will be the same for both radars and this ionospheric effect would be expected to result in equal noise floor changes at each radar. Figures 5.3 and 5.4 show this is not the case.

Comparing the Llanddulas and Formby day and night figures, 5.3 and 5.4, we see that Formby has roughly a 4 dB noise drop at night whereas Llanddulas has a drop of around 6 dB. This 2 dB difference could be in part due to the location of each site. The Formby radar will experience very similar conditions both day and night but Llanddulas is situated near a busy road and rail track. These are primarily active during the day and could account for the additional 2 dB drop at night for the Llanddulas Doppler spectra. This cannot however account entirely for the noise characteristic differences between sites. Figures 5.3 and 5.4 show the noise levels at Llanddulas never get as low as at Formby with a 3 dB difference still evident. Other site characteristics at Llanddulas such as high fencing and transmit and receive antenna height difference will also be contributing factors and as such Llanddulas is generally regarded as a 'noisy' radar site.

On the 18^{th} of October 2007 the radar footprint had a significant change in the noise characteristics as BBWF became operational. BBWF is slightly outside the normal measurement criteria for currents due to its location but it is covered by the radar footprint and Doppler spectra are recorded at its location.

Averaging over an area larger than that normally used for currents we are able to see the impact of a wind farm being introduced to Liverpool Bay. As shown in figure 5.5, the noise level is considerably higher at radar cells co-located with BBWF. Due to the small angle from boresight and proximity of the Formby radar, BBWF is the prominent feature in the average noise plot from Formby.

Figure 5.6 shows the average noise for Llanddulas and Formby over the measurement period from October 2007 to July 2009. This period is after the BBWF is operational but before any power is exported from the RFWF. Figure 5.6 shows again that Formby has lower average noise levels than Llanddulas and that the NHWF environment is still a region with elevated noise levels. Each wind farm is located over several radar cells, and even with the reduced area BBWF is introducing noise to radar cells 274 and 275. This can be seen from Formby but is obscured at Llanddulas due to the NHWF and the wide angle look direction.

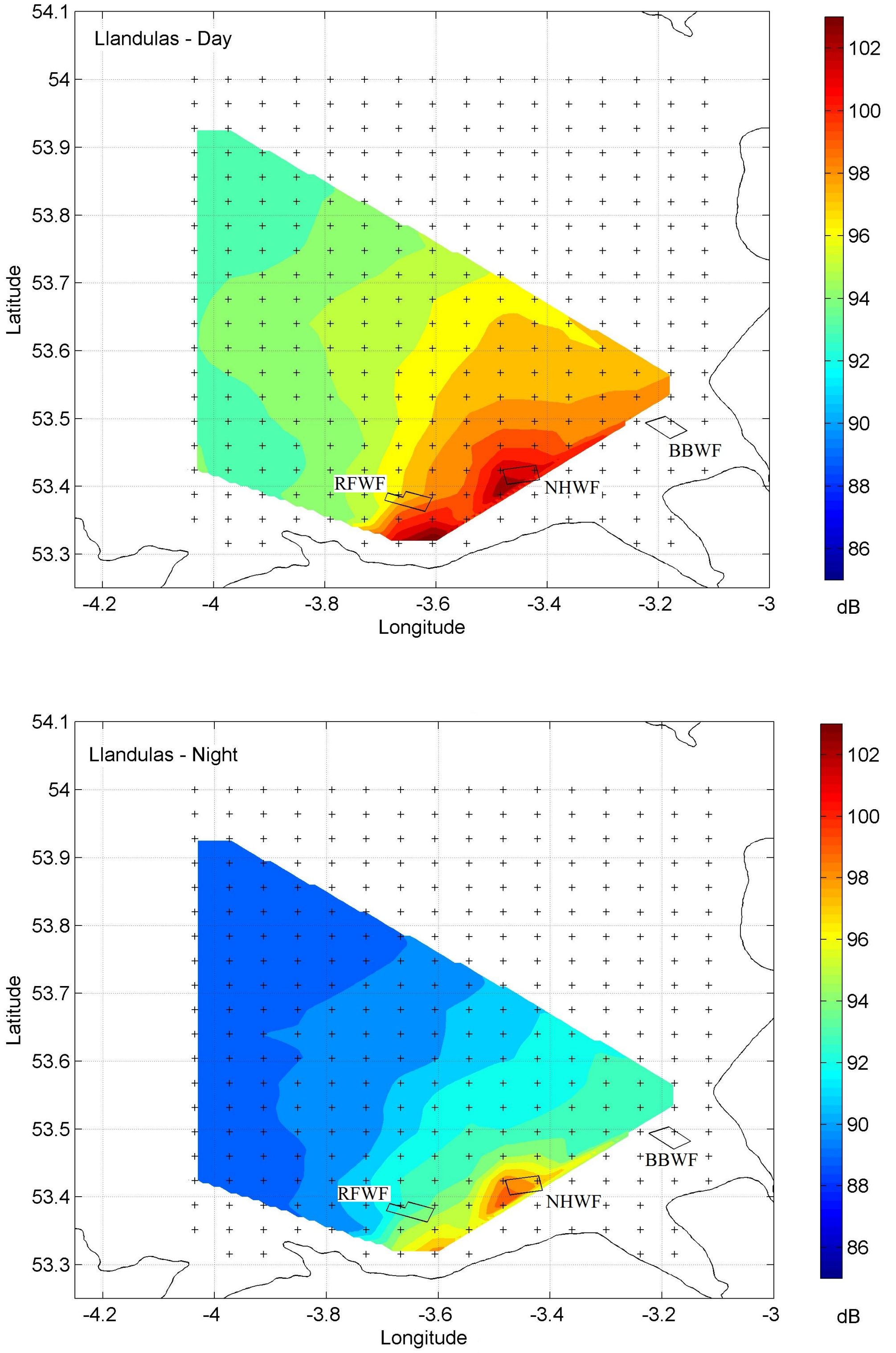

Figure 5.3: Average Doppler spectra noise levels for the HF WERA radar at Llanddulas during the core day and night hours. Measurement period August 2005 to October 2007.

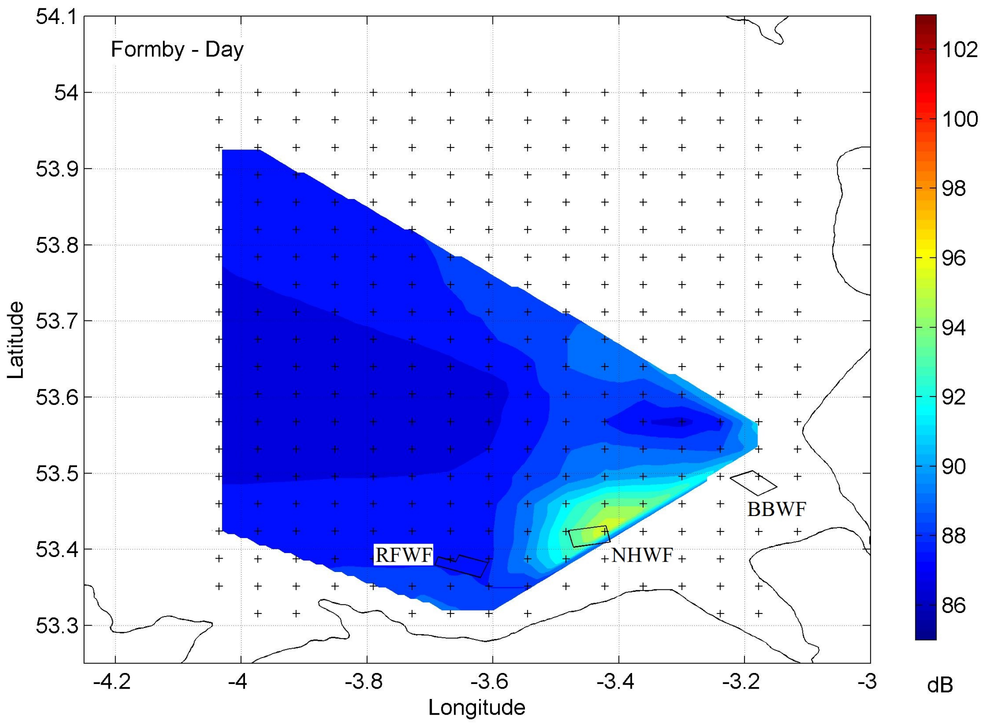

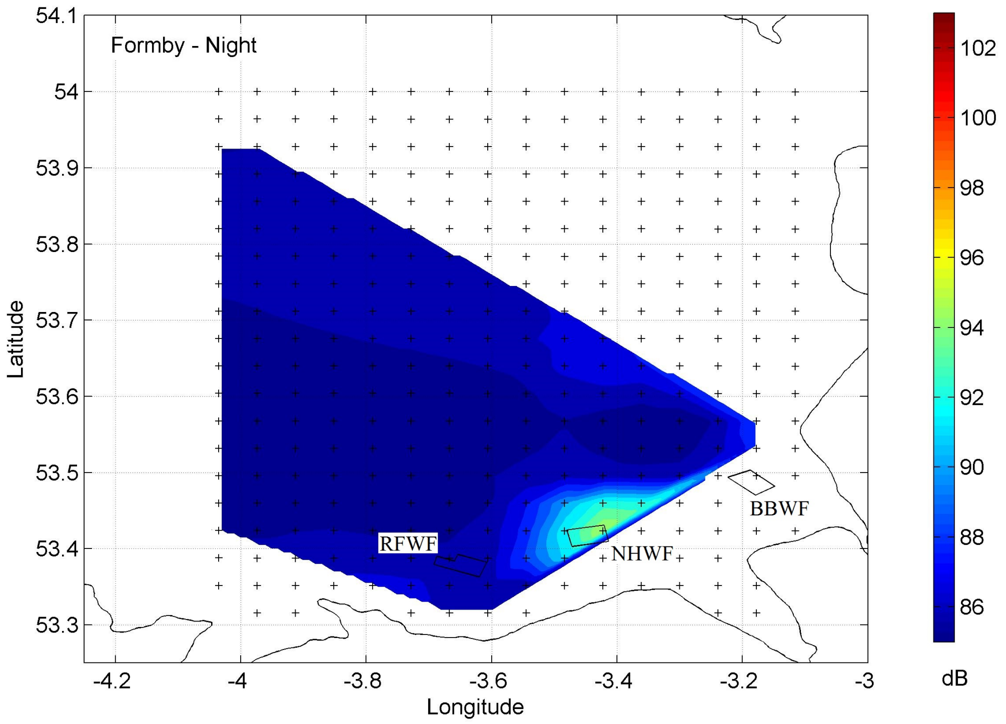

Figure 5.4: Average Doppler spectra noise levels for the HF WERA radar at Formby during the core day and night hours. Measurement period August 2005 to October 2007.

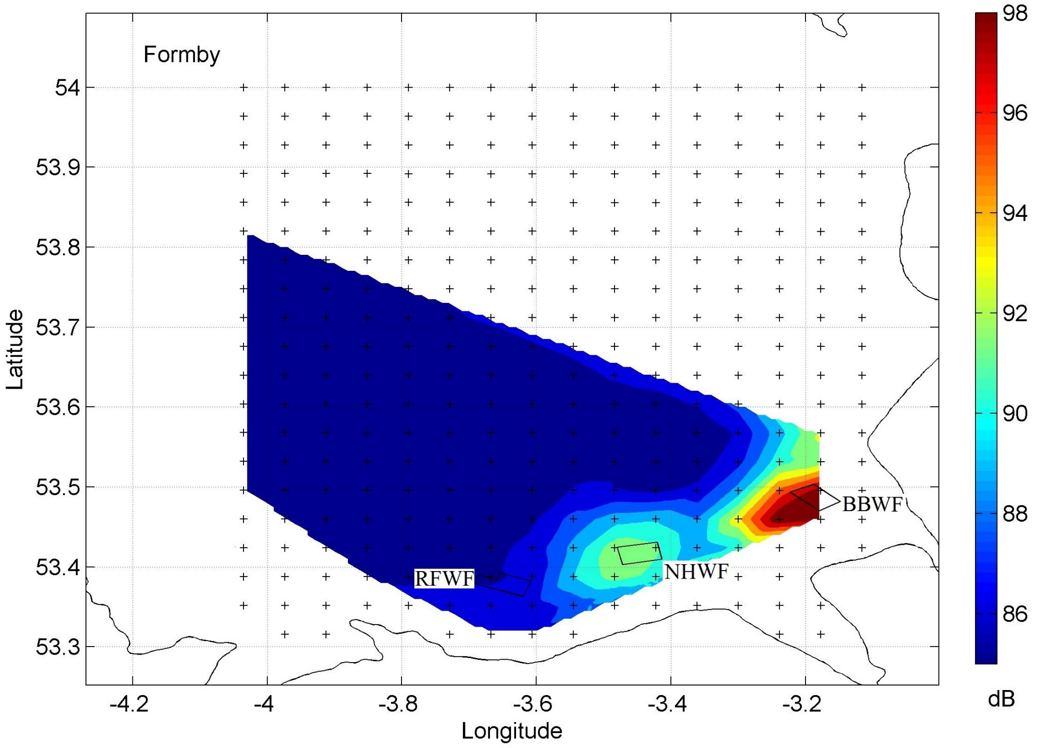

Figure 5.5: Formby Average noise for an extended area. Data period is October 2007 to July 2009, for post BBWF but pre RFWF.

The RFWF became fully operational in December 2009. After this time we can see in figure 5.7 that a region of previously low noise levels is now dominating the average noise spatial plot for the Llanddulas Doppler Spectra. Llanddulas has roughly a 10 dB rise in the average noise levels of the Doppler spectra with the introduction of the RRWF. Formby on the other hand does not see a variation of more than 1 dB compared to other measurement periods. This will be in part due to the different aspects of the RFWF causing a variation in the RCS. The distance to each radar will also affect the noise, and cells co-located with BBWF remain the cells with the highest average noise, as viewed by Formby, most likely due to its proximity.

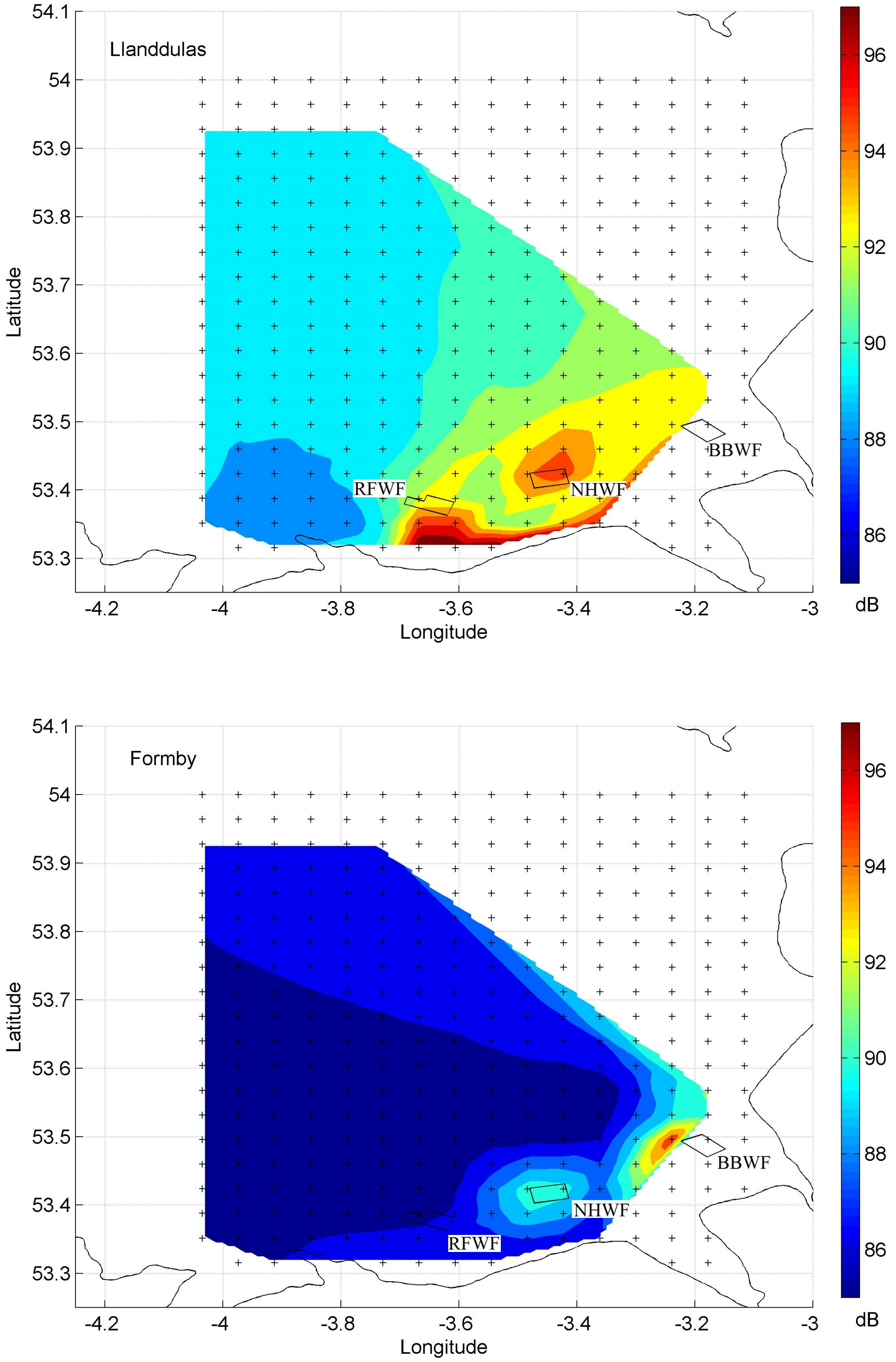

Figure 5.6: Average Doppler spectra noise levels for the HF WERA radar at Llanddulas and Formby for the measurement period October 2007 to July 2009.

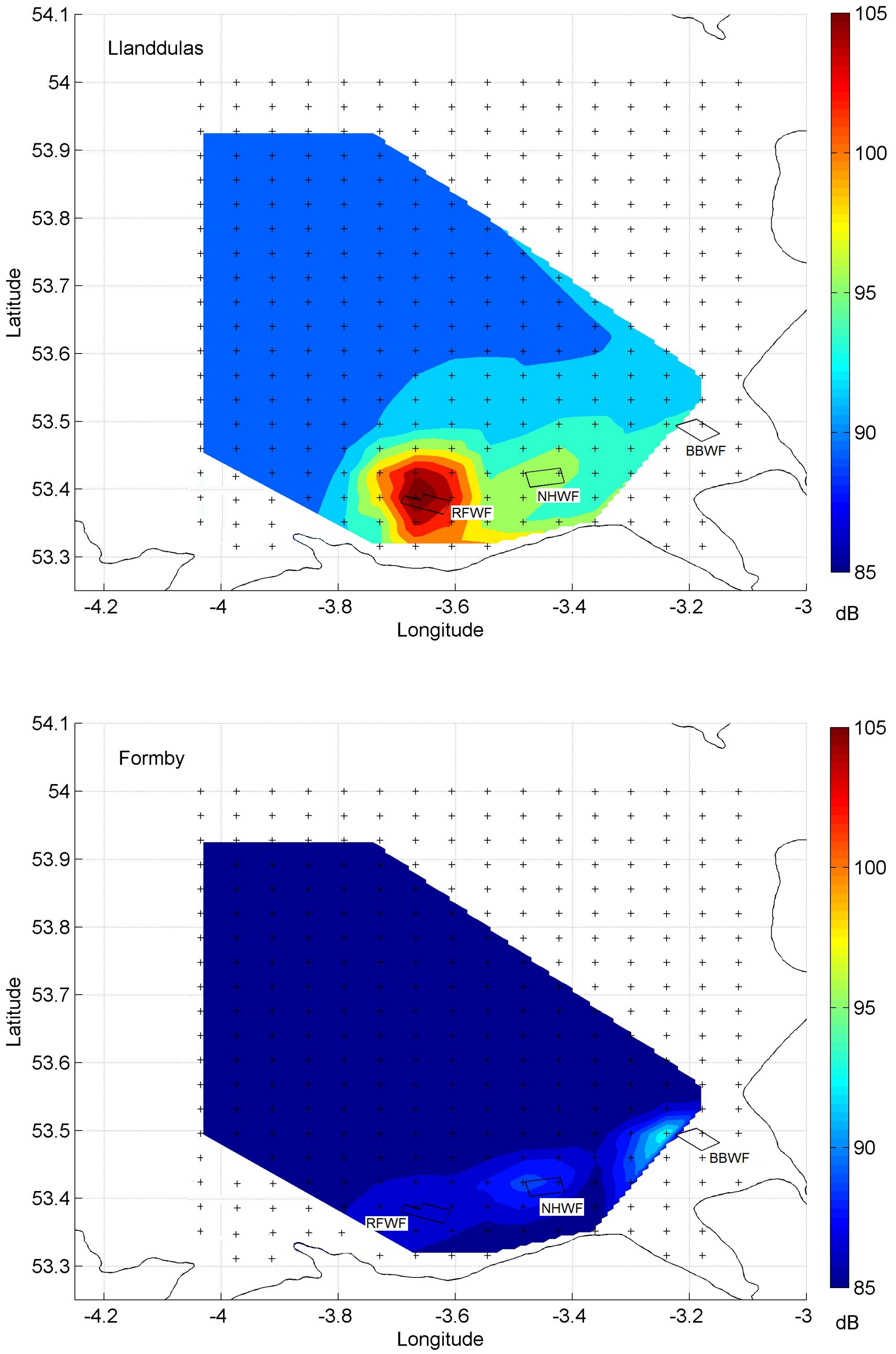

Figure 5.7: Average Doppler spectra noise levels for the HF WERA radar at Llanddulas and Formby for the measurement period October 2009 to June 2010.

5.2 Data availability

Although installed in 2004 the HF radar experienced some operational problems and the long running continuous time series is considered to start in August 2005. The Liverpool Bay HF radar measurement period is therefore taken to be from August 2005 until December 2011. Spectral data, resolved onto a 300 cell grid, were available for over 98% of the deployment with small time gaps occurring due to maintenance. Doppler spectra of cells with a first-order superior signal to noise ratio (SNR) of 10 dB or more were processed for radial currents. Of the available Doppler spectra, over 99% at both Formby and Llanddulas were able to be processed into radial currents and over 90% into vector currents for the small revised current measurement area shown in figure 4.1. Cells close to the radar footprint edge and at the greatest distances had a slightly lower availability for radial current measurements of 85% or more. This is due to the signal strength falling off with distance therefore fewer measurements passing the 10 dB thresholding. When shorter time series are used measurement gaps can be proportionally larger and this is considered on a case by case basis when analysing a particular section of data.

Second-order Doppler spectral processing for wave measurements requires better quality data than when resolving for currents alone. Having established the noise floor in the spectra and passing the current thresholding, the Doppler spectra were again filtered for a peak second order SNR ratio of 15 dB or more and a difference between the first and second-order peaks of at least 5 dB. During the radar deployment the beam angle for certain cells where measurements were routinely made was deemed too wide for accurate current and wave measurements. Because of this the current and wave area was reduced. This is discussed further in chapter 7.

Taking a 3 month period, when the RFWF was in full operation, the data availability at co-located cells does not appear to be affected. Both Llanddulas and Formby have high availability, 97% and 96% respectively. After current thresholding 99% of radial data at Llanddulas and 96% at Formby was considered valid and suitable for the full current vector calculation. The percentage of these measurements passing the wave data quality controls was highly variable between individual radar cells. Llanddulas has an average availability of 60% ± 18% and Formby 23% ± 20% with maxima of 93% and 88%, respectively. Due to the high variability over the radar footprint it is not apparent that RFWF has influenced wave data availability when considering long time series statistics.

5.3 Frequency Operation

The radio spectrum ranges from roughly 3 Hz to 300 GHz. Today's world is dependent on devices and communication via radio waves and as such frequency bands have become an internationally regulated commodity with strict allocation and permitted operation. Above a certain power, transmission is by licence only and certain frequency bands can be particularly crowded.

The Liverpool Bay HF WERA radar operated at 6 different frequencies listed in table 4.3. This allows the radar performance to be assessed looking for any advantage of one frequency over another. The data passing the current and wave thresholds from the Formby radar is almost equally split amongst the 3 frequencies used with maximum differences of 0.5%. Figure 5.8 shows that for the Llanddulas radar, some cells have a higher availability of wave data at a particular frequency. The data at radar operating frequency 13.465 MHz accounts for approximately 1.5% more of the data passing quality control in certain regions. The fact that it is not uniform over the radar footprint suggests the RFI might be directional.

Radar data for the improved measurement availability at 13.465 MHz was investigated for agreement with fixed moorings. Comparisons were made between radar cell 194 and measurements with ADCP A and the WaveRider buoy located at cell 234. Cell 234 and 194 are approximately 8 km apart with a greater depth of water at cell 194. Radar cell 234 itself was not used due to increased spatial variability in currents, greater shipping presence and higher noise levels, being roughly 2 dB greater than at cell 194, resulting in slightly fewer measurements. As such cell 194 is thought to perform better.

Correlation with ADCP data does not differ between the operational frequencies. This is found for both Llanddulas radial currents, see table 5.1, and dual current measurement components, see table 5.2. The current correlations with ADCP in table 5.1 appear low. This is due to the look direction of the Llanddulas radar to cell 194. Being just 19^o east from direct north it is the smallest current component being measured. This is confirmed in table 5.2 where we see very similar correlations with the north vector component. To maximise wave data availability, operating at 13.465 MHz from the Llanddulas radar is seen in table 5.3 to be preferable. There is an increase in the wave measurement agreement between dual radar and Buoy Hs measurements at 13.465 MHz. This frequency also shows a smaller rms difference between the buoy and radar measurements.

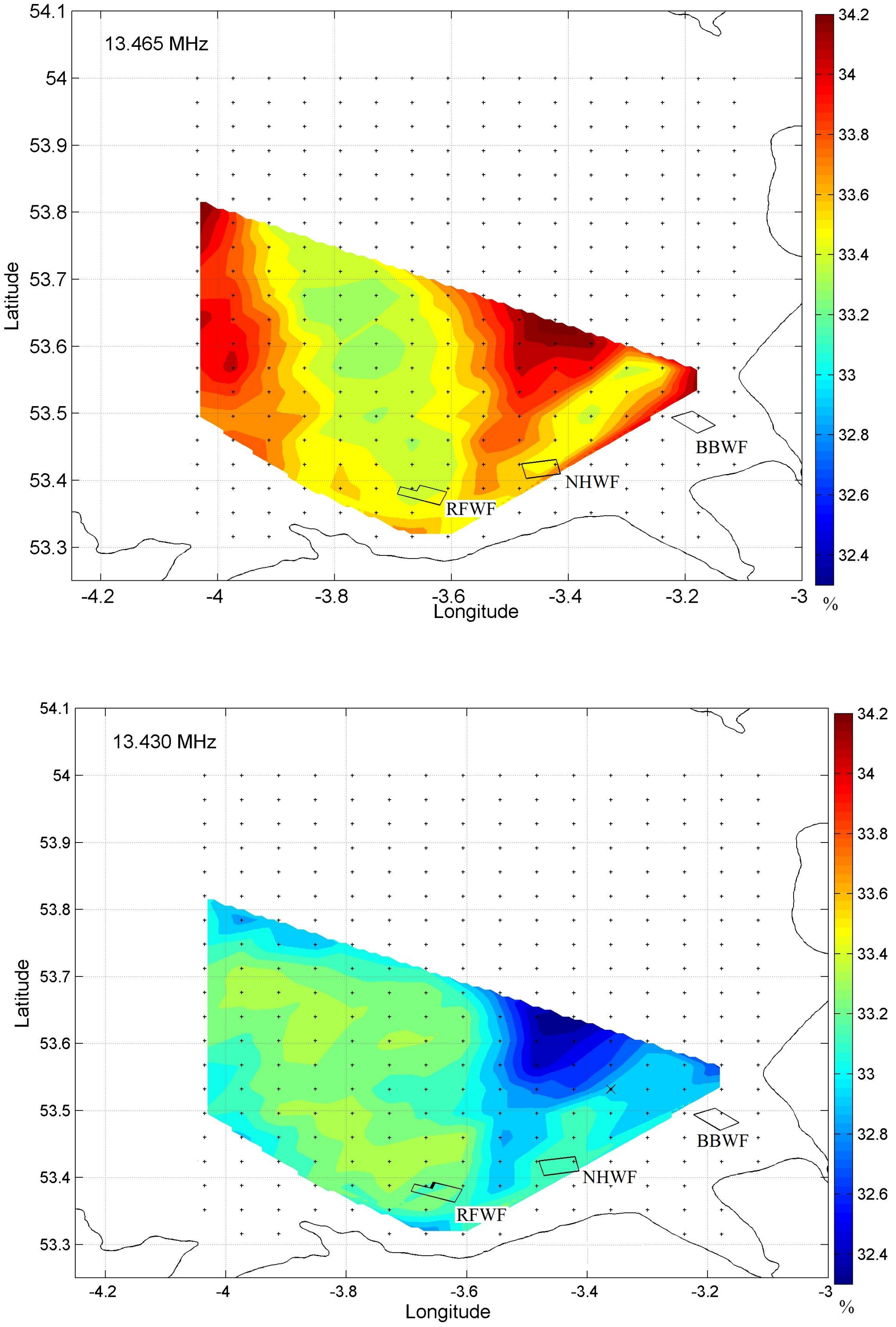

Figure 5.8: The percentage of data passing current and wave thresholds attributed to the Llanddulas frequency operations at 13.465 and 13.430 MHz. Measurement time series is from August 2005 to October 2007.

Llandulas Radial currents: RC194-ADCP A	
Operating Frequency MHz	Correlation r
13.430	0.67
13.465	0.67
13.395	0.68

Table 5.1: Llanddulas radial current measurement, cell 194, correlated with the ADCP A current component in the look direction of the radar (August 2005 - October 2007). RC194 refers to radar cell 194 and r to the correlation value.

Dual Vector current RC194-ADCP A		
Operating Frequency MHz	Correlation r East	Correlation r North
13.430	0.96	0.62
13.465	0.96	0.62
13.395	0.96	0.60

Table 5.2: Vector current measurements, cell 194, correlated with the ADCP A east and north current components (August 2005 - October 2007). RC194 refers to radar cell 194 and r to the correlation value.

Dual Wave Hs RC194-Buoy		
Operating Frequency MHZ	Correlation r	rmsd (m)
13.430	0.57	0.81
13.465	0.61	0.75
13.395	0.56	0.82

Table 5.3: Wave measurements, cell 194, correlation with Buoy measurements (August 2005 - October 2007. RC194 refers to radar cell 194, Hs is the significant wave height, r is the correlation value and rmsd is the root mean square difference.)

Chapter 6

Tidal Analysis

Currents in Liverpool Bay are dominated by strong semi-diurnal tides [Howarth *et al.*, 2007; Prandle, 1991]. As such they are predictable and patterns and trends should be matched by HF radar measurements as well as those from ADCP.

In this chapter the amplitude and phase of the main tidal constituents are investigated using both radar and ADCP current time series. A residual current time series is constructed and used to investigate wind-driven surface effects.

6.1 The Tides

Tides manifest themselves in two ways. These are described by Pugh [1996] *"as both the vertical rise and fall of sea-level, and the to and fro movements of the water currents"*. The range and period of the tidal cycles are the key properties for shore based tidal observation and have been published for thousands of sites worldwide. This is done from observations of tide behaviour, typically making measurements with tide gauges. Tide gauges measure the sea level height relative to the lowest level ever expected at a site, also referred to as the site datum, and can be related to mean sea level. The design has varied over the years from early staff gauges to more modern bubble gauges with combined chart recorders and, more recently, pressure sensors with digital data loggers. Large tide networks are now established with automated central data collection that allow real time tide levels and highly accurate predictions via web based applications. Admiralty EasyTide, available at www.easytide.ukho.gov.uk, is one such example with tidal predictions going as far back as 100 AD and indefinitely into the future. Such predictions are possible due to the nature and consistency of the celestial forcing bodies, which are considered constant over the period of Earth's history. Pugh [1996] gives a comprehensive account of celestial forcing combinations however the three main categories of celestial forcing, as summarised by Radock [1999], are:

- 1) Semi-diurnal - a period or cycle of approximately one half of a solar, or lunar, day
- 2) Diurnal - a period or cycle of approximately one solar, or lunar, day
- 3) Mixed - a combination of both semi-diurnal and diurnal tides

As for any wave, a complicated tidal series can be described as the summation of a series of sinusoidal oscillations with specific amplitude, frequency and phase. These are referred to as tidal harmonics and each belongs to one of the three categories mentioned above. Table 6.1 lists ten common tidal harmonics, of which there are over 60, and their phase speed.

Tidal Constituent	Frequency (cycles/hr)	Phase Speed (^{o}/hr)
O_1	0.0448	13.943
K_1	0.04178	15.041
N_2	0.079	28.440
M_2	0.08051	28.984
S_2	0.08333	30.000
K_2	0.08356	30.082
M_4	0.1610	57.968
MS_4	0.1638	58.984
S_4	0.1667	60.000
M_6	0.24153	86.952

Table 6.1: Ten common tidal constituents and their phase speeds.

Particular tidal species are identified with a combination of coded letters and a subscript number, for examples see table 6.1. The subscripts 1 and 2 identify the harmonic as diurnal and semi diurnal respectively but can also indicate harmonics. Examples include K_1, a diurnal harmonic component associated with changes in the lunar-solar declination, and M_2, a semi diurnal constituent, the result of the lunar positional cyclic changes relative to the earth [Emery & Thomson, 2001].

The harmonic analysis of tides, referred to as tidal analysis, is the process of decomposing a tidal series into harmonic constituents. With periods matching those that force it, specific frequencies contributing large amplitudes can be selected. When the amplitude of each tidal constituent is known for a given region the tidal series can be reconstructed. Tidal parameters can also be mapped to describe the tidal characteristics of a region [Pugh, 1996]. This is a useful technique in predicting tides for shipping and developing understanding of tidal forcing and the effects it has on the hydrodynamics of the sea. The harmonic analysis method is a well utilised tool in oceanography [Ebuchi *et al.*, 2006; Graber *et al.*, 1997; Howarth *et al.*, 2007; Kelly *et al.*, 2003; Prandle, 1987]. It can be utilised in many situations as a technique for best fitting models to data.

6.2 Least squares tidal analysis

In this section the method of least squares tidal analysis, as it has been applied in investigating the Liverpool Bay tidal constituents by Robinson *et al.* [2011], is summarised following Emery & Thomson [2001].

In tidal analysis the time series is used to determine the harmonic constituent amplitudes A_q and B_q for M specified frequencies where $q = 0, 1, \ldots, M$ giving $2M + 1$ harmonic coefficients. Assuming that $2M + 1 << N$, where N is the number of observations of the Δt sample time, the record length will be $T = N\Delta t$. The M frequency amplitudes, ξ_M, can then be obtained using

$$\xi_M = \sqrt{A_q + B_q} \tag{6.1}$$

and the phase, ψ_M, by

$$\psi_M = \tan^{-1}(B_q/A_q) \tag{6.2}$$

The power spectra, P$_M$, can also be calculated from the sum of the squares of the A_q and B_q coefficients

$$P_M = A_q^2 + B_q^2 \tag{6.3}$$

A_q and B_q are obtained by minimising the squared difference between the original data and the model of the specified frequency.

To solve for the A_q and B_q coefficients a matrix equation of the form $\mathbf{y} = \mathbf{D}z$ is solved for z with

$$z = \mathbf{D}^{-1}y \tag{6.4}$$

where $\mathbf{D}^{-1}$ is the inverse matrix of

$$\begin{vmatrix}
N & c_1 & c_2 & \cdots & c_M & s_1 & s_2 & \cdots & s_M \\
c_1 & cc_{11} & cc_{12} & \cdots & cc_{11M} & cs_{11} & cs_{12} & \cdots & cs_{1M} \\
c_2 & cc_{21} & cc_{22} & \cdots & cc_{2M} & cs_{21} & cs_{22} & \cdots & cs_{2M} \\
\cdots & \cdots & \cdots & \cdots & \cdots & \cdots & \cdots & \cdots & \cdots \\
\cdots & \cdots & \cdots & \cdots & \cdots & \cdots & \cdots & \cdots & \cdots \\
c_M & cc_{M1} & cc_{M2} & \cdots & cc_{MM} & cs_{M1} & cs_{M2} & \cdots & cs_{MM} \\
\cdots & \cdots & \cdots & \cdots & \cdots & \cdots & \cdots & \cdots & \cdots \\
s_1 & sc_{11} & sc_{12} & \cdots & sc_{1M} & ss_{11} & ss_{12} & \cdots & ss_{1M} \\
s_2 & sc_{21} & sc_{22} & \cdots & sc_{2M} & ss_{21} & ss_{22} & \cdots & ss_{2M} \\
\cdots & \cdots & \cdots & \cdots & \cdots & \cdots & \cdots & \cdots & \cdots \\
s_M & sc_{M1} & sc_{M2} & \cdots & sc_{MM} & ss_{M1} & ss_{M2} & \cdots & ss_{MM}
\end{vmatrix}$$

Matrix D is $(2M+1)$ x $(2M+1)$ in size and constructed using equations 6.5 to 6.9.

$$c_k = \sum_{n=1}^{N} \cos \frac{2\pi\alpha_k n}{N} \tag{6.5}$$

$$s_k = \sum_{n=1}^{N} \sin \frac{2\pi\alpha_k n}{N} \tag{6.6}$$

$$cc_{kj} = cc_{jk} = \sum_{n=1}^{N} \cos \frac{2\pi\alpha_k n}{N} \cos \frac{2\pi\alpha_j n}{N} \tag{6.7}$$

$$ss_{kj} = ss_{jk} = \sum_{n=1}^{N} \sin \frac{2\pi\alpha_k n}{N} \sin \frac{2\pi\alpha_j n}{N} \tag{6.8}$$

$$cs_{kj} = sc_{jk} = \sum_{n=1}^{N} \cos\frac{2\pi\alpha_k n}{N} \sin\frac{2\pi\alpha_j n}{N} \tag{6.9}$$

y and **z** are the column vectors

$$\mathbf{y} = \begin{vmatrix} yc_0 \\ yc_1 \\ yc_2 \\ \vdots \\ \vdots \\ yc_M \\ ys_1 \\ \vdots \\ ys_M \end{vmatrix} \qquad \textit{and} \qquad \mathbf{z} = \begin{vmatrix} A_0 \\ A_1 \\ A_2 \\ \vdots \\ \vdots \\ A_M \\ B_1 \\ \vdots \\ B_M \end{vmatrix}$$

and the elements of **y** are given by equations 6.10 and 6.11.

$$yc_k = \sum_{n=1}^{N} x_n \cos\frac{2\pi\alpha_k n}{N} \tag{6.10}$$

$$ys_k = \sum_{n=1}^{N} x_n \sin\frac{2\pi\alpha_k n}{N} \tag{6.11}$$

where $\alpha_k = f_k T$ and $\alpha_j = f_j T$, $k = 0, 1, \ldots, M$, $j = 1, \ldots, M$ and both have frequency units s^{-1}.

The time series that is required for this type of analysis must be at least the length of the longest tidal constituent hoped to be resolved. Another common signal processing technique to resolve a time series into its frequency constituents is the Discrete Fourier Transform (DFT), as given by equation 6.12.

$$X(k) = \sum_{n=0}^{N-1} x(n) e^{-j\omega_k n} \tag{6.12}$$

where $\omega_k = \frac{2\pi k}{N}$ [Rabnier & Gold, 1975].

The DFT is a transform technique that decomposes a discrete time series, x(n), of N samples into its constituent frequencies and their relative amplitudes. This is in effect doing the same thing as the tidal analysis but for all N integer multiples of the fundamental rather than just a select few. When the tidal forcing frequencies are so specifically known, tidal analysis can easily extract the amplitudes of the required frequencies and ignore all others. With the DFT, tidal amplitudes are not easily picked out and are at frequencies that are multiples of the frequency spacing in the spectra and not necessarily the forcing frequencies. As such energy can be spread over several frequency bins. Tidal analysis is also less intensive computationally due to this reduction in frequencies. These issues are illustrated by comparing figures 6.1 and 6.2. Another big advantage is its ability to incorporate large gaps and missing data points easily whereas some interpolation is often required with the DFT. This is particularly useful with oceanographic data in general and radar in particular where small data gaps are common.

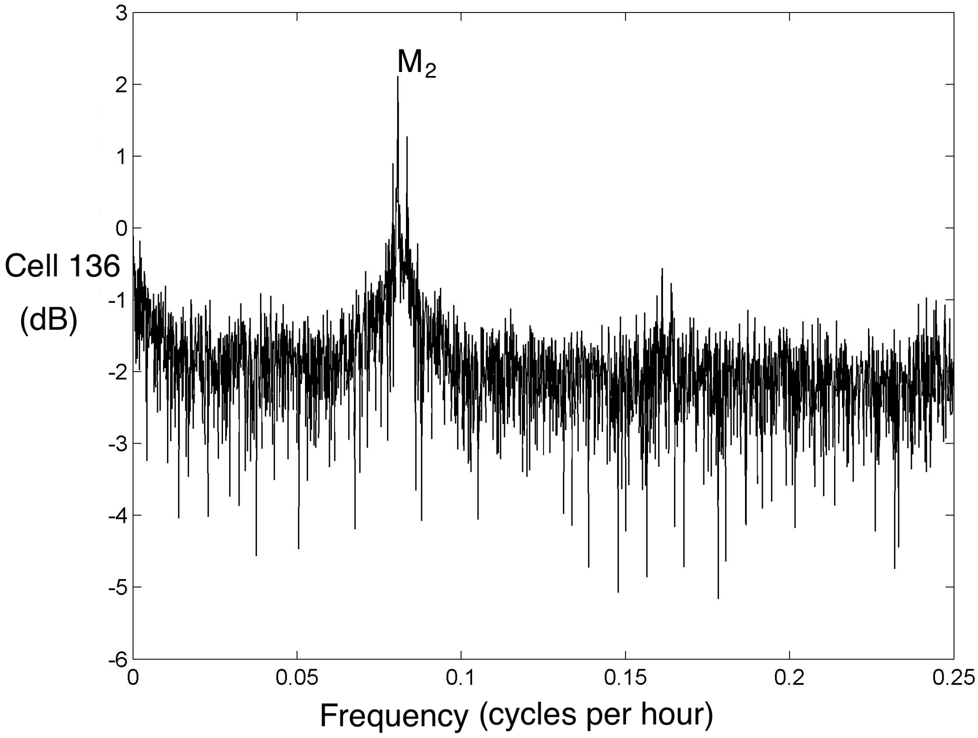

Figure 6.1: The decomposition of the east current time series of 2006 from radar cell 136 into constituent frequencies and amplitudes using the Discrete Fourier Transform.

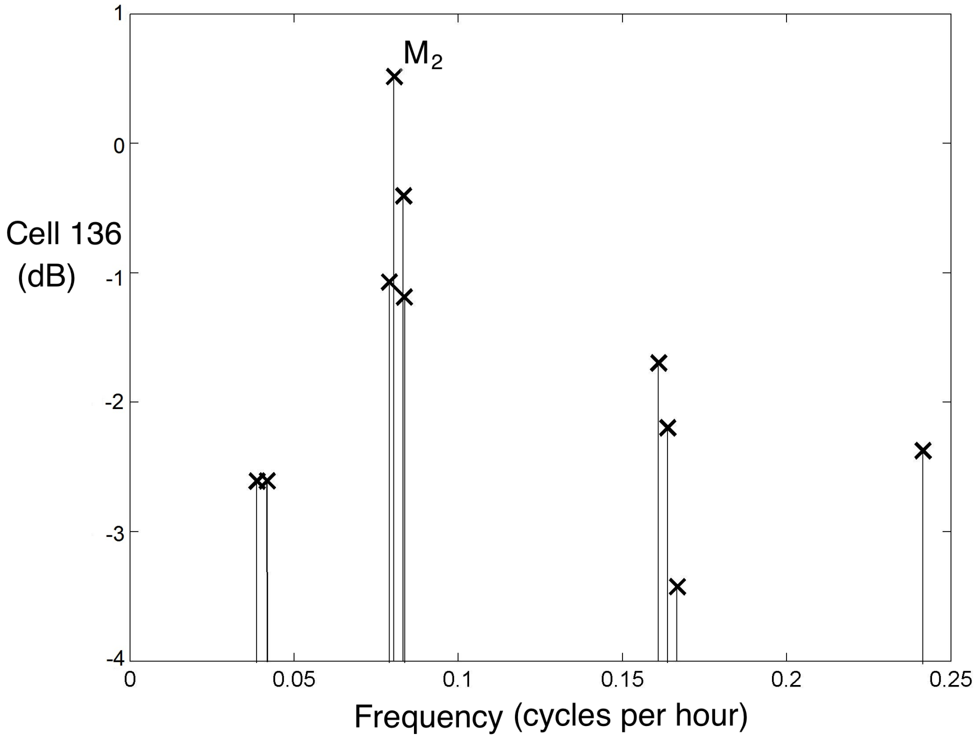

Figure 6.2: The decomposition of the east current time series of 2006 from radar cell 136 into constituent frequencies and amplitudes using Harmonic analysis.

6.3 Liverpool Bay tidal analysis

Least squares harmonic analysis was applied to the discrete data series of the ADCP and HF radar east (u) and north (v) currents. The celestial forcing frequencies solved for are those detailed in table 6.1. The results and analysis reported in this section were first published by Robinson *et al.* [2011] as part of a larger study which is further detailed in chapter 7.

Howarth *et al.* [2007] found over 90% of the observed currents in Liverpool Bay can be accounted for by tidal forcing. The semi-diurnal constituents, N_2, M_2, S_2, and K_2 are seen in figures 6.1 and 6.2 to make large contributions. The tidal ellipse is the envelope of the current vector as a particular tidal frequency moves through one complete cycle. The ellipse parameters (amplitude and phase) for the largest constituent, M_2, were used by Howarth *et al.* [2007] and Robinson *et al.* [2011] as a quality control indicator for comparing ADCP and HF radar current measurements. The results here are also presented in Robinson *et al.* [2011].

Table 6.2 shows tidal analysis results covering the two year period from January 2006 to December 2007. It gives the percentage of energy contributed by each of the 10 tidal constituents and their totals. Figures given in table 6.2 were calculated by reconstructing the decomposed signal using the M frequencies resolved for and the A_q and B_q coefficients. These were then statistically compared with the original time series to first of all assess the method. Correlations between the original u and v times series and that reconstructed using all 10 frequencies are found to be over 0.96 and 0.68, respectively, with rms differences of below 2 cm/s. This shows the decomposition to be producing good amplitude and phase values. Secondly, the percentage contribution from each constituent was calculated by signal reconstruction using individual frequencies and assessing how much it accounted for the tidal variance.

Tidal Frequency	Radar 234 u	Radar 234 v	ADCP A_{ab18} u	ADCP A_{ab18} v	Radar 136 u	Radar 136 v	ADCP B_{ab20} u	ADCP B_{ab20} v
O_1	0.020	0.10	0.03	0.048	0.023	0.029	0.019	0.028
K_1	0.017	0.092	0.02	0.073	0.029	0.031	0.032	0.14
N_2	2.24	1.06	2.63	0.86	1.73	1.41	1.83	0.84
M_2	77.72	22.51	78.89	33.86	79.25	29.89	77.36	40.99
S_2	9.34	3.25	10.1	5.46	9.48	6.08	10.68	6.34
K_2	2.23	1.14	2.1	1.09	1.49	1.53	1.69	1.06
M_4	0.23	0.66	0.22	1.44	0.29	0.44	0.15	0.12
MS_4	0.038	0.21	0.043	0.33	0.036	0.017	0.0066	0.015
S_4	0.0026	0.0007	0.0017	0.023	0.0022	0.0011	0.0012	0.020
M_6	0.042	0.0097	0.018	0.048	0.021	0.067	0.053	0.16
Total	91.9	29.0	94.1	43.2	92.4	39.5	91.8	49.7

Table 6.2: Percentage of tidal energy contributed by specific frequencies. The 2 year time series of east (u) and north (v) current components are from HF radar cells 234 and 136 and their co-located ADCP A and B, respectively. Subscript numbers represent the height above the bed (ab).

Liverpool Bay is dominated by an east-west current with 91% or more of the u tidal energy being attributed to just these 10 tidal frequencies. Within that total the energy at a specific frequency varies greatly depending on the constituent. In the case of ADCP A_{ab18} u component at 18 m above the bed we see a maximum contribution of 77% from M_2 with just 0.2 percent from S_4. There is a lot less tidal energy in the v current component, as expected, however the M_2 constituent is responsible for 75% of the total. This is less than the 85% u M_2 contribution to the total but still the most significant. An extended set of 20 frequencies were tested, but these only accounted for an additional 1% of tidal energy.

Results in table 6.2 from the ADCP and radar show excellent agreement in the contributions from each frequency. The radar and ADCP M_2 ellipse, as shown in figure 6.3, have phase agreement within 3^o and amplitude differences are small (2 cm/s). For a tidally dominated region this high level of agreement is not unexpected. Using an OSCR deployed in an earlier HF radar experiment in Liverpool Bay Prandle [1987] found the semi-major M_2 tidal frequency axis to be mutually consistent spatially with an agreement of less than 0.5 cm/s between radar cells.

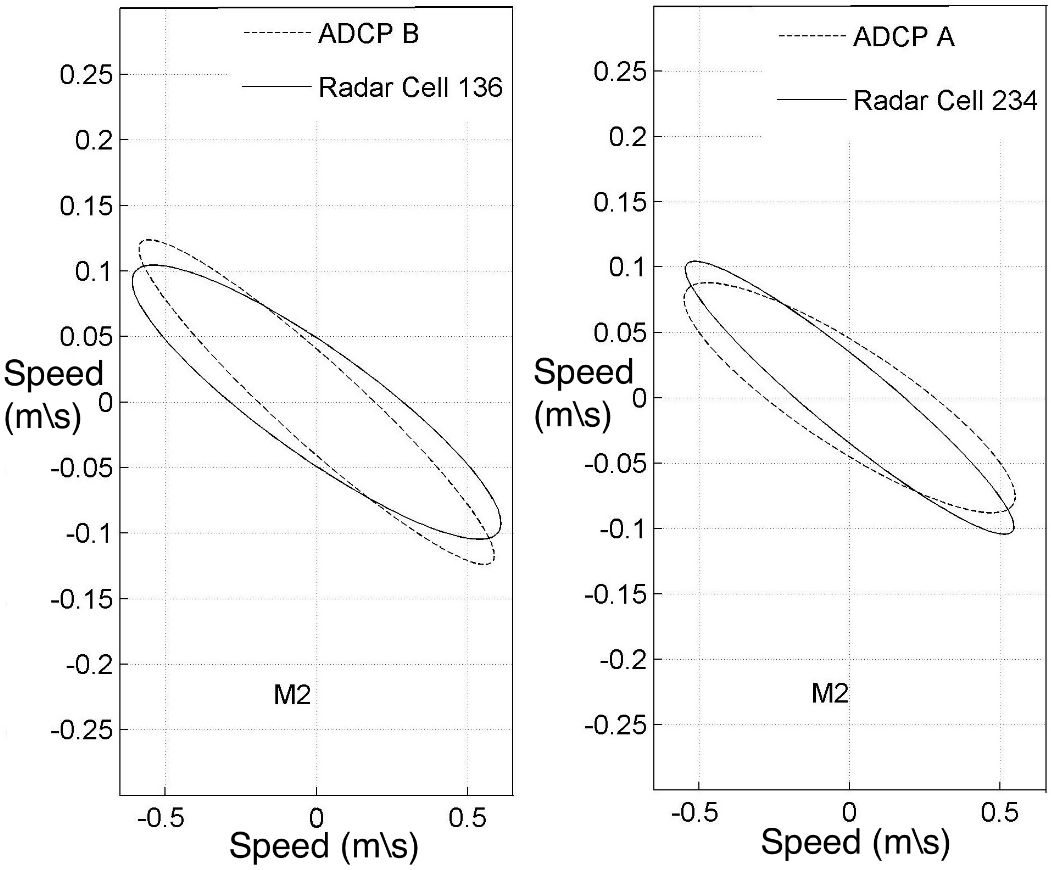

Figure 6.3: M_2 tidal ellipse from the east current time series measured at the co-located HF radar cell 234 and ADCP A and cell 136 and ADCP B.

Having reconstructed the time series using the tidal analysis amplitudes and phases, the residual current time series was obtained by subtracting one from the other. What is contained within the residual current represents forcing from tidal frequencies not used in the harmonic analysis, a wind-driven current element, other surface processes, and non-linear interactions.

The mean residual current amplitudes are found to be 10 cm/s or less and table 6.3 shows that the radar and ADCP residuals are moderately correlated. Using a constant ADCP bin height above the sea bed gave very good amplitude and phase agreement with radar measurements. This is not generally the case when comparing residuals and in table 6.3 we see improved correlations when using a bin height at a constant distance below the surface. Results are particularly improved for the v component. When the ADCP A time series is switched so that it is always the measurement bin at 2 m below the surface the correlation improves from 0.18, for 18 m above the bed, to 0.45. Improvements are also seen in the u component but the differences are not as great. These further improved using a bin height 3 m below the surface as opposed to 2 m. The improvement is greatest for ADCP B going from a correlation of 0.39 to 0.53. This is discussed further in chapter 7.

Mooring and Measurement details	r		rmsd cm/s	
	u	v	u	v
ADCP A$_{ab18}$ R234	0.38	0.18	12.4	12.2
ADCP A$_{bs2}$ R234	0.42	0.45	10.2	10
ADCP A$_{bs3}$ R234	0.48	0.42	12.2	11.8
ADCP B$_{ab20}$ R136	0.61	0.40	13.0	10.3
ADCP B$_{bs2}$ R136	0.39	0.47	12.3	7.6
ADCP A$_{bs3}$ R136	0.53	0.47	12.1	9.1

Table 6.3: Correlation (r) and root mean square difference (rmsd) of ADCP and radar residual currents after tidal analysis. East (u) and north (v) components from radar cell 234 are compared with ADCP A and cell 136 with ADCP B. Subscript numbers represent the height above the bed (ab) or below the surface (bs).

Ebuchi *et al.* [2006] took an alternative approach to defining the residual current where the ADCP current amplitudes are subtracted from those of the radar. Ebuchi *et al.* [2006] considers the HF radar to average currents from the surface to a particular depth, 1 m in the case of Liverpool Bay, and the ADCP to average tidal currents at varying depths below the ocean surface. With this definition Ebuchi *et al.* [2006] found weak to moderate positive correlation between the u and v residual current components and wind measurements of 0.26 for u and 0.4 for v.

Wind forcing on surface currents was investigated by comparing the residual current time series with the wind velocity measurements taken on Hilbre Island. The original current time series data minus that reconstructed from tidal analysis and the Ebuchi *et al.* [2006] residual time series are both considered. The results, see table 6.4, give a measure of how the effect of wind forcing is captured by the HF radar and ADCP.

The ADCP B residual u and v current components have low correlations with wind data of speeds 0 m/s or more. This is also true for ADCP A u components with a slightly increased, but still low, v correlation. The radar data with moderate correlations (around 0.4) is therefore better capturing wind-driven currents.

Stronger winds are indicative of higher sea state conditions and will have more of a forcing effect on the sea surface. To investigate these effects a high-pass filter

Residual current time series	Wind speeds 0 m/s +		Wind speeds 12 m/s +	
	u	v	u	v
Radar Cell 136	0.38	0.44	0.47	0.77
Radar Cell 234	0.36	0.42	0.48	0.72
ADCP A_{bs2}	0.07	0.33	0.01	0.30
ADCP A_{bs3}	0.02	0.26	0.037	0.25
ADCP A_{ab18}	0.04	0.25	0.06	0.26
ADCP B_{bs2}	0.16	0.15	0.19	0.19
ADCP B_{bs3}	0.12	0.09	0.09	0.079
ADCP B_{ab20}	0.15	0.15	0.10	0.18
Radar 234 − ADCP A_{ab18}	0.39	0.29	0.47	0.57
Radar 136 − ADCP B_{ab20}	0.22	0.22	0.32	0.48

Table 6.4: Correlation of ADCP and Radar residual east (u) and north (v) current components with wind data from the Hilbre Island meteorological station. Subscript numbers represent the height above the bed (ab) or below the surface (bs).

was applied to select winds > 12.3 m/s (roughly 12% of data), categorised as a strong breeze. It can be seen from figure 6.4 that the majority (about 80%) of winds > 12 m/s are moving north-eastwards. This is consistent with the majority of storm events in the UK coming from the west.

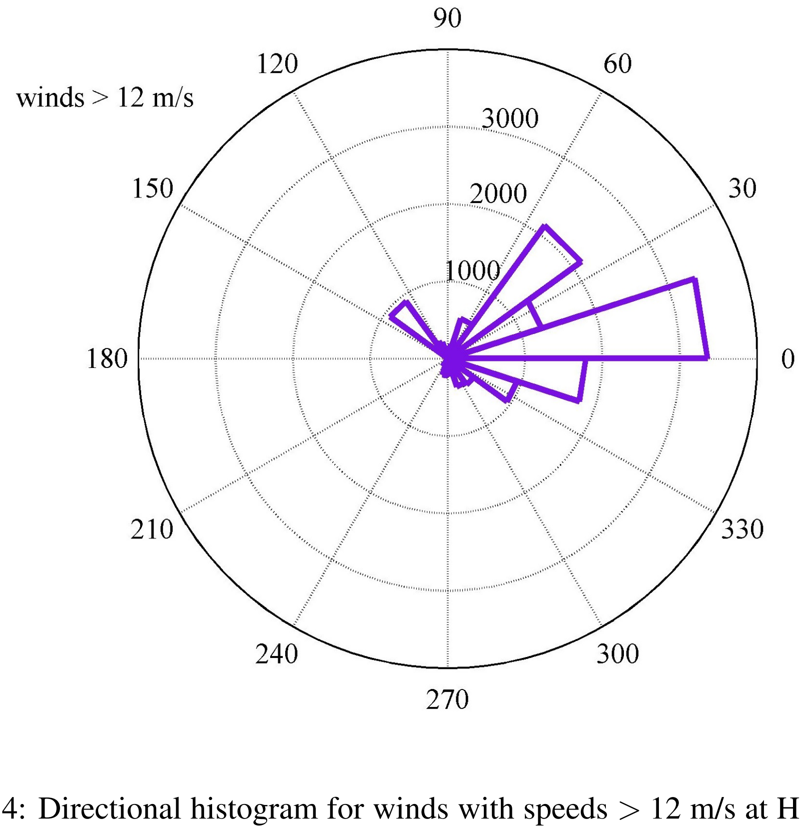

Figure 6.4: Directional histogram for winds with speeds > 12 m/s at Hilbre Island Meteorological Station. Angles are the directions the wind is going to with winds blowing towards the east at 0^o, the North at 90^o, etc. Data plotted covers the two year time series from January 2006 to December 2007.

Looking at the data in table 6.4, the radar residual u component showed improved, moderate, positive correlation after the high wind-speed filter was applied. The residual v component is however greatly improved from a correlation of 0.44 to 0.77 ± 0.02 at radar cell 136. This is also the case at cell 234 where the correlation is 0.42 before filtering and 0.72 ± 0.02 afterwards. The influence of the wind on the v component is much more obvious because of the smaller tidal influence. This is evident in the fact that it has a higher correlation with the wind data than the residual u component both before and after filtering. Therefore wind-driven surface currents will be a significant part of the residual radar current amplitude.

Correlations are slightly improved between wind data and ADCP residuals at 2 m below the surface when filtering, but remain low. At a constant bin height and at 3 m below the surface there is no improvement. It is most likely that wind effects are not propagating deep enough for the ADCP closest surface bin to be distinguishable above noise level. It is therefore the radar, which directly observes the ocean surface, which is best suited to observe surface wind effects.

Using the residual current time series, as defined by Ebuchi *et al.* [2006], has comparable results for the u component. The correlations for v, 0.57 with ADCP A and 0.48 with ADCP B, are however much lower. Surface effects in Liverpool Bay are therefore best captured using the original radar current time series minus the reconstructed time series through tidal analysis and not the method of Ebuchi *et al.* [2006]. This is clear as the radar residual data had a significant positive correlation with wind data when there are winds of 12.3 m/s or more.

Chapter 7

Current measurements at the North Hoyle wind farm

7.1 Introduction

This chapter looks in detail at HF radar data statistics from measurement cells co-located with the North Hoyle wind farm (NHWF). Current measurements from the radar are compared with those from nearby ADCPs using a two year time series from January 2006 to December 2007.

First discussed is the expected level of agreement between Radar and ADCP radial currents and the dual radar vector measurements at locations in the radar footprint other than the NHWF. This is then compared to the agreement with ADCPs at NHWF. Also investigated is the expected agreement as a function of distance from the ADCP and cross-over angle.

The ADCP configuration in Liverpool Bay has a theoretical accuracy for determining currents of 0.7 cm/s. Due to the sampling frequency the theoretical accuracy of each radial current measured by the Liverpool Bay WERA radar is 9 cm/s, significantly larger than the ADCP. This however is improved by finding the peak of a quadratic fitted to the logged values of the Doppler spectra around the first-order peak.

Outliers occur in both current time series but are more prevalent in the HF radar measurements. Physically unrealistic current speeds for Liverpool Bay were removed from both the HF radar and ADCP time series before comparison by applying a threshold of 4 times the average current speed. The threshold value was required to filter out spikes of obvious instrument error in the data and not intended to filter measurement noise or mask real measurement differences between the ADCP and HF radar. The current time series from both the ADCP and HF radar were inspected and this threshold was found to include over 99 % of the time series data in all data sets with only very large spikes being removed. The information, results, figures and tables discussed in this chapter have previously been presented by Robinson *et al.* [2011].

7.2 Radial HF radar and ADCP current agreement

Radial currents from several radar cells were compared with ADCP currents in the radar measurement direction 18 m above the bed at ADCP A (ADCP A_{ab18}) and at 20 m above the bed at ADCP B (ADCP B_{ab20}), a selection of which is given in table 7.1. All correlations were calculated at the 95% significant level, or greater, and found to have a confidence interval of ± 0.01 or better.

Mooring and Measurement details	r	rmsd cm/s	Mean current speed cm/s	
			Radar	ADCP
ADCP A_{ab18} R234 Ldl	0.87	10	17	17
ADCP B_{ab20} R136 Ldl	0.82	11	15	16
ADCP A_{ab18} R234 Fby	0.96	13	37	37
ADCP B_{ab20} R136 Fby	0.96	13.8	39	36
ADCP A_{ab18} R198 Fby(wf)	0.87	17.2	29	29
ADCP A_{ab18} R217 Fby(wf)	0.89	16.3	29	30
ADCP B_{ab20} R198 Fby(wf)	0.91	14.1	29	29
ADCP B_{ab20} R217 Fby(wf)	0.93	16.8	37	39

Table 7.1: Correlation (r), root mean square difference (rmsd) and means of ADCP and Radar (R) radial currents from both Llanddulas (Ldl) and Formby (Fby). Subscript numbers represent the height above the bed (ab) and cells co-located with the wind farm by wf.

Formby radial measurements have correlations of 0.96 ± 0.002 at the 99 % confidence limit with both ADCP A_{ab18} and ADCP B_{ab20}. The Llanddulas current radial correlations with ADCP A, 0.87 ± 0.004, and ADCP B, 0.82 ± 0.005, at the 99% confidence limit are lower than for Formby but the results still exceed those found in many other investigations.

Previous HF radar and ADCP correlations, including Fernandez & Paduan [1996], using a 25 MHz OSCR radar, and those of Emery *et al.* [2004] and Paduan *et al.* [2006], both of whom used a 13 MHz CODAR radar, had correlations ranging between 0.5 and 0.72, see table 1 in appendix A. Previous studies however use ADCP data from between 9 m and 20 m below the ocean surface. These are below the measurement averaging depth of the HF radars at any of these frequencies. The

ADCP time series will therefore not contain surface current information captured by the radar and correlations are subsequently lower.

Figure 7.1 shows HF radar cell 136 radial currents from a) Formby and b) Llanddulas against ADCP B_{ab20}. The component of the current in the direction of Llanddulas is clearly seen to be smaller in magnitude than that of Formby, with an average current magnitude of almost half, see table 7.1. The Llanddulas HF radar and the ADCPs rms difference is 10 cm/s and 11 cm/s at ADCP A_{ab18} and B_{ab20} respectively. This increases to 13 cm/s with ADCP A_{ab18} and 13.8 cm/s with ADCP B_{ab20} with Formby. These rms differences fall mid-range of those previously reported however are proportionally smaller compared with their mean current magnitudes.

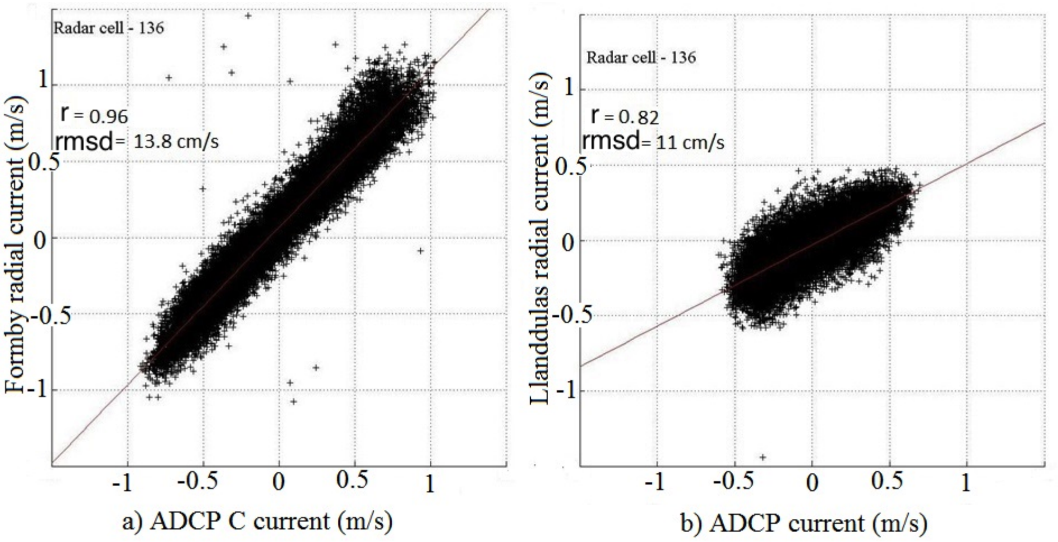

Figure 7.1: The a) Formby and b) Llanddulas radial current, cell 136, against the ADCP B current component in their look direction.

Table 7.1 also gives the correlations for ADCPs A and B with the Formby HF radar radials at cells 198 and 217. These cells are co-located with the NHWF. ADCP B is closer to the wind farm. It has better agreement than ADCP A for these cells with higher correlations of 0.91 and 0.93 and smaller rms differences of 14.1 cm/s and 16.8 cm/s at cells 198 and 217, respectively. The correlations at the wind farm are less than at the ADCP locations but they are still very high and exceed those of previous studies. The rms differences are however notably larger, suggesting greater disagreement between the measurements at these locations.

7.3 Dual HF radar and ADCP current agreement

The comparison of the u (east) and v (north) current components between radar cell 136 and ADCP B_{ab20} is shown in figure 7.2 a) and b) respectively. Figure 7.2 follows figure 7.1 and again demonstrates the domination of the east-west currents in Liverpool Bay. The north-south component has a mean magnitude of roughly 25% that of the east-west current, see table 7.2.

Correlations of the u component between the radar and ADCPs are, as for radial currents, higher than found in previous studies. Correlations are 0.97 ± 0.001 with the ADCP-A_{ab18}8 and 0.98 ± 0.001 with B_{ab20}, both at the 99% confidence limit. The correlations for the v component are 0.58 ± 0.01 and 0.57 ± 0.01, again at the 99% confidence limit, for A_{ab18} and B_{ab20} respectively. These are significantly less than for the u component but compare well with the correlation of 0.58 for the non-dominant current component between the radar-ADCP study by Paduan & Graber [1997]. The rms differences are reasonable compared to radar-ADCP comparisons overall but are towards the large end of the rms difference range of 6.2 – 13.3 cm/s found in other studies for component currents [Fernandez & Paduan, 1996; Paduan & Rosenfeld, 1996; Teague *et al.*, 2001] (see appendix A, table 1).

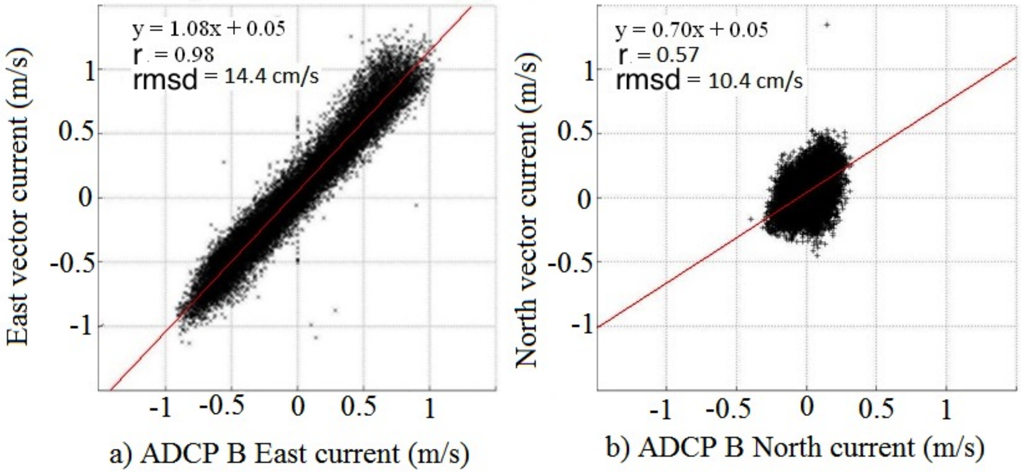

Figure 7.2: The HF radar vector current, cell 136, against the ADCP B current a) east and b) north components.

ADCP measurements at 2 m and 3 m below the surface were also compared as u and v components with the radar, see table 7.2. ADCP currents 2 m below the surface had an rms difference larger than those at a constant bin height by an average of 2 cm/s, however using ADCP currents at 3 m below the surface, did as expected from chapter 6, improve the rms difference by an average 1 cm/s. This may indicate that the ADCP current is noisier at 2 m below the surface possibly due to sidelobe contamination from the surface. This is supported by the fact that at ADCP B the rms difference at 2 m below the surface was 4 cm/s larger than at 3 m for the u component.

Mooring and measurement details	r		rmsd cm/s		Mean current speed cm/s			
	u	v	u	v	u		v	
					Radar	ADCP	Radar	ADCP
ADCP A$_{ab18}$ R234	0.97	0.58	13.3	11.8	37.7	37.6	11.2	8.1
ADCP A$_{bs2}$ R234	0.95	0.70	14.5	9.7		36.9		9
ADCP A$_{bs3}$ R234	0.96	0.61	12.6	10.6		38.7		8.7
ADCP B$_{ab20}$ R136	0.98	0.57	14.3	10.4	41.6	39.5	10.3	11
ADCP B$_{bs2}$ R136	0.94	0.72	16.9	7.3		38.2		11.7
ADCP B$_{bs3}$ R136	0.97	0.71	12.3	8.4		40.2		11.5
ADCP A$_{ab18}$ R198 (wf)	0.82	0.28	30.3	26.8	42.5		15.9	
ADCP A$_{ab18}$ R217 (wf)	0.83	0.27	30	29	42.9		18.9	
ADCP B$_{ab20}$ R198 (wf)	0.88	0.40	26.2	26.5				
ADCP B$_{ab20}$ R217 (wf)	0.89	0.40	25.7	29.1				

Table 7.2: Correlation (r), root mean square difference (rmsd) and means of ADCP and Radar (R) east (u) and north (v) current components. Subscript numbers represent the height above the bed (ab)or below the surface (bs) and cells co-located with the wind farm by wf.

Treating the u and v currents as real and imaginary components of a complex number the Pearson product-moment correlation coefficient between the radar and ADCPs were calculated using a circular correlation function. Current vectors from radar cell 234 and ADCP A$_{ab18}$ have a correlation of magnitude 0.93 and argument 2.4^o, see table 7.3. These results are very similar to the complex correlation of magnitude 0.94 and argument 1.5^o found by Howarth *et al.* [2007] when comparing the same measurement system for a one year time series in 2006. The same was also found for the comparison between radar cell 136 and the ADCP B$_{ab20}$.

At both locations the ADCP and radar correlation is high and the current directions agree well within the order of the azimuthal resolution of the radar. The rms differences are again towards the larger end of the range compared to previous studies but are proportionally similar to the mean current.

Complex correlation magnitudes between the radar and ADCP were found by Howarth *et al.* [2007] to be less for the bin 3 m above the bed than at the 18 m and 20 m bins. This was also the case for the two year extended time series. The mean current magnitudes at the bed were found to be approximately 25 % less, possibly due to shearing forces, density variation, and bed friction. The complex correlation magnitudes between the bed and the surface calculated by Howarth *et al.* [2007] for ADCP A_{ab3} of 0.93 and 0.92 for ADCP B_{ab3} compare well to the values found for the two year current comparison of 0.83 and 0.89 for ADCP A_{ab3} and ADCP B_{ab3} respectively, see table 7.3. The directional agreement is also reasonable, within 10^o of each other, given the different ADCP deployments, and is again close to the directional resolution of the radar. The high agreement between the ADCP bed level currents and the radar is another indication of how dominant the tidal forcing is within this region.

Mooring and Measurement details	r (phase)	rmsd cm/s	Mean current speed cm/s	
			Radar	ADCP
ADCP A_{ab18} R234	0.93(2.4)	14.3		39
ADCP A_{ab3} R234	0.83(9.67)	21	41.0	28.4
ADCP A_{bs2} R234	0.93(0.05)	13.9		39.1
ADCP A_{bs3} R234	0.93(0.05)	13.7		40.6
ADCP B_{ab20} R136	0.94(2.7)	14.6		42
ADCP B_{ab3} R136	0.89(2.43)	22	44.1	30
ADCP B_{bs2} R136	0.92(0.06)	15.8		41.2
ADCP B_{bs3} R136	0.95(0.07)	12.3		42.9

Table 7.3: Correlation (r), root mean square difference (rmsd) and means of ADCP and Radar (R) complex current measurements with phase in degrees (degrees). Subscript numbers represent the height above the bed (ab) or below surface (bs).

As done for tidal analysis in chapter 6, the advantages of below surface time series compared to those at a constant height above the sea bed are established for vector currents. Comparing the radar and ADCP A currents at 2 m and 3 m below surface shows exactly the same high correlations, see table 7.3, as for the constant ADCP A_{ab18} bin currents and rms differences within 0.6 cm/s of each other. The ADCP A 3 m below surface currents show a slight improvement in rms difference than those at 2 m but it is small and overall the currents appear will mixed at this location, as was the case when comparing u and v components at 2 and 3 m below the surface. This is also seen at ADCP B but in this instance the better agreement between the radar and ADCP currents at 3 m below the surface is more significant. There is a noticeable decrease in the rms difference using ADCP currents 3 m below the surface at ADCP B and better agreement of the radar and ADCP mean magnitude and direction for both ADCP A and B.

The correlations between all radar cells and ADCP A as a function of distance are shown on figure 7.3. The east component correlations on figure 7.3 a) are seen to be very high at even the furthest distances from the ADCP. Some outliers can be seen between 10 km and 30 km and the correlation values at the NHWF are amongst these. The north components on figure 7.3 b) are seen to be much more variable. There is a general trend of correlations getting lower as distance increases and the NHWF correlations fall mid range for their distance.

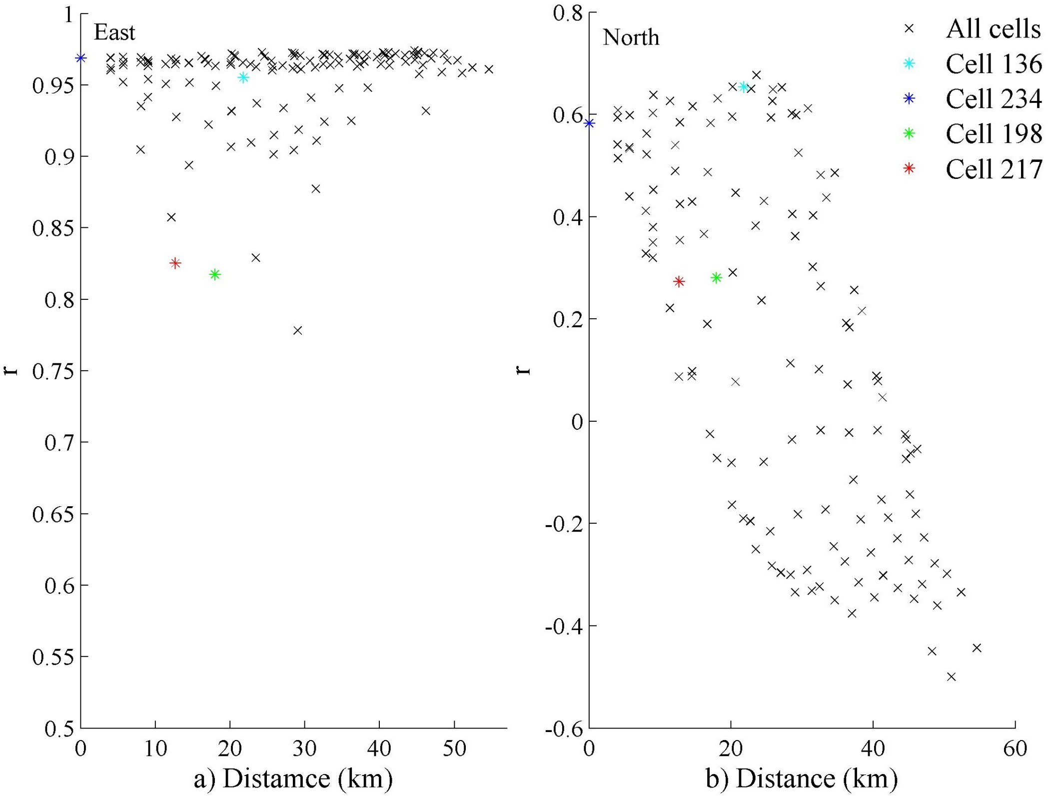

Figure 7.3: Radar a) East and b) North correlations with ADCP A against distance. NHWF co-located cells are 198 and 217. ADCP A is located at cell 234.

The rms difference for the east, figure 7.4 (a), and north, figure 7.4 (b), current components increases with distance from the ADCP. At the NHWF, cells 198 and 217, the rms difference is over double the average for that distance. Other outliers are also present on figure 7.4 and, like those on figure 7.3, they are not co-located with the wind farm. As such the wind farm is not thought to be the main cause of the outliers in these cases.

When current measurements from Formby and Llanddulas are combined for a resultant vector the angle between the radials is defined as the cross-over angle, β. β, and the current alignment relative to the radial, α, introduce an error magnification that will be less than 1.5 for $\beta < 1.3\alpha$ and less than 4 when $\beta > 30^o$ [Prandle,

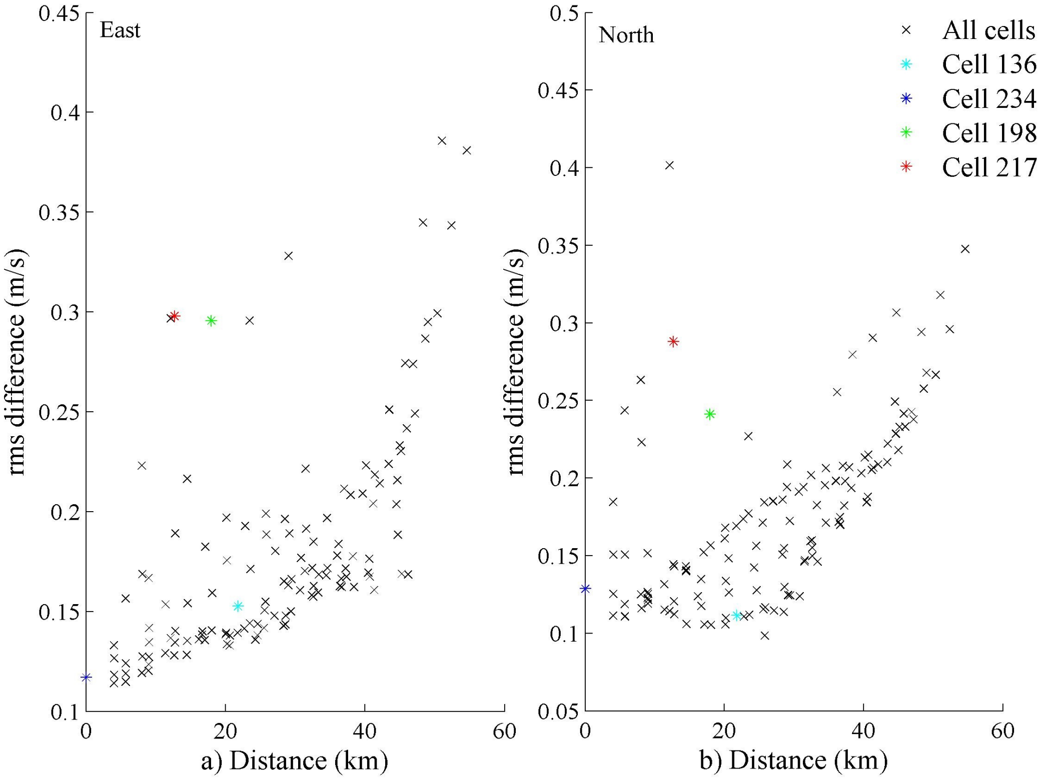

Figure 7.4: Radar a) East and b) North rms differences with ADCP A against distance. NHWF co-located cells are 198 and 217. ADCP A is located at cell 234.

1991]. The angle between two radials is generally required to be $> 30^o$ and $< 150^o$ when resolving for the current vector [Paduan & Graber, 1997]. The amplification factor is greatest where the difference in look angle approaches 180^o, however in Liverpool Bay at the NHWF this region is outside the required 60^o region from the boresight of the radar, where sidelobe contamination is prevalent and dual currents and waves are not resolved.

Figure 7.5 a) and b) shows how the correlation between the radar and ADCP varies with cross-over angle for the east and north currents, respectively. For the majority of cells on figure 7.5 a) correlations are excellent compared with previous studies and most outliers occur for angles greater than 150^o as expected [Paduan & Graber, 1997]. The NHWF co-located cells follow the trend of how correlations vary at large cross-over angles for both the east and north currents.

Figure 7.6 shows how the rms difference between the radar and ADCP varies with cross-over angle. Both figure 7.6 a) and b) for the east and north currents show a distinctive ”U” shape due to increased errors at large and small cross-over angles. Cells 198 and 217 have large rms differences but, as was the case for their

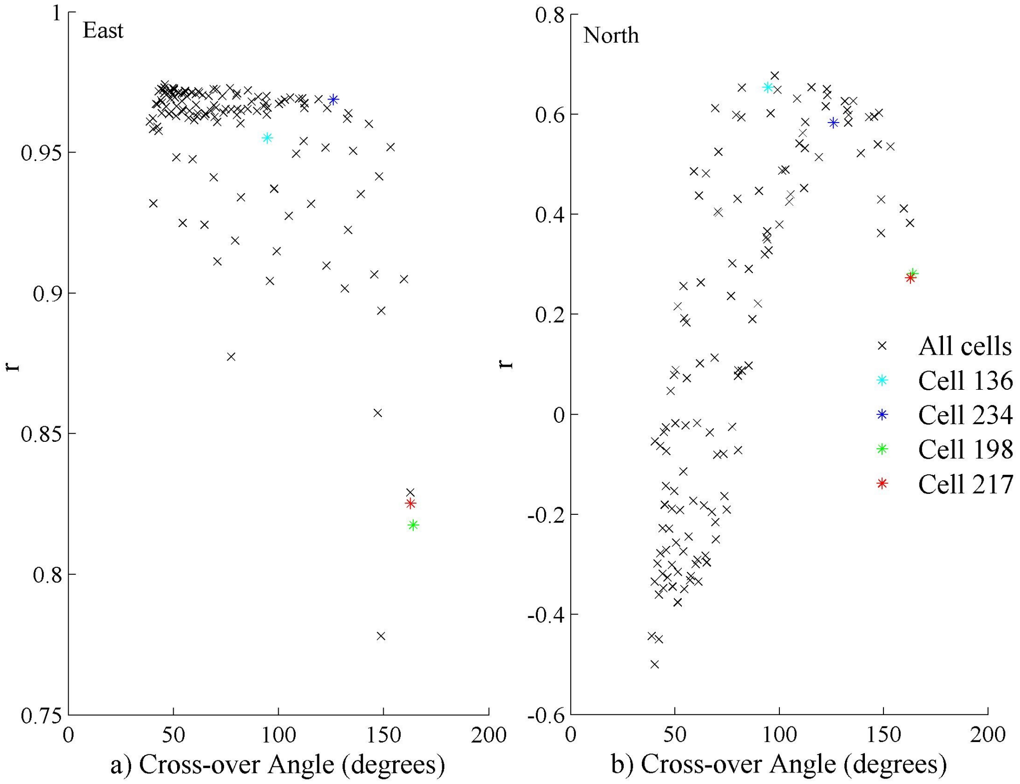

a) Cross-over Angle (degrees) b) Cross-over Angle (degrees)

Figure 7.5: Radar a) East and b) North correlation with ADCP A against cross-over angle. NHWF co-located cells are 198 and 217. ADCP A is located at cell 234.

correlations, these follow the overall trend and are consistent for the cross-over angle at these locations, 164^o and 163^o for cells 198 and 217 respectively. This shows the cross-over angle to be a contributing factor to measurement differences at the wind farm location.

Chapman & Graber [1997] showed these geometric errors can be estimated by using the HF radar radial current measurements and the component of the ADCP current in the direction of the radial being considered [Prandle, 1991]. This eliminates cross-over as it is a single radar measurement. An estimate for the magnitude of the cross-over angle error can be obtained by taking the difference between the rms difference of the ADCP and radar radial current and the rms difference between the ADCP and the dual current vector.

The radar dual current vectors and radial current difference have been used to estimate the magnitude of the cross-over angle error as set out by Chapman & Graber [1997]. The cross-over angle at the NHWF is therefore estimated to introduce errors in the current amplitudes of roughly 15 cm/s. For cells within the recommended range this is much less, roughly 3 cm/s.

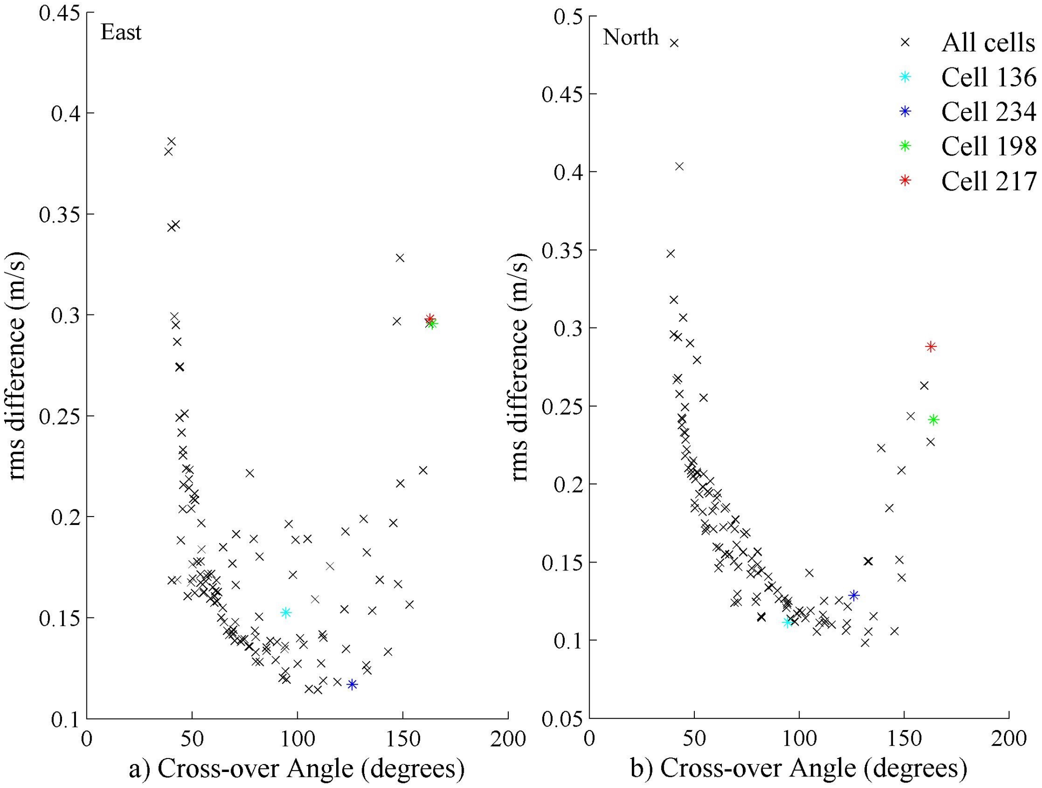

Figure 7.6: Radar a) East and b) North rms differences with ADCP A against cross-over angle. NHWF co-located cells are 198 and 217. ADCP A is located at cell 234.

7.4 Summary

The continuous two year time series of data is one of the longest HF radar current records examined to date. Measurements are made in a wide variety of environmental conditions and not all of these are favourable to HF radar measurement. A comparison of such long duration provides working expectations of the Liverpool Bay HF radar for average seasonal conditions. HF radar current measurements in Liverpool Bay are provided consistently over this period and the correlations between the ADCP and radar are greater than previously reported, > 0.9.

North-south currents in Liverpool Bay are on average 65% smaller than east-west currents which are tidally dominated by the M_2 tidal frequency [Robinson *et al.*, 2011]. Due to tidal dominance in the east-west direction the radar and ADCP currents are highly correlated and surface currents, as well as those throughout the water column, are fairly uniform.

The results show excellent agreement with results from Howarth *et al.* [2007] at ADCP A_{ab18} and B_{ab20}. Agreement between currents 3 m above the bed is slightly less than found by Howarth *et al.* [2007] but still has a large positive correlation, > 0.83. The rms differences were very similar between both radar-ADCP comparisons for magnitude and direction and are comparable to the differences found in other studies, although the rms differences are at the large end of the range.

The ADCP averages through the water column in 1 m bins, the centre of which is a varying height above the bed depending on the deployment. This results in the 2 m below surface current time series including backscatter in the averaging from between 1.5 and 2.5 m below the surface and may introduce some sidelobe contamination from reflections off the surface. The 3 m below surface current time series does not have this issue as backscatter is from between 2.5 m and 3.5 m below the surface. This is evident in the greater correlations and smaller rms differences. The low Hs in Liverpool Bay will however limit how far down the wind driven surface currents are mixed in the water column and the closer the ADCP bin to the surface the better. The 2 m below surface time series is likely to be a good compromise between some surface sidelobe contamination and observing the surface current. The advantage in using either the 2 m or 3 m ADCP surface time series as opposed to ADCP measurements at a constant bin height is however evident, particularly for comparing north components. This is also seen when treating currents in terms of magnitude and direction and further highlights differences between using an ADCP current at a constant bin height compared with one at a constant depth.

The wind farm region has consistently yielded lower correlations and larger rms differences between the radar and ADCP current measurement. After consideration this is thought to be a combination of degradation due to the large cross-over angle, β, and distance from the ADCPs location and not the wind farm itself. Comparing the radial and dual current results, the cross-over angle at the wind farm location is thought to introduce errors in the current amplitudes of roughly 15 cm/s, and roughly 3 cm/s in regions where the cross-over angle is within the required range.

Overall the HF WERA radar in Liverpool Bay has been shown to provide almost continuous current measurements over a significant period of time. Current magnitudes and directions have considerable accuracy over an extensive region compared to current measurements made by ADCP. The correlation between ADCP and HF radar current measurements is very high and rms differences are relatively small.

Chapter 8

Current and wave measurement at the Rhyl Flats wind farm

8.1 Introduction

The North Hoyle wind farm (NHWF) has been operational since before the HF radar installation therefore a before and after study on HF radar current and wave measurements is not possible. Cross-over angles at the NHWF are also slightly larger than the 60^o norm and are suspected to mask any effect on current measurement from the wind farm [Robinson *et al.*, 2011]. At Burbo Bank wind farm (BBWF), shallow mud flats and bad cross-over angles mean the region is also outside the operational parameters of the HF radar and current and wave measurements are not possible. The Rhyl Flats Wind Farm (RFWF) therefore presents the best opportunity to gain an understanding of the radar's performance and measurement accuracy before and after the installation of a wind turbine.

This chapter reports on the comparison of HF radar current and wave measurements with those of fixed moorings for periods before and after the RFWF installation. HF radar cells co-located with the RFWF are cells 138 and 158 and these are the focus of the measurement comparison.

The three month period of February, March and April 2009 is defined as before the RFWF installation. At this time the wind farm towers are in place but introduce only a large stationary return in the Doppler Spectrum which does not affect current and wave measurements. Turbine blade attachment, the rotation of which is thought to be the significant contribution to characteristics of the Doppler Spectra, as seen in Figure 8.1, began at the end of April 2009 and first power was exported in July 2009. February, March and April of 2010 is the period defined as after the installation and at this point RFWF is fully operational. Sea states are generally low for both these periods and HF radar is known not to be as accurate in low sea states however it is during these conditions where the influence of the wind turbines is suspected to be most prevalent. The information, results, figures and tables discussed in this chapter have previously been presented by Robinson *et al.* [2013].

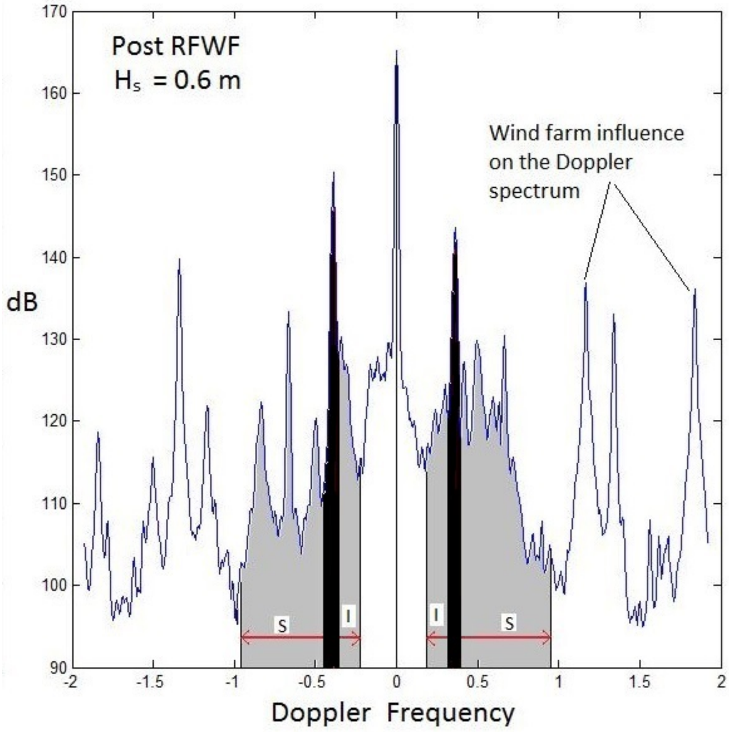

Figure 8.1: An arbitrary Doppler spectrum with amplitudes in decibels (dB) showing wind turbine interference. The first-order spectral region is shaded black, the second-order grey. The inferior, I, and superior, S, region of the second-order Doppler spectrum are also indicated.

The average noise for each radar cell from the Llanddulas Doppler spectra during the before and after periods considered are shown in figure 8.2. Pre RFWF, figure 8.2 a, the main regions of peak noise are the North Hoyle wind farm and the measurement cells directly in front of the Llanddulas radar, where internal noise from the transmitter is prevalent. Post RFWF, figure 8.2 b, the noise level at North Hoyle, roughly 96 dB, and the base level, around 90 dB, is relatively unaltered in comparison to the previous year, as it is with the majority of cells, however it is obvious this is not the case for cells co-located with RFWF. Mean noise levels are greatest at cell 158 (106 dB) and an increase in mean noise appears evident in measurement cells up to 8 km, or 2 measurement cells, away from the RFWF.

As discussed in chapter 5, the introduction of the NHWF greatly increases the

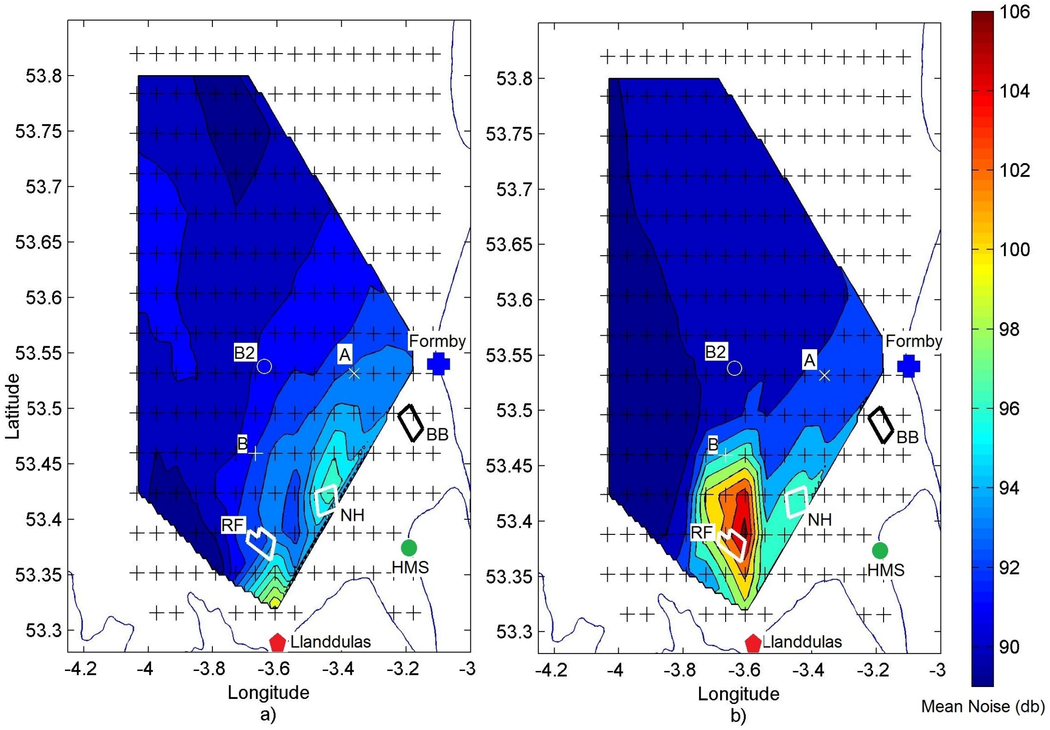

Figure 8.2: Average Llanddulas Doppler spectra noise a) before and b) after the Rhyl Flats wind farm installation.

noise of the region but does not affect the current measurement availability, which was a minimum of 93% of the before and after time periods. Wave data availability was however highly variable over the entire radar footprint as expected, ranging from 3% to 93%, an effect due more to the low sea states during this time.

8.2 HF WERA radar and ADCP current comparison

An ADCP surface current time series consisting of measurements 2 m below the surface was used for the purpose of this comparison. This is common to reduce surface noise effects [Liu *et al.*, 2010; Robinson *et al.*, 2011] and is a compromise between minimising surface sidelobe contamination and capturing wind driven surface currents, as discussed in chapter 7. As the 2 m below surface bin has been used throughout this chapter the bs subscript used in chapter 7 has been omitted.

The 2009 data availability from ADCP A is on a par with that of the radar, being 95%, however this is much lower for ADCP B at only 46% due to a deployment and maintenance issue. In 2010 the ADCP data availability improved to 99.9% for both ADCPs however ADCP B was relocated in January 2010 from HF radar cell 136 and for the post RFWF measurement period is co-located with HF radar cell 134.

Due to the close proximity of ADCP A to cell 234, also the buoy location, and the added complications at ADCP B between the 2009 and 2010 measurement periods, only ADCP A has been used for the comparison with HF radar currents.

Measurement details	r 2009	r 2010	rmsd cm/s 2009	rmsd cm/s 2010	rmsd % of mean current 2009	rmsd % of mean current 2010
ADCP A R234 Ldl Radial current	0.83	0.84	10.7	13.9	67	84
ADCP A R157 Ldl Radial current	0.61	0.16	9.7	13	100	129
ADCP A R158 Ldl Radial current	0.56	0.07	8.5	11.5	119	155
ADCP A R159 Ldl Radial current	0.46	0.02	8.1	11.1	150	207
ADCP A R234 Fby Radial current	0.94	0.88	15.5	22.9	41	59
ADCP A R157 Fby Radial current	0.90	0.94	18.6	15.2	51	41
ADCP A R158 Fby Radial current	0.87	0.94	18.5	13.9	57	42
ADCP A R159 Fby Radial current	0.85	0.94	18.2	14.3	63	50

Table 8.1: HF radar radial (Ldl = Llanddulas and Fby = Formby) and ADCP current correlations for February, March, and April 2009 and 2010 at the buoy co-located HF radar cell, 234, and the Rhyl Flats Wind Farm co-located HF radar cells, 157, 158, and 159.

Comparing the radial current measurements in table 8.1 between HF radar and ADCP it is found that the Formby radar is most robust to wind turbine interference (WTI). Formby radial measurements have good correlations with ADCP A in both 2009 and 2010 at the RFWF and the co-located HF radar cell 234, as was found by Robinson *et al.* [2011]. By contrast the Llanddulas radial data shows a significant decrease in correlation with ADCP A at the RFWF location where, as at the co-located radar cell, it had improved slightly. The differences reflect the varying look directions of the two individual radars.

Figure 8.3 a) and b) show Doppler spectra for Formby and Llanddulas, respectively, for the case where a large difference between the ADCP and radar current measurement has occurred, shown as outliers on figure 8.4 d). Both spectra show contributions from the wind turbines that are of similar amplitude to current returns and are in close proximity to the Bragg scattering frequency. It is clear from figure 8.3 that the wind farm influence is much greater at Llanddulas with amplitudes remaining much higher and with broader peaks. It is no surprise then that the large discrepancies between ADCP and radar measurements are from the Llanddulas radar as this makes the first order Bragg peaks difficult to identify. The very low sea state, Hs equal to 0.4 m, will also be contributing to this effect.

The Doppler spectrum shown in figure 8.1 was taken in slightly improved conditions with better winds and a higher sea state, although it is still low with a Hs of 0.6 m compared to 0.4 m. Here the first order Doppler spectral peak is still easily identifiable and a reasonable current measurement can be made.

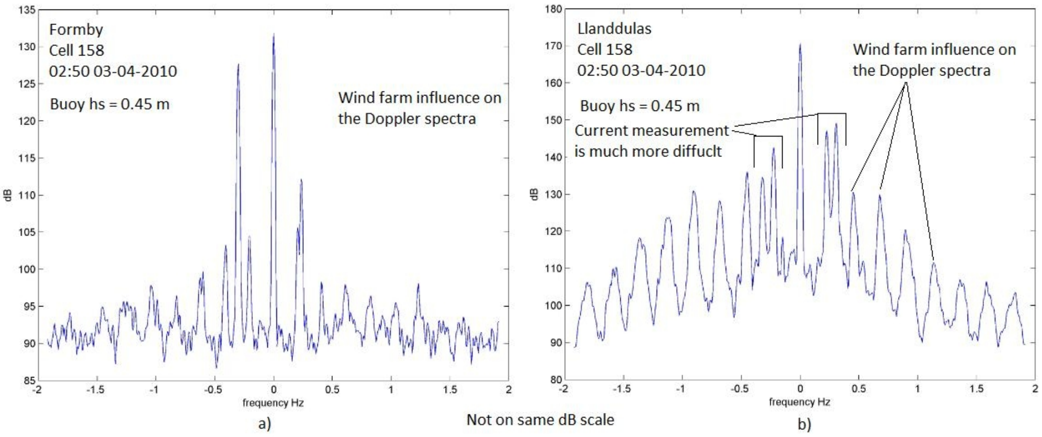

Figure 8.3: Radar cell 158 Doppler spectra produced by the a) Formby and b) Llanddulas radar at $02:50$ on $03-04-11$, post RFWF installation. It should be noted that the Formby and Llanddulas spectra are presented with different scales so the amplitude detail can be seen.

The north radar current component, known to show the same trends as the Llanddulas radar [Robinson *et al.*, 2011], is plotted against the north ADCP current component in figure 8.4 d). This shows large radar spikes occur on several occasions during the 3 month post RFWF period. Currents measured by the ADCP at this time are very small in magnitude, less than 1 cm/s, resulting in high radar current measurements for very low ADCP measurements. This is not evident in the pre RFWF data as seen in figure 8.4 b). HF radar data naturally has more data spikes. If the distinct line seen in figure 8.4 d) is due to the measurement method the spikes would be expected to occur over a much larger ADCP current range, as is seen in figure 8.4 a) and c), however this is not the case.

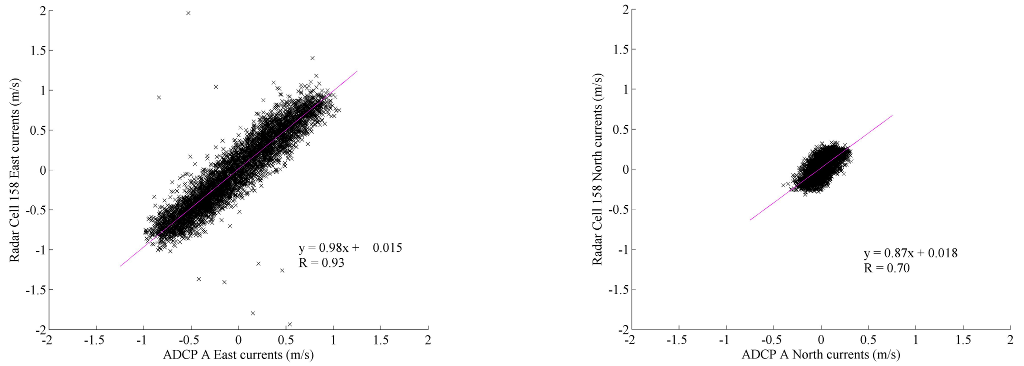

a) East currents pre Rhyl Flats wind farm b) North currents pre Rhyl Flats wind farm

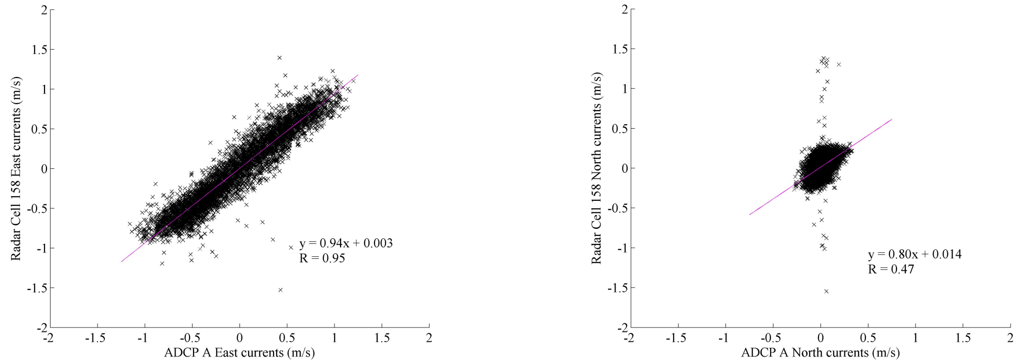

c) East currents post Rhyl Flats wind farm d) North currents post Rhyl Flats wind farm

Figure 8.4: HF radar east and north current measurement agreement with ADCP pre and post Rhyl Flats wind farm.

The high correlations of the Formby radials are most obvious in the dual current vector and any errors introduced from the Llanddulas radial are not evident. Correlations in 2009 and 2010 are high and consistent with those found by Howarth *et al.* [2007] and Robinson *et al.* [2011]. The north current correlations are less in 2010 compared with the previous year however not by a significant amount, see table 8.2.

8.3 HF radar and buoy wave comparison

Significant wave heights were similar during February, March, and April in 2009 and 2010 and were generally low as figures 8.5 a) and b) show. The majority of data gaps in 2009 occur when the buoy is measuring Hs values below the radar measurement threshold at this frequency. The HF radar data spikes result in large mean radar Hs values of 1.88 m in 2010 and 1.67 m 2009. In contrast the buoy mean Hs values were much lower at 0.72 m and 0.55 m, respectively.

The 2010 data series is more complete with a greater number of simultaneous

Measurement details	r 2009	r 2010	rmsd cm/s 2009	rmsd cm/s 2010
ADCP A R234 vector current	0.86	0.85	17.8	18.8
ADCP A R157 vector current	0.93	0.93	14.1	13.3
ADCP A R158 vector current	0.92	0.93	14.9	11
ADCP A R159 vector current	0.90	0.93	17.7	12.6
ADCP A R234 East current	0.89	0.88	21.1	22.6
ADCP A R157 East current	0.94	0.94	16.9	17
ADCP A R158 East current	0.93	0.95	17.1	15.8
ADCP A R159 East current	0.91	0.94	19.5	16.4
ADCP A R234 North current	0.53	0.49	13.9	15.7
ADCP A R157 North current	0.68	0.52	10.8	12.8
ADCP A R158 North current	0.51	0.43	9.3	12.9
ADCP A R159 North current	0.70	0.54	9.1	10.7

Table 8.2: HF radar vector, east, and north, current correlations (r) and root mean square differences (rmsd) with a bed mounted 600 kHz ADCP for data collected February, March, and April 2009 and 2010. Radar cells compared are cell, 234, and the Rhyl Flats Wind Farm co-located HF radar cells, 157, 158, and 159.

measurements available in 2010 compared with 2009. Their agreement is however less. Most of the increased data points occur at low Hs, as measured by the buoy, however for buoy measurements of less than 1 m there is no correlation (-0.17) with the HF radar measurements. During other HF radar experiments much better correlations for low sea state have been reported, for example Liu *et al.* [2010] found correlations up to 0.4 with a significance at the 95% confidence level. It appears that under the influence of the RFWF more erroneous data points are passing the quality control measures and not being filtered out. This results in an apparent increase in data availability from 2009 to 2010 however the overall agreement is much worse.

Figure 8.2 shows that the RFWF has caused an elevation in the noise level at cell 158. Many additional peaks, as seen on figure 8.3 b), are known to occur in the second-order region, shaded in grey on figure 8.1, which is the Doppler spectral region used for wave measurement. These additional peaks are providing at least some of the spurious wave measurements. The effect of the additional energy at these frequencies will lead to an increase in the measured wave energy and hence higher Hs measurements.

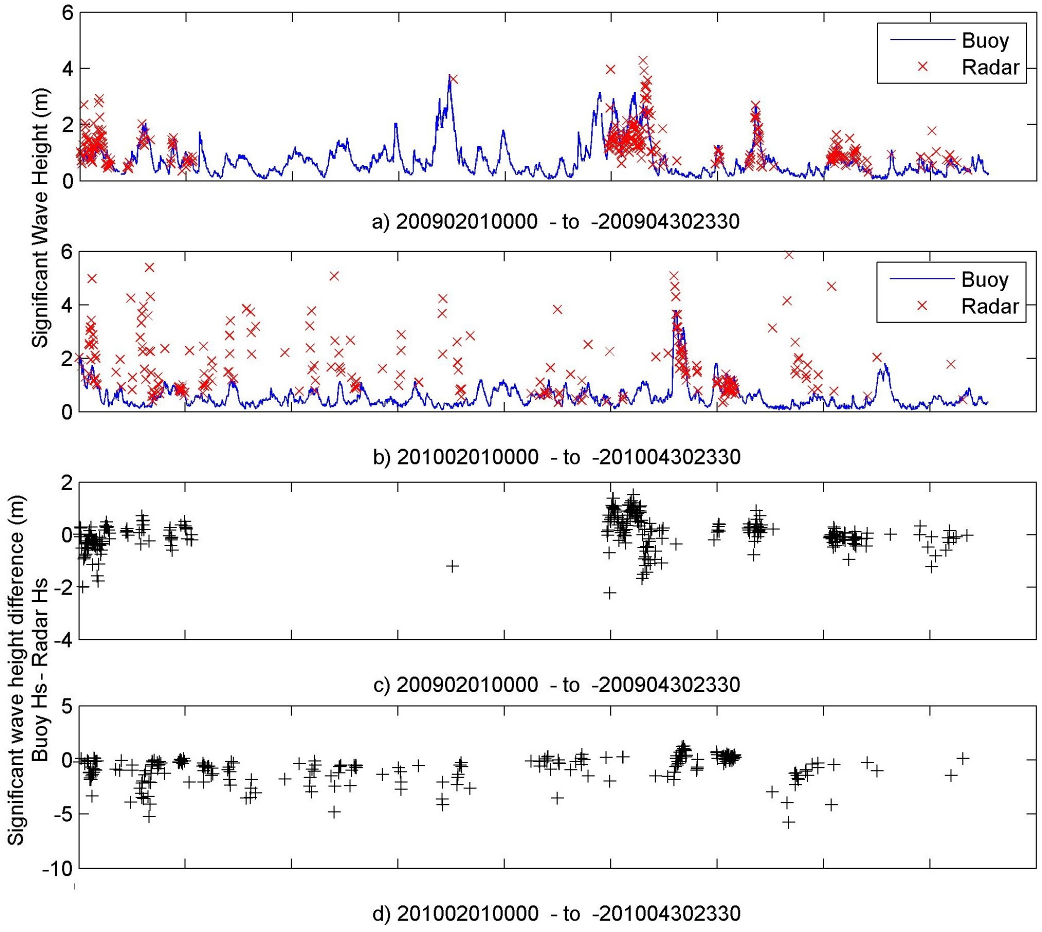

Figure 8.5: The simultaneous measurements of significant wave height by HF radar at cell 158 and Waverider buoy in 2009 and 2010 for the months of February, March, and April.

Measurement detail	r 2009	r 2010	rmsd (m) 2009	rmsd (m) 2010
Hs234 – Buoy	0.34	0.07	1.30	1.52
Hs157 – Buoy	0.64	0.49	0.63	0.95
Hs158 – Buoy	0.63	0.19	0.60	1.47
Hs159 – Buoy	0.45	−0.03	0.73	1.67
Hs – Buoy average over all cells	0.58	0.48		

Table 8.3: The correlation (r) of HF radar full inversion and Waverider Buoy significant wave heights (Hs) for February, March, and April 2009 and 2010 at the buoy co-located HF radar cell 234 and the Rhyl Flats Wind Farm co-located HF radar cells: 157, 158, and 159.

Table 8.3 shows results from the statistical comparison between HF radar and buoy Hs. No additional quality control measures have been applied and all available data have been used. There is seen to be an average decrease in correlation between radar and buoy Hs measurements from 2009 to 2010 of 0.1. These average correlation values of 0.58 in 2009 and 0.48 in 2010 are typical of the area and similar to those found by Howarth *et al.* [2007] and Wolf *et al.* [2007] of around 0.6. In contrast the decrease in agreement between radar and buoy Hs measurements from 2009 to 2010 at the RFWF is up to four and a half times greater than this with the rms difference more than doubling from 2009 to 2010, see table 8.3, at cell 158 and 159. The influence on cell 157 appears to be less significant with increases in rms difference and decreases in correlation more similar to those found overall.

To bring the quality control of the radar data more in line with that of the buoy, a maximum difference was imposed between consecutive measurements of 1 m, although potentially the wind farm will introduce anomalous results in consecutive radar measurements which would not be eliminated by this. There was a slight increase of $1.5-2\%$ of data spikes removed in the post RFWF data and this dropped off to less than 0.5% just outside the RFWF radar cells, indicating that the turbines were responsible for these errors. An additional data spike filter was also applied to account for physically unrealistic Hs measurements of 7 m or more.

Because of known inaccuracies of HF radar at low Hs at this radio frequency [Wyatt *et al.*, 2011], when the buoy Hs measurement was less than 1 m, the radar data and buoy measurements were removed from the comparison. After the 1 m high pass filter has been applied the data sets remaining are relatively small (47% of the originals at cells 158 and 234 in 2009 66% and 72% respectively in 2010) with most spikes in the radar Hs measurements occurring for low sea states.

Table 8.4 shows the correlation and rms difference between the radar and buoy Hs measurements after the additional quality control measures at the RFWF and buoy location. For the 2009 data the correlation of radar cells at the RFWF has decreased with the additional filtering. This is not the case for 2010 where the additional filtering has brought about improvements in the correlation between radar and buoy data. For cell 158 the additional data filtering increased the correlation in 2010 from 0.19 to 0.55 and at cell 159 it went from -0.03 to 0.81. There was also a large improvement for HF radar cell 234 where the Hs correlation with buoy data went from 0.07 in 2009 to 0.65 in 2010. HF radar cell 234 is known to have an increased ship presence. This could cause a spurious Hs measurement. If present for one time period the de-spiking methods used for this time series would remove the value, hence the improved correlation with buoy data.

Measurement detail	r 2009	r 2010	rmsd (m) 2009	rmsd (m) 2010
Hs234 – Buoy	0.69	0.65	0.69	0.61
Hs157 – Buoy	0.56	0.75	0.59	0.62
Hs158 – Buoy	0.38	0.55	0.73	0.90
Hs159 – Buoy	0.18	0.81	0.85	0.64
Hs – Buoy average over all cells	0.64	0.82	0.86	0.66

Table 8.4: The significant wave height (Hs) correlation, r, and root mean square difference (rmsd) of HF radar full inversion and Waverider Buoy for February, March, and April 2009 and 2010 at the buoy co-located HF radar cell, 234, and the Rhyl Flats Wind Farm co-located HF radar cells, 157, 158, and 159 after additional data filtering and quality control.

The additional filtering has had a large impact on improving the Hs correlations with buoy data over the entire radar footprint, both before and after the wind farm installation. Figure 8.6 shows the correlation between buoy and radar Hs measurements, after filtering for high sea states, for all cells where parameters allow for wave measurements. It is immediately evident comparing figures 8.6 a) and 8.6 b) that correlations between radar and buoy are higher in 2010 compared to 2009. This is also seen when comparing the data in tables 8.3 and 8.4 as the average correlation is seen to increase. This increase is a smaller amount in 2009, from 0.58 to 0.64, and much larger in 2010 from 0.48 to 0.82.

Viewing the correlation as a spatial plot over the radar footprint confirms what the data for cells at the RFWF suggests: the wind turbines are decreasing the measurement agreement between buoy and HF radar. Figure 8.6 a) shows that prior to the RFWF installation correlations between radar and buoy were expected to reflect the average over the radar footprint at the RFWF site. Figure 8.6 b) shows that after the RFWF installation below average measurements occur for cells at the RFWF location.

Another area highlighted by figure 8.6 b) is the region just below radar cell 234, where both the buoy and ADCP A are located. The correlation values are not however too dissimilar for the same cell in 2009 and likely to be caused by the region below radar cell 234 being particularly busy with shipping.

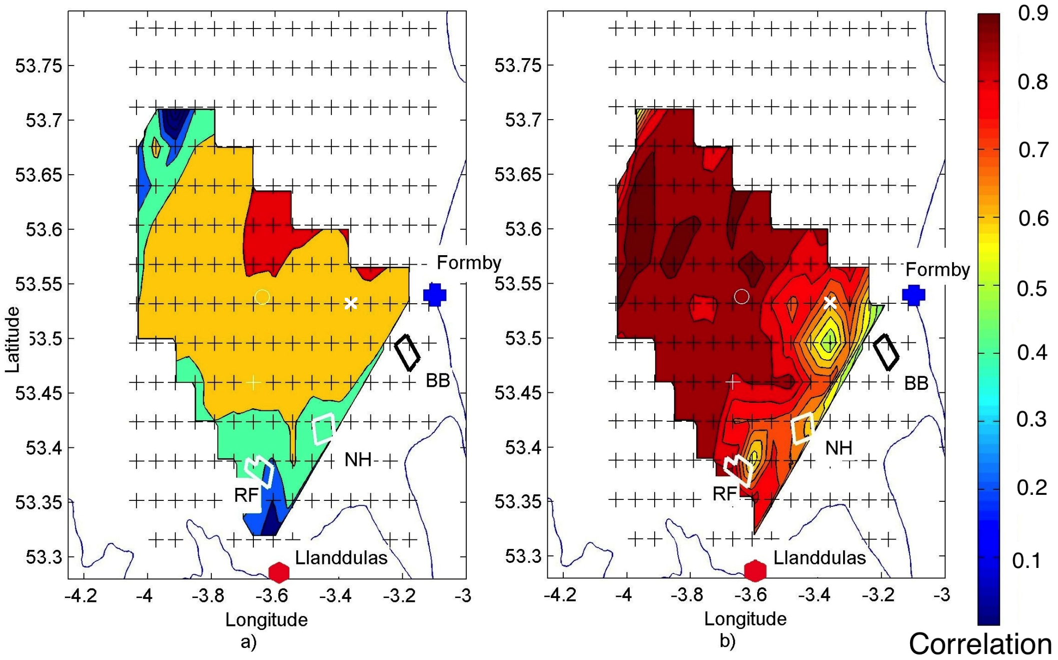

Figure 8.6: The HF radar and Waverider Buoy significant wave height correlation for the data period February, March, and April in a) 2009 and b) 2010 after the application of an additional filter process. The location of the North Hoyle (NH), Burbo Bank (BB), and Rhyl-Flats (RF) wind farms and location of ADCP A (x) are indicated.

Data spikes from ships passing slowly through the measurement cell could also appear in the measurements over more than one measurement period. If this were the case, they would not be removed by the additional data filtering. The effect of this is that no improvement between the HF radar and buoy data occurs and this region remains one of poor measurement quality.

The HF radar peak and mean periods, Tp and T1 respectively, of 2009 and 2010 were compared with those from the buoy after the additional filtering, see tables 8.5 and 8.6. The comparison shows there to be little Tp correlation for either the time period in 2009 or 2010 and moderate T1 correlation.

At the RFWF cell 158 the HF radar and buoy correlation is much less relative to the cells surrounding it in 2010 compared with 2009 for both Tp and T1. In 2009 Tp and T1 correlations and rms differences at the RFWF for radar cell 158 are close to the average over the radar footprint however in 2010 values at cell 158 are well below the averages for the data period used. What figure 8.6 and tables 8.4 and 8.6 indicate generally is that the radar performance at cells co-located with the RFWF will be poor compared to other radar cells.

Measurement detail	r 2009	r 2010	rmsd (m) 2009	rmsd (m) 2010
Tp234 – Buoy	0.05	0.12	3	2.5
Tp157 – Buoy	0.14	0.21	1.5	2.1
Tp158 – Buoy	0.26	0.03	1.9	4.4
Tp159 – Buoy	0.18	0.3	3.7	4.3
Tp – Buoy average over all cells	0.21	0.26	2.8	2.8

Table 8.5: The peak period (Tp) correlation, r, and root mean square difference (rmsd) of HF radar full inversion and Waverider Buoy for February, March, and April 2009 and 2010 at the buoy co-located HF radar cell, 234, and the Rhyl Flats Wind Farm co-located HF radar cells, 157, 158, and 159 after additional data filtering and quality control.

Measurement detail	r 2009	r 2010	rmsd (m) 2009	rmsd (m) 2010
T1234 – Buoy	0.25	0.46	1.6	1.7
T1157 – Buoy	0.49	0.52	1.1	1.5
T1158 – Buoy	0.46	0.19	1.3	2.4
T1159 – Buoy	0.32	0.45	1.9	2.1
T1 – Buoy average over all cells	0.4	0.5	1.6	1.6

Table 8.6: The mean period (T1) correlation, r, and root mean square difference (rmsd) of HF radar full inversion and Waverider Buoy for February, March, and April 2009 and 2010 at the buoy co-located HF radar cell, 234, and the Rhyl Flats Wind Farm co-located HF radar cells, 157, 158, and 159 after additional data filtering and quality control.

8.4 Summary

Despite the introduction of the RFWF to the radar footprint, agreement between ADCP and radar current measurements are good. For the majority of instances the Bragg scattering peaks can be easily identified in the Doppler spectra with sufficient SNR.

When conditions are poor for HF radar measurement some data spikes can occur. Although accounting for only 1% of the total measurements, data spikes can become significant in statistical analysis. Applying a threshold limit that disregards unrealistic current measurements is the simplest computational approach to dealing with these prior to data publication. Employing a limit to the difference between consecutive current measurements, similar to that employed by the Buoy for Hs, may also be an effective removal method.

Due to the robustness of the Formby radial component to noise and correlations with in situ ADCP that are amongst the highest reported in the field, > 0.9, additional processing for current measurements would be unnecessary at this stage. These options will also reduce current data availability.

Without additional quality control, agreement between the HF radar and buoy wave measurements is poor at the RFWF for both the 2009 and 2010 time periods used in this comparison. Applying a 1 m high pass filter to the buoy Hs measurements and then comparing HF radar Hs measurements for the same time improved both the 2009 and 2010 correlations and rms differences. The improvements were most significant for the HF radar cells co-located with the RFWF in 2010. It is also evident that the correlations at RFWF, relative to the mean after filtering, have decreased post wind farm installation for Hs, Tp and T1.

The radio frequency selected for this deployment is too low to allow accurate wave measurement in the low sea states that dominate the wave climate in this area. By filtering the radar data to remove the low sea cases and applying de-spiking methods, the accuracy of the data improves slightly but there is still a detectable impact of both turbines and ships on wave parameter quality. However the filtering together with the original quality control procedures significantly reduces the quantity of available wave measurements making the radar a less useful tool for operational monitoring of waves in these conditions.

It is clear that signals from both wind turbines and ships are providing spurious wave measurements particularly in low sea conditions. Chapter 9 looks at investigating the wind farm backscatter evident in the Doppler spectra. The removal of this prior to current and wave measurement should then improve wave data availability and increase agreement with buoy data.

Chapter 9

Wind farm clutter mitigation

9.1 Introduction

The previous three chapters have focused on the radar performance compared to in situ measurement devices. Chapter 6 has looked at HF radar and ADCP agreement through tidal amplitudes, chapter 7 has reviewed the long time statistics of current measurements at the NHWF and chapter 8 has discussed the impact of the RFWF on measurements of currents and waves.

For current measurements further mitigation of WTI is not necessary. It is shown by Robinson *et al.* [2011] and Robinson *et al.* [2013] that only around 1% of data is affected and the measurements are to an industry high standard. Robinson *et al.* [2013] does however show that if consistent, quality wave measurements are to be obtained in the vicinity of the RFWF the possible mitigation in the Doppler spectra before the inversion for wave measurements should be investigated.

This chapter attempts to quantify the wind turbine interference (WTI) in terms of the radar cross section (RCS) and operational parameters of the wind turbines. The Doppler spectra are investigated for evidence of WTI and frequency identification within the Doppler spectra is attempted. The characterisation of the WTI within the Doppler spectra is tested for different radar chirp lengths and automatic identification and removal is discussed. HF radar current and wave measurements with in situ devices before and after wind turbine frequency removal from the Doppler spectra are evaluated.

The radar cells where mitigation is attempted are those co-located with the RFWF as it has been established by Robinson *et al.* [2011] and Robinson *et al.* [2013] that the location within the radar footprint should result in excellent radar measurements if it were not for the wind turbines.

9.2 Wind turbine clutter

Wind farm operations vary with time as wind parameters change. In Liverpool Bay the cut in and cut out wind speeds, 4 m/s and 25 m/s respectively, are in operation at NHWF, BBWF and RFWF. Average wind speeds of 9 m/s correspond to the nominal rotation speeds given in table 9.1.

Description	NFWF	BBWF	RFWF
Operating company	N Power	DONG Energy	N Power
Turbine Model	Vestas V80 2 MW	Siemans 3.6 MW	Siemans 3.6 MW
Turbine number	30	25	25
Energy production	40,000 HE per annum	80,000 HE per annum	61,000 HE per annum
Support tower material	Steel		
Blade materials	Carbon fibre	Fibreglass reinforced epoxy resin	
	Copper Wire		
Blade diameter	3.5 m max	4.2 m max	
Nacelle height above mean sea level	67 m	83.5 m	80 m
Rotator diameter	80 m	107 m	
Blade length	39 m	52 m	
Nominal rotation speed	16.7 rpm	13.5 rpm	
Blade tip velocity	37 – 80 m/s	28 – 73 m/s	

Table 9.1: Operating parameters and site statistics of the North Hoyle (NH), Burbo Bank (BB) and Rhyl Flats (RF) wind farms (WF). HE refers to Homes Equivalent, a measurement of energy where 1 HE (Homes Equivalent) is the energy required to power 1 home for 1 year. Data is provided by the wind farms' operating companies.

Given the wind turbine dimensions in table 9.1 and using equations 2.8 and 2.7 an estimate has been made of the RCS of a wind turbine from each of the wind farms in Liverpool Bay using the method outlined in Riddolls [2005] as discussed in chapter 2.

The substructure, or plinth, that supports the tower is ignored as in Liverpool Bay these are below the surface of the water. In this case the blade shape is treated as a cylinder with the mean radius being used based on the maximum radius at the base and minimum radius at the tip. The towers, constructed of steel, are treated as solid cylindrical tubes of a constant diameter. Their surfaces have been approximated as flat and orientated in the same plane as the electric field, although slightly sloping in reality. Equation 2.8 will then give a maximum estimate of the tower RCS value, given in table 9.2. Although tower RCS values are large by comparison, they are low enough that the receive antennas are not overloaded by the zero Doppler signal return of the tower. Because of this the signal return from the tower is not considered to be a problem.

Wind turbine RCS at 13 MHz		
Wind Farm	Tower m^2	Blade m^2
North Hoyle	8,570	360
Burbo Bank	13,300	640
Rhyl Flats	12,200	640

Table 9.2: Maximum radar cross section (RCS) estimates at 13 MHz for a wind turbine at the North Hoyle, Burbo Bank and Rhyl Flats wind farm following the method of Riddolls [2005].

The blade is in reality a complicated shape of varying diameter and a tapered design. The blade orientation relative to the radar varies in 3 dimensions but the case for maximum RCS was considered. The blade RCS was estimated as a combination of a dielectric cylinder representing the main body of the blade and a thin highly conducting cylinder representing the lightning conductor running the length of the blade.

RCS estimates for both the blade and tower were done at 13 MHz and are significantly different from the 4 MHz results calculated by Riddolls [2005]. This highlights how variable the RCS value, given by equations 2.7 to 2.10, is depending on the operating frequency in use.

Table 9.2 shows North Hoyle turbines to have a smaller RCS than Rhyl Flats. This was expected due to the larger dimensions of the Rhyl Flats turbine. Figure 9.1 shows the maximum RCS values as expected at 90^o and 270^o for 1 blade rotating through 360^o. The 3 blade turbine design at RFWF will have RCS maxima offset from each other by 60^o for one complete rotation, as shown in figure 9.2.

The RCS values were also calculated using the method set out by Tennant & Chanbers [2006]. The approach is very similar however the blade is estimated to be a rectangular, flat, metal plate of width W and length L, where W was taken to be the average diameter of the blade. The maximum RCS values, 225 m^2 at NHWF and 400 m^2 at the RFWF, were less by roughly 40% each. This is the same as the percentage reduction in area when we go from a cylinder of area πrL to a rectangle of area WL where $r = W/2$. The method used by Tennant & Chanbers [2006] results in higher estimates of the RCS and the method of Riddolls [2005] will be more realistic.

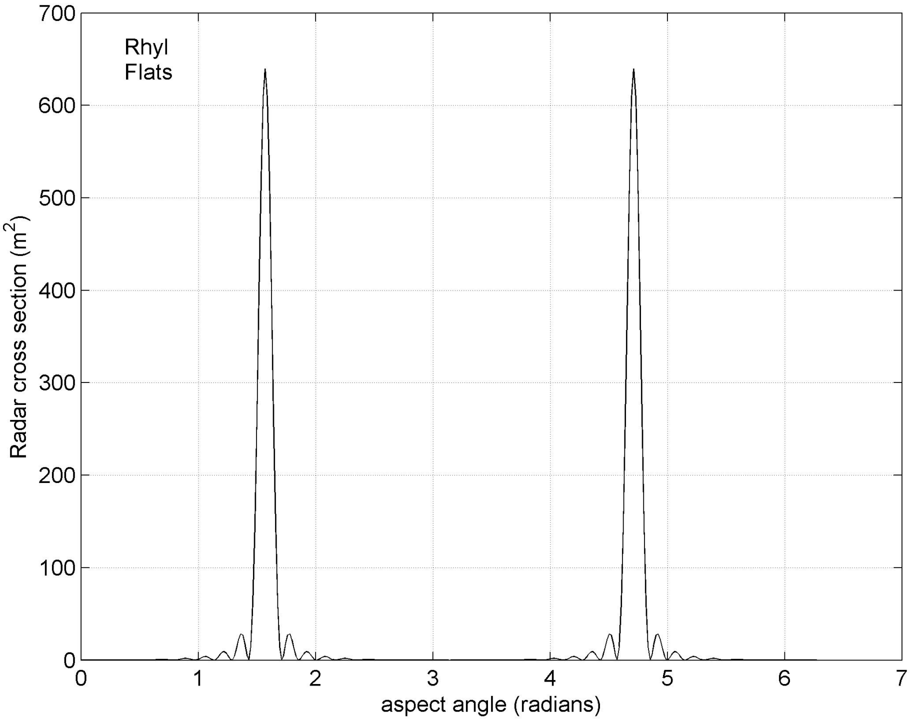

Figure 9.1: Radar cross section variation with aspect angle for a turbine at the Rhyl Flats wind farm (RFWF) with radar operating frequency of 13 MHz.

9.3 Manual signal identification

Doppler spectra of backscatter from the ocean in the region of the RFWF were examined by eye with a focus on co-located radar cells 138 and 158. The elevated noise floor at Llanddulas is immediately evident when comparing Doppler spectra from the two HF radars. Examples at cell 138, figure 9.3, and cell 158, figure 9.4, show that the Formby noise floor is typically 20 dB lower than at Llanddulas at these locations. Site and installation-specific reasons will account for around 6 dB of this, as discussed in earlier chapters, with the remainder attributed to the RFWF.

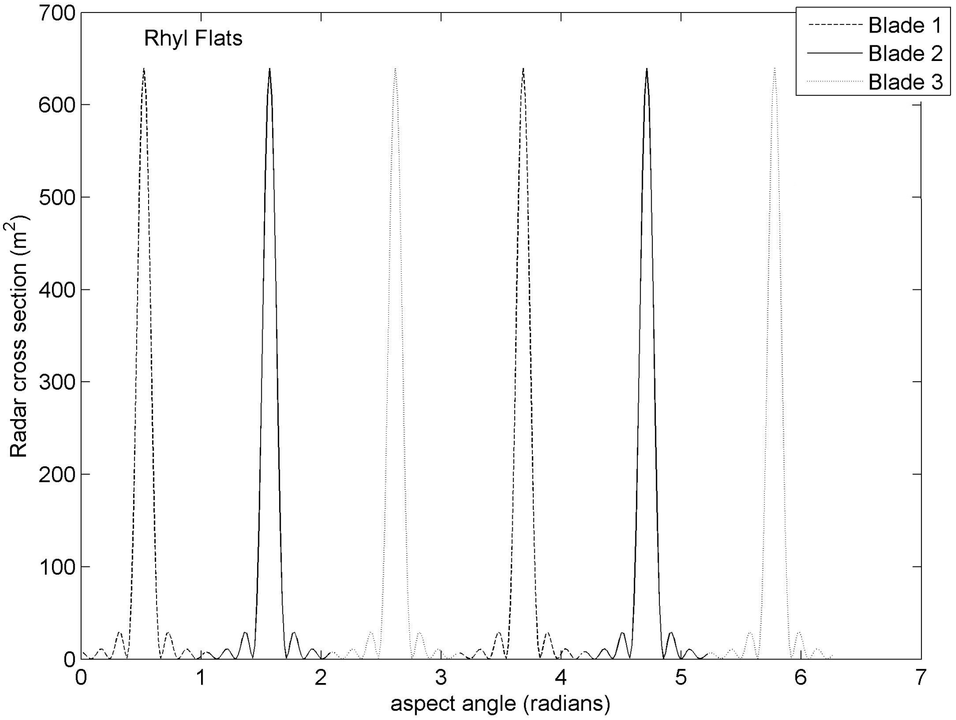

Figure 9.2: Radar cross section variation with aspect angle for 3 turbine blades at the Rhyl Flats wind farm (RFWF) with radar operating frequency of 13 MHz.

The distance to cell 138 is 11 km from Llanddulas and 42 km from Formby. This will also be acting to exaggerate the difference due to the $1/R^2$ signal strength drop-off, but all Doppler spectra features are still easily identifiable.

Characteristic Doppler spectra for the wind farm location generally have one of two forms: 1) A relatively high energy sea state with identifiable first and second order regions and frequencies symmetrical about 0 Hz of uncharacteristic large amplitude, as in figures 9.3 and 9.4 a) and b) and 2) A Gaussian-like base centred around 0 Hz with an increased number of periodic symmetrical frequencies with broad large amplitudes peaks, as in figures 9.3 and 9.4 c), d), e) and f).

Figures 9.3, 9.4 and table 9.3 present data from the same three specific time periods on April 1^{st} 2010. At $02:00$ winds of almost 17 m/s are recorded at the Hilbre Island Meteorological Station. The sea state at this time is high with the buoy Hs measuring 2.7 m and strong currents being given by ADCP B. Figures 9.3 a) and 9.4 a) show there to be little WTI in the Formby Doppler spectra at $02:00$ however the Llanddulas Doppler spectrum at this time, as seen in figures 9.3 b) and 9.4 b), is dominated by the large amplitude, symmetrical peaks at large frequencies. With the wind turbines expected to be operating at their nominal rotational speed, as given in table 9.1, a signal modulation similar in response to that of the RCS shown in figure 9.2 is later shown to explain this shape.

The agreement of HF radar current measurements with ADCP B at cells 138 and 158, as given in table 9.3, is reasonable for individual measurements based on the rms differences reported by Robinson *et al.* [2011] and Robinson *et al.* [2013], as discussed in chapters 7 and 8. The radar Hs measurement at this time is however very close to that of the buoy, within 40 cm at cell 158 and 10 cm at cell 138, and well within the rms differences of 60 cm discussed in chapter 8 [Robinson *et al.*, 2013]. This shows that even with the strong turbine modulation of the Llanddulas Doppler spectra, seen in figure 9.3 b) and 9.4 b), in a high sea state HF radar and in situ buoy and ADCP measurements can agree within expected limits.

At 19 : 00 in the Formby Doppler spectrum for cell 138, figure 9.3 c), and cell 158, figure 9.4 c), the broad amplitude peaks described earlier as form 2 can be identified. The corresponding wind speed of 1.9 m/s recorded at Hilbre Island Meteorological Station is low. As expected, the sea state is also low with the buoy measuring 63 cm. This wind speed is below the wind turbine operational cut off of 4 m/s but evidence of the wind turbine rotation is clearly seen in the Doppler spectrum. It is possible that the offshore winds at the RFWF are above the required 4 m/s. It is also possible that the wind turbines are not generating electricity but are still free to rotate about their axis. With such light winds the wind turbines would be rotating very slowly. A slow rotation would act to broaden the sharp peaks seen at 02 : 00 in figure 9.3 b) and 9.4 b). The slower rotation could also account for the high noise floor seen in the Doppler spectrum of figure 9.3 d), where the SNR is too small for a current radial measurement. At 19 : 00 the HF radar and ADCP measurement agreement is poor at the RFWF site and the radar measurement quality is also too low to undergo full inversion for a wave or dual current measurement. Figure 9.3 f) shows that at 22 : 00 the SNR is much greater allowing for radial measurements from both radars. There is also a much stronger current measured by the ADCP, 78 cm/s, and the HF radar measurement is within 14 cm/s of this at both measurement cells. This is within the rms difference reported in chapter 8 [Robinson *et al.*, 2013]. The first-order scattering machanism has enough energy that when the first-order Bragg peaks are located, the SNR is greater than the 10 dB required for a current measurement. It is not however the case for second-order scattering mechanisms and no full inversion is possible for wave parameters at 22 : 00. With a less energetic sea state the validity of wave measurements will be low regardless of the wind farm presence and below a Hs of 0.5 m it is unlikely a measurement would be made.

Figure 9.5 shows the averaged Doppler spectra for the month of April 2010 for 20 past the hour measurements. At this time the averaging period is double that of 00 and 40 past the hour to allow for better measurement of the second-order sea state. It is evident that certain frequencies repeat with larger than expected amplitudes even in the tails of the Doppler spectra. Through manual inspection all the outer peaks in figure 9.5 are found to be at exactly the same frequencies, ± 0.67 Hz, ± 1.34 Hz and ± 1.84 Hz.

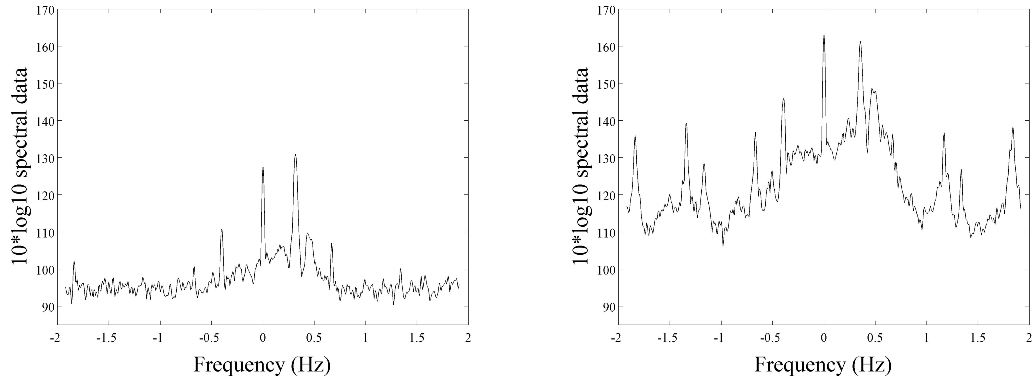

a) Formby, Cell 138, 201004010200 b) Llanddulas, Cell 138, 201004010200

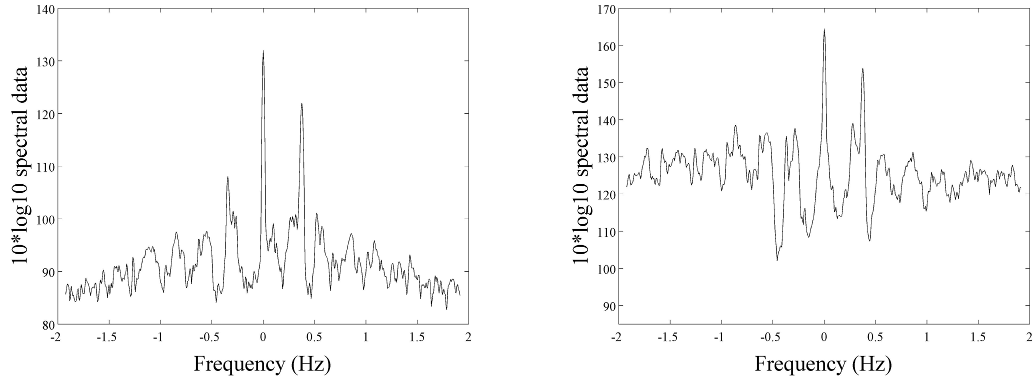

c) Formby, Cell 138, 201004011900 d) Llanddulas, Cell 138, 201004011900

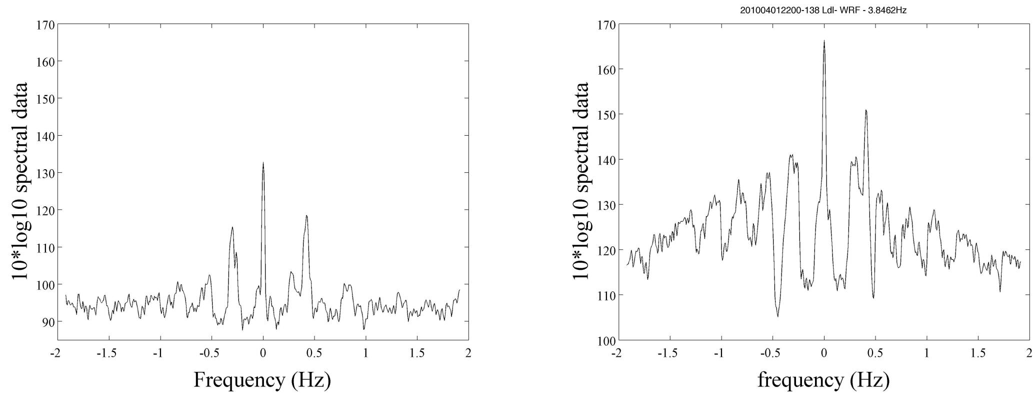

e) Formby, Cell 138, 201004012200 f) Llanddulas, Cell 138, 201004012200

Figure 9.3: Doppler Spectra examples from cell 138, co-located with the Rhyl Flats wind farm.

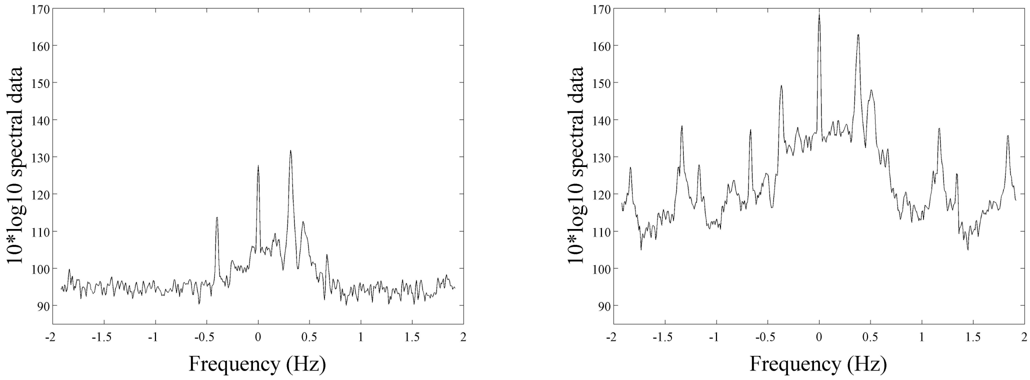

a) Formby, Cell 158, 201004010200 b) Llanddulas, Cell 158, 201004010200

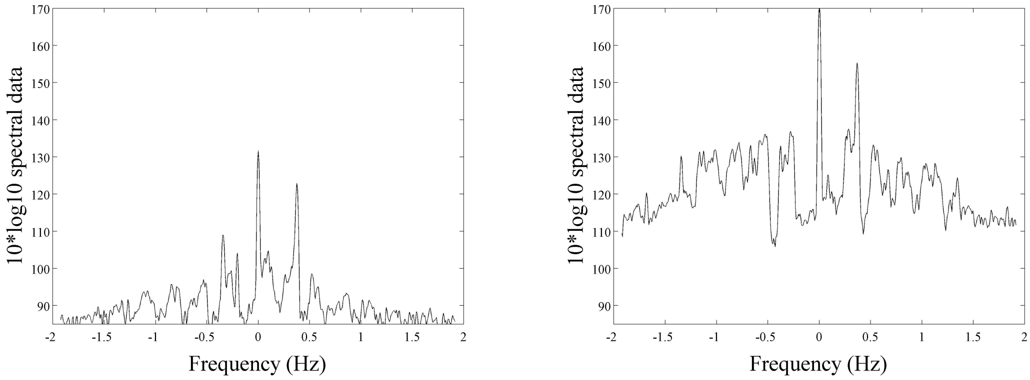

c) Formby, Cell 158, 201004011900 d) Llanddulas, Cell 158, 201004011900

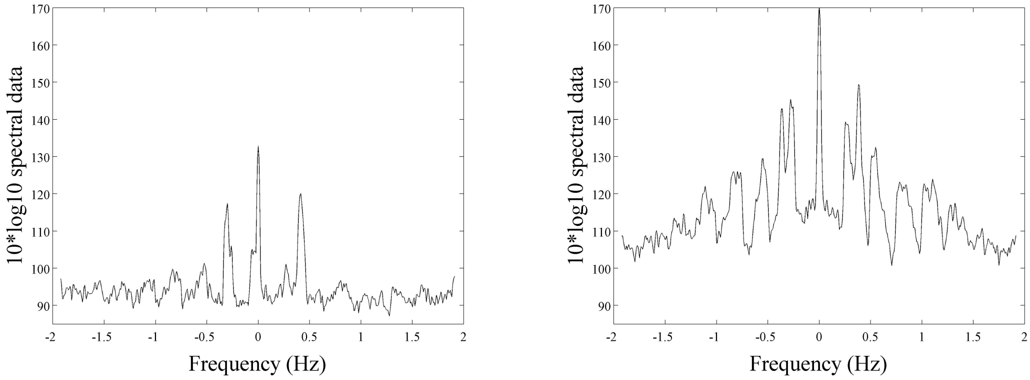

e) Formby, Cell 158, 201004012200 f) Llanddulas, Cell 158, 201004012200

Figure 9.4: Doppler Spectra examples from cell 158, co-located with the Rhyl Flats wind farm.

Figure 9.6 shows all four plots of figure 9.5 on the same axis with the identified frequencies indicated. 0.67 Hz is almost a multiple of the Bragg frequency, 0.38 Hz, as is 1.34 Hz. Therefore some amplitude at these frequencies could be second and fourth order harmonics from ocean scattering, though if this were the case a third harmonic of reasonable amplitude should also be seen in figures 9.5 and 9.6 at around 1.05 Hz and it is not. The energy from the first-order scattering off the ocean is also spread around the Bragg frequency as it is shifted by the moving currents and

Time: April 2010 day-time	01 – 0200	01 – 1900	01 – 2200

Hilbre wind magnitude (m/s)	16.9	1.92	4.97
Hilbre wind direction	297	192	145

ADCP B east current (cm/s)	−83	−3	78
ADCP B north current (cm/s)	28	−1	5

Buoy Hs (m)	2.71	0.63	0.42

Radar cell 138	FBY	LDL	FBY	LDL	FBY	LDL
Radial current velocity (+ away) (cm/s)	−53	−22	18	–	76	38
Hs perpendicular (m)	2.43	5.7	2.81	–	4.05	8.41
Hs parallel (m)	1.73	2.75	1.88	–	2.33	3.46
Dual vector current magnitude (cm/s)	62		–		92	
Dual vector current direction	174		–		−9.6	
Dual Radar vector current east (cm/s)	−61		–		90	
Dual Radar vector current north (cm/s)	6		–		−15	
Radar Hs (m)	2.81		–		–	

Radar cell 158	FBY	LDL	FBY	LDL	FBY	LDL
Radial current velocity (+ away) (cm/s)	−53	6	20	−5	62	13
Hs perpendicular (m)	3	3.86	1.98	2.87	2.16	7.27
Hs parallel (m)	1.96	2.19	1.54	1.85	1.62	3.18
Dual vector current magnitude (cm/s)	59		21		83	
Dual vector current direction	180		8.82		−15.3	
Dual Radar vector current east (cm/s)	−59		20		80	
Dual Radar vector current north (cm/s)	0.1		3		22	
Radar Hs (m)	2.42		–		–	

Table 9.3: Three instances of oceanic and atmospheric parameters measured by in situ and HF radar measurement devices in Liverpool Bay.

is not a sharp peak as seen at 0.67 Hz, 1.34 Hz and 1.84 Hz. It is more likely then that these sharp peaks at identical frequencies are caused by some other scattering mechanism that is consistent throughout the time period of a month.

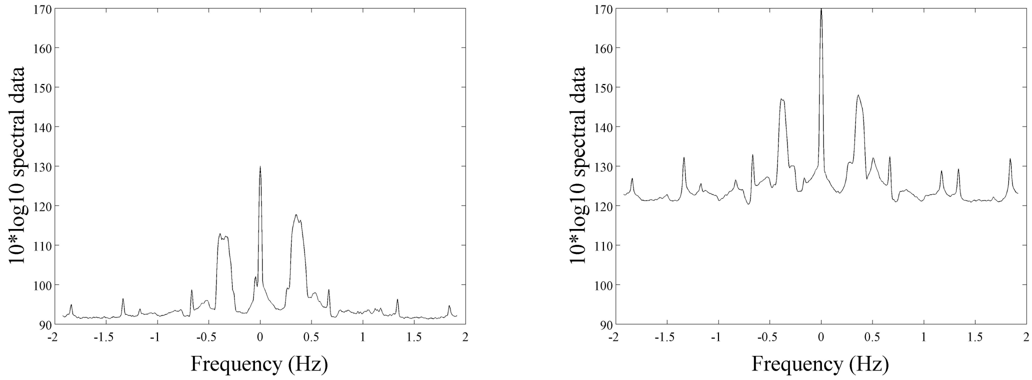

a) Formby, Cell 138 b) Llanddulas, Cell 138

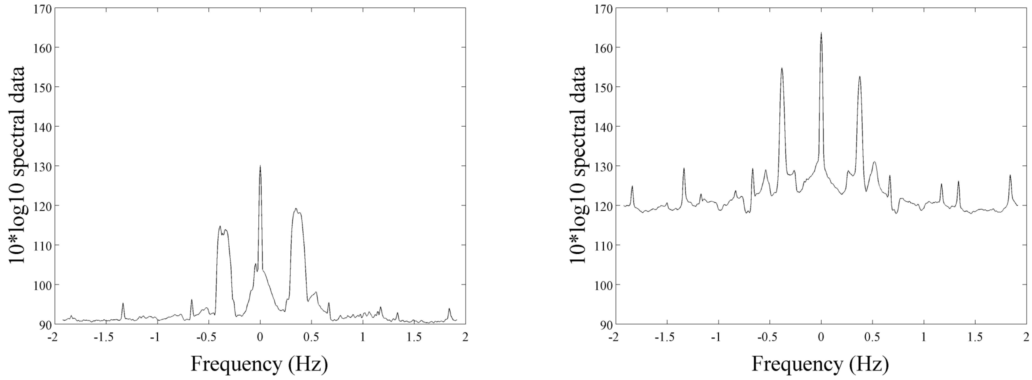

c) Formby, Cell 158 d) Llanddulas, Cell 158

Figure 9.5: Doppler Spectra average April 2010 from cells co-located with the Rhyl Flats wind farm: a) Formby - cell 138 b) Llanddulas - cell 138 a) Formby - cell 158 b) Llanddulas - cell 158

The nominal operating frequency of the RFWF, as given in table 9.1, is 13.5 rpm. This corresponds to a time period of 4.44 s and a frequency of 0.225 Hz. However, this is for one blade, and as discussed earlier in the chapter, three high return RCS modulations are expected which would triple the frequency to 0.675 Hz. On a more detailed inspection of the plots this is found to be within one spectral bin of the 0.67 Hz peak identified in figure 9.6. A corresponding positive and negative symmetry about 0 Hz is also predicted due to the blades moving towards the radar 3 times in one revolution and away from the radar 3 times in one revolution as well, at inherently identical speeds. The second harmonic from the WTI of 1.34 Hz is then also identified and a third is predicted at 2.01 Hz. This, as well as further harmonics, are expected from the RCS model shown on figure 9.2. The number of harmonics we would expect to see in the Doppler spectra is however limited by the selected radar chirp frequency. The Doppler spectra frequency range, ± 1.92 Hz, therefore makes the 2.01 Hz third WTI harmonic outside the frequency range of the Doppler spectra. Peaks also occur at frequencies not predicted by the wind turbine model,

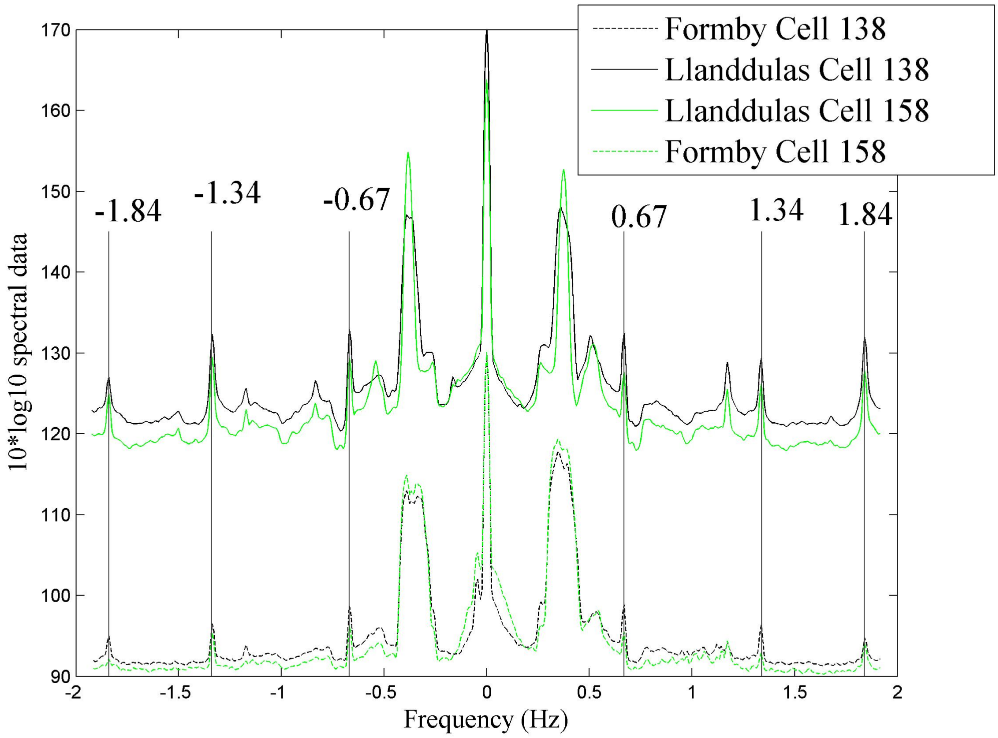

Figure 9.6: Doppler Spectra average. Twenty minutes past the hour measurement, April 2010 from cells co-located with the Rhyl Flats wind farm.

these are however only distinguished in the Llanddulas spectra.

As the large RCS given in table 9.2 would suggest, the stationary return with zero Doppler frequency shift, as seen in figure 9.7, is largest at the wind farm location and generally diminishes with distance away from the wind farm. Figure 9.7(a) does however show that the amplitude remains large for up to roughly 6 cells, whereafter it appears there is a fairly constant energy at 0 Hz.

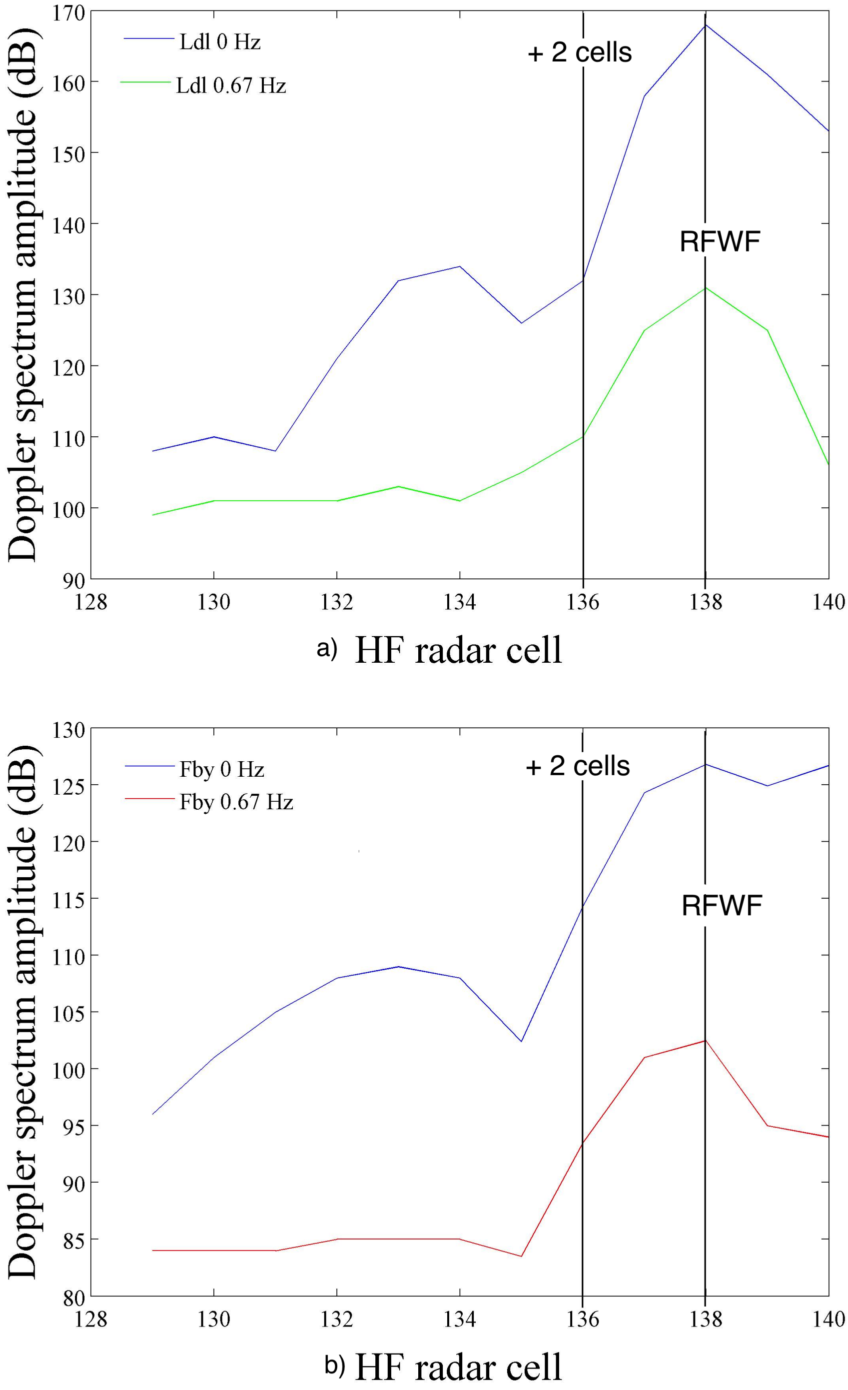

Figure 9.7: Llanddulas (Ldl) (a) and Formby (Fby) (b) Doppler spectrum amplitudes at 0 Hz and 0.67 Hz for cells 129 to 140 on April 15th 2010 at 18 : 20. The RFWF is indicated by the black line at cell 138 and 2 cells away by the black line at cell 136.

The extent of the wind farm influence from blade rotation on the Doppler spectra is seen in figure 9.7 to be 2 cells in the north-south look direction from Llanddulas and the east-west look direction of Formby. This would be expected as the amplitude of the harmonics in the Doppler spectra is genarally seen to decrease with increasing harmonic number. The average noise of the Doppler spectra, discussed in chapter 5, supports this, as elevated noise extends for between two and three cells before dropping off to normal levels.

The projection of the wind turbine influence into cells not co-located with the wind farm suggests that third, fourth and possibly fifth harmonics of the wind turbine would be located in adjacent measurement cells. The range and azimuthal processing will also make this a possibility. Some of the radar cells will be directly observing some WTI but also that of the adjacent cell. For example cell 138 is co-located with the RFWF but also adjacent to cell 158 which is also co-located with the RFWF, and vice versa. To confirm that the suspected modulation frequencies of the wind turbine greater than $\pm$ 1.92 Hz are sampled into the next measurement cell the Doppler frequency range was extended in a month long experiment during April 2010, detailed in the next section. This allowed for a third unambiguous harmonic to be observed in the Doppler spectra and predictions to be investigated regarding where the wind turbine amplitude modulations would appear in the Doppler spectrum.

9.4 Extended frequrncy range measurements

For the wind turbine nominal operating frequency, f_{wt}, of 0.67 Hz, large amplitude spikes are expected at $\pm$ 0.67 Hz, $\pm$ 1.34 Hz ($2xf_{wt}$), $\pm$ 2.01 Hz ($3xf_{wt}$) and so on. The length of time taken for the 50 kHz bandwidth signal to be transmitted, the sweep frequency time, is a standard 0.26 s. This is then the sample time for the received signal at each range and each sweep is analysed with an FFT to give one sample per range. The Doppler bandwidth is $1/\text{sweep frequency time}$ and, for the standard 0.26 s, results in a sample frequency of 3.846 Hz and Doppler spectra frequency range of -1.923 Hz to 1.923 Hz. As the Doppler spectrum cuts off at $\pm$ 1.923 Hz any frequencies larger than this will appear in the next measurement cell. The third WTI harmonic expected at 2.01 Hz would exceed the immediate cell by 0.087 Hz. It is suspected that this will result in the third WTI harmonic being located 0.087 Hz into the adjacent Doppler spectrum. Counting down 0.087 Hz from 1.923 Hz you arrive at 1.84 Hz, exactly what is observed in the initial inspection of the averaged Doppler spectra in figure 9.6. This evidence suggests that any wind turbine frequency modulation outside the Doppler spectral frequency range -1.923 Hz to 1.923 Hz would appear in the adjacent Doppler spectra. This idea is consistent with the sampling of the continuous data collection by the processing software.

Considering then unambiguous wind turbine frequency modulations in the standard operating mode of 0.26 s, two wind turbine modulations are expected and observed in the positive and negative Doppler spectral regions. If the sweep frequency time were then decreased the Doppler bandwidth at each range would increase. The HF radar allows for up to six 10 minute measurement periods every hour, incorporating data collection and processing into this time. As discussed in chapter 4, NOCL makes three measurements per hour utilising four of the possible six measurement periods (a longer averaging time for one of the three measurements takes up two of the possible six measurement periods). During the month of April 2010 both the Llanddulas and Formby radar were configured to make additional measurements at the 10 minute and 50 minute measurement slots. This allowed for the use of two shorter sweep frequency times, 0.195 s and 0.21667 s, extending the Doppler spectral frequency range to ± 2.564 Hz and ± 2.308 Hz, respectively. Full operating parameters for the month of April 2010 are given in table 9.4 for Llanddulas and table 9.5 for Formby. With the chirp frequency large enough it is expected that a peak would be observable at ± 2.01 Hz and that there would no longer be a peak at ± 1.84 Hz.

Time past the hour	Frequency (MHz)	Chirp Length (s)	Sample Frequency (Hz)	Doppler spectra range (Hz)	Doppler spectra resolution (Hz)
00	13.430	0.26	3.836	± 1.923	0.0075
10	13.430	0.195	5.128	± 2.564	0.0100
20	13.465	0.26	3.846	± 1.923	0.0075
40	13.395	0.26	3.846	± 1.923	0.0075
50	13.430	0.21667	4.615	± 2.308	0.0090

Table 9.4: The Llanddulas radar operating parameters for April 2010.

Figure 9.8 shows the average Doppler spectra for the extended Doppler frequency range at ten minutes past the hour in April 2010. As was the case for the twenty past the hour average shown in figure 9.6, both Llanddulas and Formby Doppler spectra are seen in figure 9.8 to consistently have high energy spikes at identical frequencies. With the extension of the frequency range the spike, which did occur at ± 1.84 Hz for the standard frequency range shown in figure 9.6, is now absent. Based on the first two spikes being exact multiples of each other it was expected that the ± 1.84 Hz peak would be identifiable in the extended frequency Doppler spectra at ± 2.01 Hz. This is what is seen in the Doppler spectra average for the extended frequency range at ten past the hour (figure 9.8). The spikes in the Doppler spectra have behaved exactly as predicted confirming the existence of subsequent harmonics in adjacent measurement cells to those directly observing the RFWF.

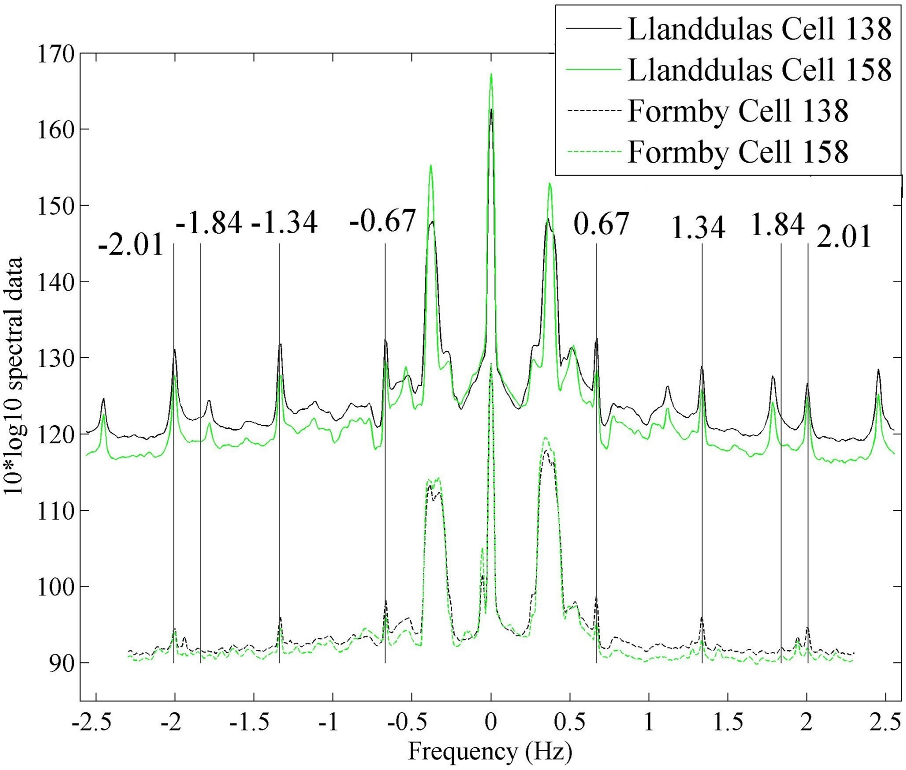

Figure 9.8: Identification of the wind turbine spectral energy from the direct HF radar cell in the Doppler spectra average. Ten minutes past the hour measurement, April 2010 from cells co-located with the Rhyl Flats wind farm.

Time past the hour	Frequency (MHz)	Chirp Length (s)	Sample Frequency (Hz)	Doppler spectra range (Hz)	Doppler spectra resolution (Hz)
00	12.450	0.26	3.836	± 1.923	0.0075
10	12.450	0.21667	4.615	± 2.308	0.0090
20	12.465	0.26	3.846	± 1.923	0.0075
40	12.435	0.26	3.846	± 1.923	0.0075
50	12.450	0.195	5.128	± 2.564	0.0100

Table 9.5: The Formby radar operating parameters for April 2010.

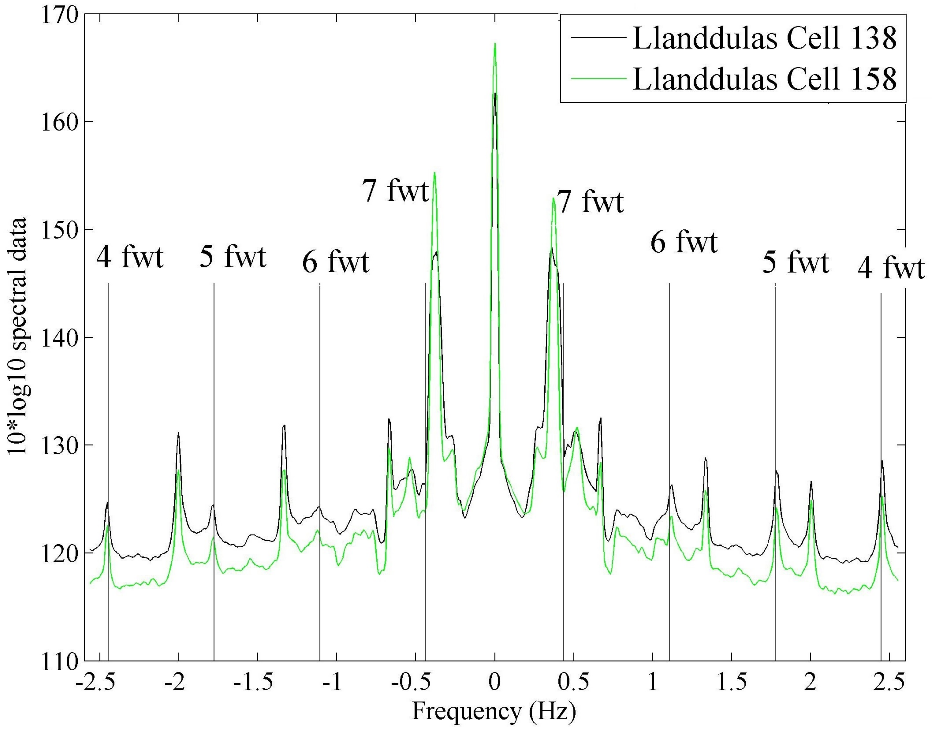

Figure 9.9: Identification of the wind turbine spectral energy from an adjacent HF radar cell in the Doppler spectra average. Ten minutes past the hour measurement, April 2010 from Llanddulas HF radar cells co-located with the Rhyl Flats wind farm. Multiples of the wind turbine modulation frequency are indicated by a number followed by fwt.

With the first and second harmonics of the suspected wind turbine modulation identified, as well as the predicted shift of the third harmonic confirmed, the expected frequencies of the fourth, fifth, sixth and seventh harmonics can more confidently be calculated.

Figure 9.9 shows the Llanddulas averaged Doppler spectra for ten past the hour, as in figure 9.8. The expected locations of the forth, fifth and sixth harmonics of the wind turbine modulation can be seen to have located additional high energy peaks in the averaged Doppler spectra. For the standard chirp length used by NOCL, also the chirp length for figure 9.6, fourth and fifth harmonics would be expected at ± 1.17 Hz and ± 0.5 Hz. Figure 9.6 shows this to be the case but the energy at these frequencies, represented by their spectral amplitudes, are starting to reduce. Any further harmonics would then be expected to appear in a third cell with continued diminishing amplitude.

Harmonics two to six for the shorter chirp length and two to four for the standard chirp length have fallen outside the frequency range where wave measurements would be expected. Based on their predicted, and confirmed, location a seventh (shorter chirp length) and fifth (standard chirp length) harmonic can however be expected to fall within or near to the frequencies utilised for ocean parameter measurement.

The amplitude of the wind turbine harmonics does appear to gradually reduce. For the Formby radar measuring currents with large SNR, as reported in chapter 8, the HF radar still has very good agreement with ADCP data. For the Llanddulas radar measuring currents with much small SNR, it is possible that the seventh (shorter chirp length) and fifth (standard chirp length) wind turbine harmonic are being picked out as the Doppler shifted Bragg peak. This could be the cause of the very large current measurements that are occasionally being made by the radar when the ADCP is reporting currents close to zero, as shown in figure 8.4 d).

The additional energy from the wind turbine modulation at the frequencies used for wave measurement could be responsible for large Hs measurements by the radar. This is because the WTI will only act to add energy to the measured sea state therefore only increasing the Hs measurement. Removing this energy would then reduce the Hs measurement.

With the nature of the WTI confirmed for the nominal operating frequency it is important to remove energy added to the Doppler spectra in these circumstances. As suggested by Robinson *et al.* [2013], this will hopefully improve HF radar performance when measuring waves but may also have some benefit to current measurement as well.

9.5 Automatic identification and removal

From the inspection of the individual and averaged Doppler spectra for all chirp lengths some identifying features of the wind turbine modulation are clear: 1) A large amplitude peak with comparable energy to that of the Bragg scattering peaks will be located at ± 0.67 Hz when the wind turbines are generating electricity at the nominal operating speed. 2) At double this frequency (± 1.34 Hz) a second harmonic can be located of almost the same amplitude. These properties, which are expected in every cell where there is wind turbine modulation, have been utilised to automatically identify the frequency in the Doppler spectra where the first and second harmonic of the wind turbine modulation is occurring. The amplitude of the modulation will vary with aspect angle, see figure 9.1, but the nature of the frequency response will be consistent.

Identification of the WTI modulation peaks in the Doppler spectra starts by first selecting the range of frequencies between 0.5 to 0.85 Hz and 1 to 1.7 Hz. These are the ranges for the first and second WTI harmonics for a range of rotational speeds. Each section is divided into three bins and the peak of each bin identified. This results in three peaks in each set. These are compared and if one of the peaks found in the section 1 to 1.7 Hz occurs at a frequency which is exactly double (within 2 frequency bins) that of a peak found in the range 0.5 to 0.85 Hz they are selected as the wind turbine first and second order harmonic frequencies. When/if the first and second turbine modulation peaks are identified in the positive Doppler spectra it is required that an equivalent set exists in the negative Doppler spectra, within one spectral bin. If confirmed, the frequencies of the third to the seventh harmonics are calculated. The energy of each WTI harmonic is then reduced, and those of the two frequency bins either side, to that of a local average. The cells run through this peak reduction programme, PRMV.m, included a two or three cell buffer around the RFWF (cells 115 – 119, 134 – 139, 155 – 159, 175 – 179 and 194 – 198), cells at the NHWF (cell 217) and the radar cell co-located with the buoy measurements (cell 234). The input Doppler spectrum is a ".spec" file type and is overwritten after processing in PRMV.m by a file of the same type.

It must be considered that more than one wind turbine will fall into a HF radar measurement cell. If it is assumed that there is a uniform wind field over the wind farm, all turbines should be at the same aspect angle and angular velocity. For this case there will be more energy at the wind turbine operating frequency and its harmonics. Although not evident in the Doppler spectra presented so far, direct observation of the wind turbines however suggests different rates of rotation. For this case more than one set of harmonics will be present and at differing frequencies. Their amplitudes will also differ, along with their aspect angles. The approach of peak finding and frequency multiple matching allows for these multiple sets of wind turbine harmonics to be identified, as shown in figure 9.10.

Both the original and the peak removed ".spec" files were processed through the Seaview Sensing software for radial and dual vector current and wave measurements using default criteria.

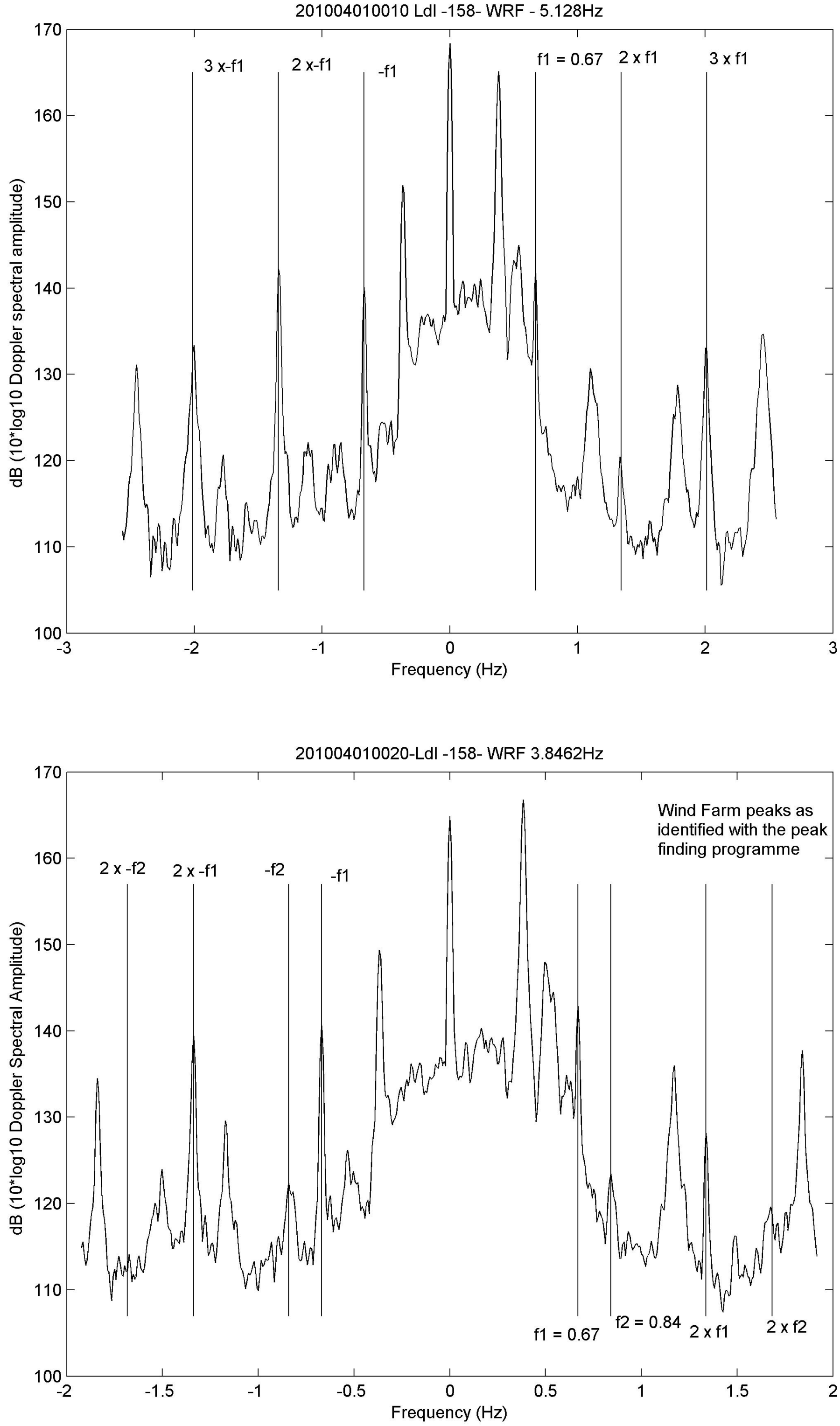

Figure 9.10: Llanddulas Doppler frequency Spectra 201004010010 and 201004010020 cell 158.

9.6 Measurement Availability

Figure 9.11 shows the original Doppler spectrum and the same spectrum after the wind turbine peaks have been identified and processed. As seen in figure 9.11, we have clear visual evidence of the wind turbines at frequencies expected through previous investigation. The energy at the identified wind farm frequencies is seen to have been slightly reduced but large amplitudes from WTI can still be seen. The WTI energy that remains outside the frequencies used for measuring currents and waves will not influence the measurement. Removal of the WTI modulation peaks will do two things: 1) make the Bragg peak clearly identifiable and 2) reduce the HF radar Hs measurement.

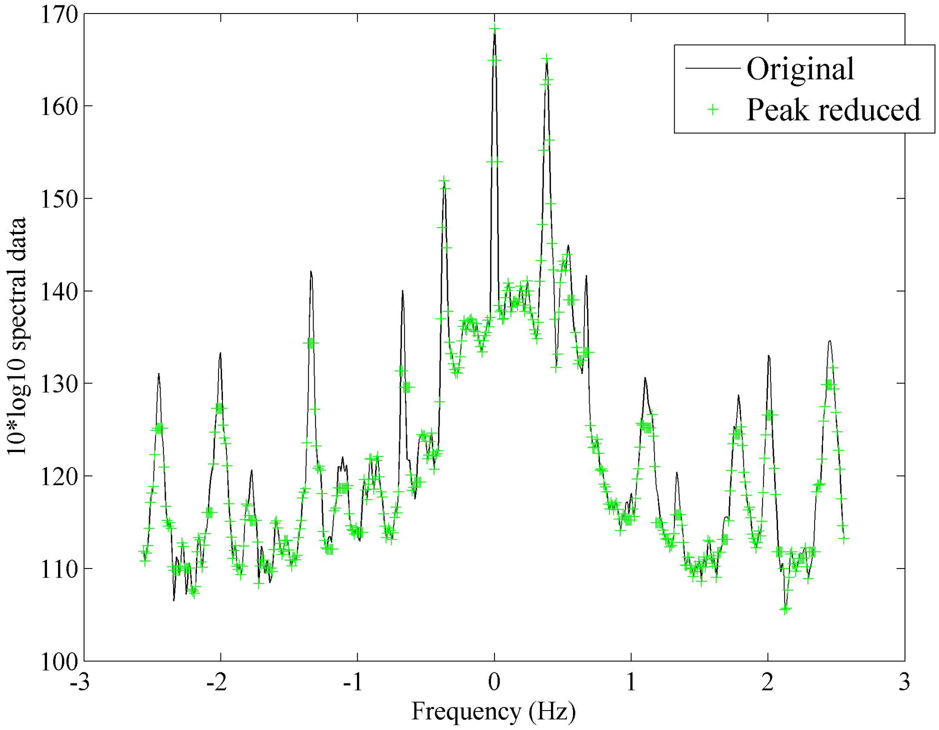

Figure 9.11: The original and peak-removed Doppler spectra from Llanddulas cell 158 at 2010-04-01 00 : 10.

When comparing the 10 minute past the hour average for the month using original and then WTI-reduced Doppler spectra in figure 9.12, a reduction in the average noise is evident. It can also be seen in figure 9.12 that the first three directly observable WTI peaks are significantly reduced as well as those from adjacent radar measurement cells. The region for current and wave measurements is significantly changed with the removal of the WTI peak at ± 0.67 Hz.

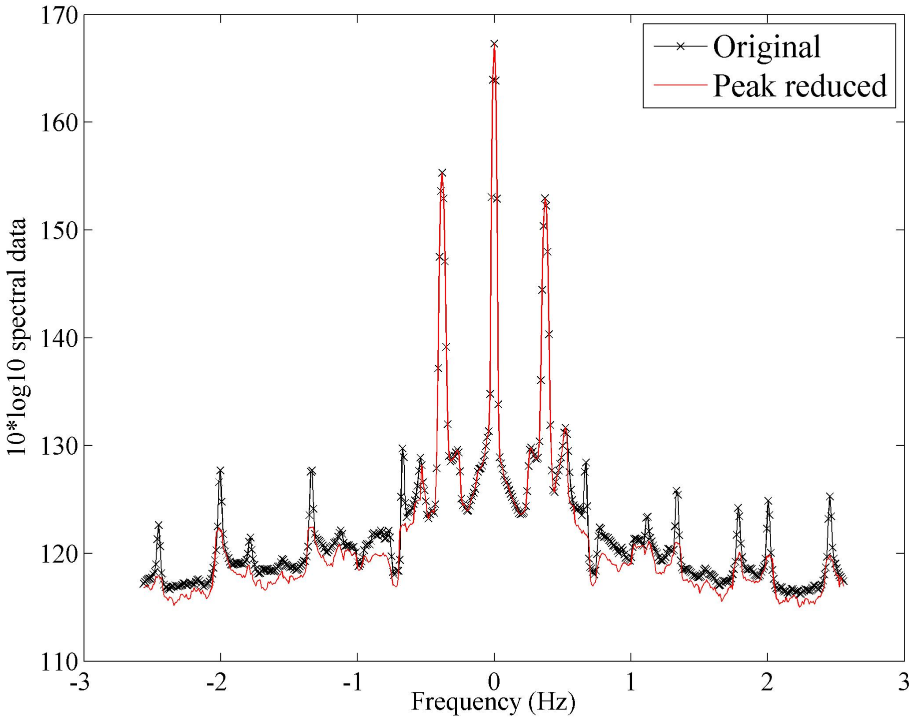

Figure 9.12: The original and peak-removed average Doppler spectra from Llanddulas cell 158 April 2010 for the ten minute past the hour measurement.

The two sets of Doppler spectra, original and WTI-removed, for April 2010 were processed using the Seaview Sensing software at The University of Sheffield. Radial currents, vector currents and sea state parameters were produced from each Doppler spectra set. The original and WTI-removed measurements were then compared, looking for differences in the data produced.

With each radar normally measuring three times an hour for 30 days a maximum of 2160 Doppler spectra would be available for each radar measurement cell. With the additional two measurement slots being utilised during the month of April 2010 this increases to 3600. Actual Doppler Spectra recorded by each radar amounted to 3596. The original Doppler spectra resulted in radial current measurements, from both Llanddulas and Formby, ranging from 88% to 95% of the time over the month of April 2010. Some examples from specific cells can be seen in table 9.6.

The least amount of possible measurements occurred at radar cell 138, at 88% data availability, followed in order by cells 197, 137 and 158. After WTI removal

Radar Measurement Cell	Radial current availability %		Vector current availability %		Hs availability %	
	Original	WTI-removed	Original	WTI-removed	Original	WTI-removed
136	94	79	71	66	23	23
137	90	77	69	66	30	31
138	88	75	66	63	34	35
156	95	79	70	66	20	20
157	92	76	69	65	29	29
158	90	76	67	64	33	33
196	94	78	73	68	26	26
197	89	77	71	67	33	33

Table 9.6: The percentage of time Doppler spectra resulted in a radial current, vector current or wave (Hs) measurement at several selected cells at or close to the Rhyl Flats wind farm.

data availability fell to between 76% and 79% with the lowest percentage availability again at cells co-located with the RFWF. The current vector availability is much less with a high of only 73% for the original Doppler spectra. Just as for the radial currents, this figure is seen to fall after the WTI removal. The examples of the current vector availability given in table 9.6 show the current vector availability has reduced by around $4-5\%$ after removal of WTI from the Doppler spectra. Is is also confirmed that the data availability is least at the cells co-located with the RFWF, cells 138 and 158.

What is clear is that the removal of WTI from the Doppler spectra has resulted in less current data availability with fewest current measurements being produced at all cells where most WTI was removed. It is possible that the SNR values have been reduced and current measurements are not valid. In the worst case this could be caused by some undesirable reduction in signal.

As the results in table 9.6 show, there is little difference between the number of wave measurements from the original and WTI-removed Doppler spectra. Some results differed by a few one hundredths of a percent which equates to only one or two measurements. Cells 137 and 138, where a more significant difference was seen, were only different by 1%, equivalent to twenty measurements. Unlike for currents, a small increase in wave data availability has occurred for two of the cells tested, with all others remaining the same or differing by less than 5 extra measurements.

Having established the effect of the WTI removal on data availability for the different measurement types, the effect on their agreement is now discussed. The original and WTI-removed data sets are compared with each other and with available in situ measurements.

9.7 Current measurements

Radial and combined vector current measurements were produced with the original and WTI-removed Doppler spectra, the data from each is compared with that of ADCP A.

Processing Formby Doppler spectra to remove WTI resulted in 44 radial current measurements that were different from those of the original Doppler spectra, less than 1% of measurements for any given cell. Low figures of mitigation, $< 0.6\%$, were also evident at Llanddulas with just 25 current measurements being different than those of the original Doppler spectra.

Figure 9.13 a) shows two examples of measurements in the radial current time series from original and WTI-removed data that differed from one another, and figure 9.13 b) shows four. The majority of measurements from the WTI-removed Doppler spectra are no different from the original. Where original and WTI-removed values are identical they are indistinguishable on figures 9.13 and 9.14. To highlight differences, WTI-removed values are shown as purple triangles and the original as a red cross. It can be seen in figures 9.13 a) and b) that the WTI-removed data are in better agreement with the ADCP data than the original. Plotted with the same conventions as figure 9.13, figures 9.14 a) and 9.14 b) also show some measurement improvement for the Llanddulas radar at cells 138 and 157, respectively. Figures 9.13 and 9.14 however also show multiple radar measurements from both Llanddulas and Formby which have characteristics of those perturbed by WTI which appear not to have rectified by the WTI mitigation process.

Figures 9.15 and 9.16 show all measurement differences between the original and WTI-removed Llanddulas and Formby radial current measurements for all cells where the WTI removal was trialled. ADCP measurements at the same instant are also plotted. A few things can be observed from these. The original radar measurements that have been altered by the WTI removal process are generally large, with the majority $> \pm 1.5$ m/s. These are physically unrealistic current measurements, particularly from the Llanddulas radar, where radial current values are expected to range between ± 0.30 cm/s [Robinson *et al.*, 2011].

Where there is a change to the radial current measurement the WTI-removed radial is closer to a more realistic value and in better agreement with the ADCP

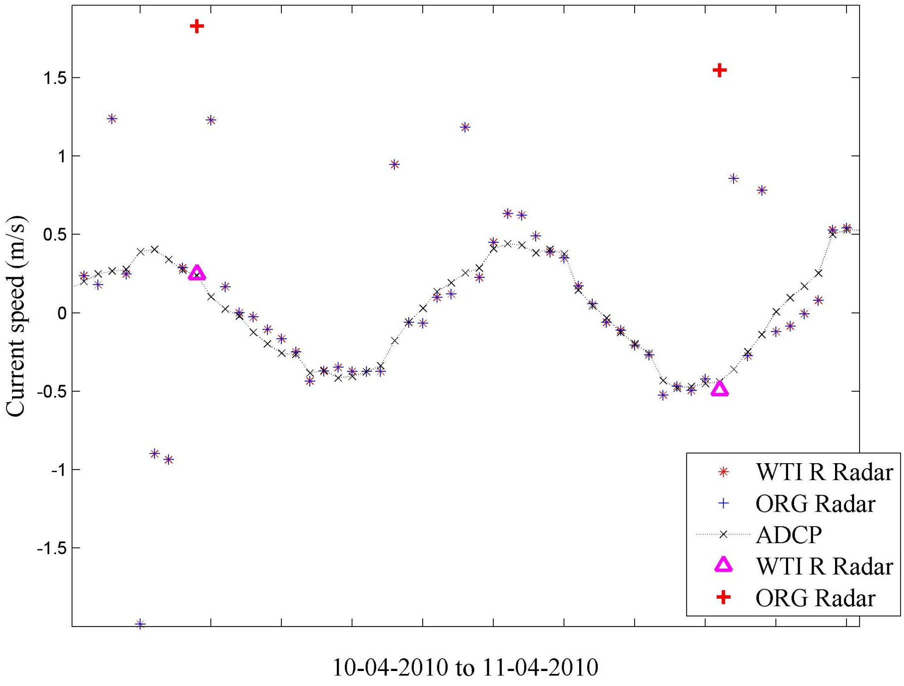

a) Cell 118

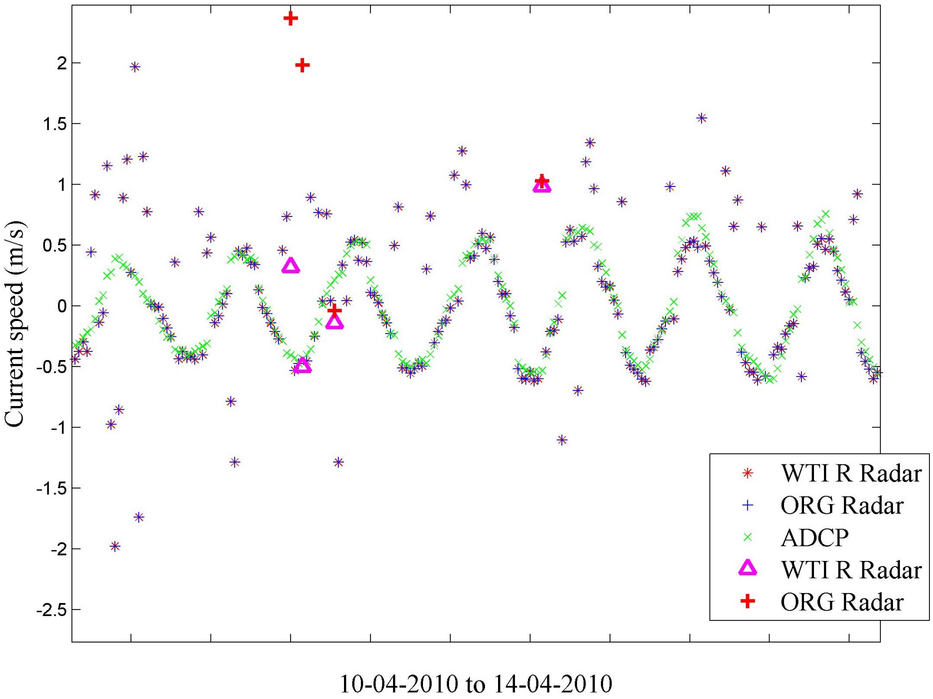

b) cell 138

Figure 9.13: The original and WTI-removed Formby radial current time series for cells a) 118 and b)138 and the ADCP current time series in the look direction of the Formby radar. Original and WTI-removed data points that are no different are shown in blue and red, respectively. Measurements differences are shown as a red cross for the original data and a purple triangle for the WTI-removed data.

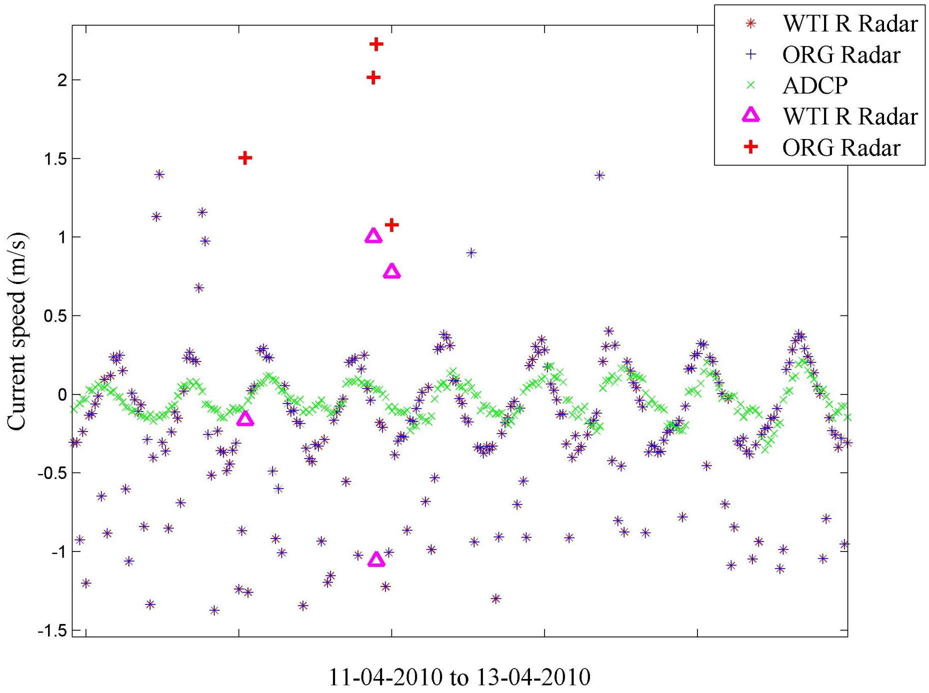

a) Cell 138

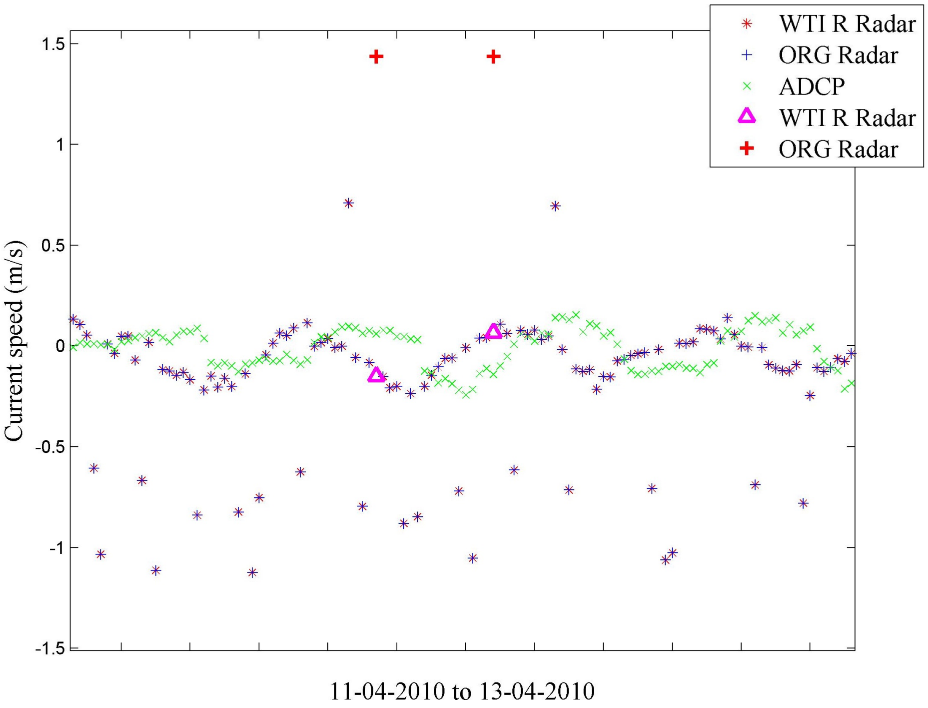

b) cell 157

Figure 9.14: The original and WTI-removed Llanddulas radial current time series for cells a) 138 and b)157 and the ADCP current time series in the look direction of the Llanddulas radar. Original and WTI-removed data points that are no different are shown in blue and red, respectively. Measurements differences are shown as a red cross for the original data and a purple triangle for the WTI-removed data.

current measurement, as shown on figure 9.15. The rms difference, see table 9.7, between the Llanddulas radar and ADCP data points on figure 9.15 has improved from 1.9 m/s for the original data to 0.9 m/s for the WTI-removed data but improvements in individual cell time series are negligible due to the small number of points that were altered and the large number of spikes that remained.

Measurement Detail	Difference Number	rmsd (m/s) ORG-ADCP	rmsd (m/s) WTI-removed-ADCP
Formby Radial	44	2.1	0.8
Llanddulas Radial	25	1.9	0.9
Radar east	15	1.1	1.2
Radar north	15	0.8	0.7

Table 9.7: Original and WIT-removed current measurements compared with ADCP A. The difference number is the number of measurements where the original and WTI-removed data differed from one and other and rmsd denotes the root mean square difference.

On figure 9.16 again we can see WTI removal has acted to decrease the magnitude of the radial current measurement. For about 20% of the points seen on figure 9.16 the WTI-removed current measurement is improved and also in very good agreement with ADCP. The rms difference for the Formby radial measurements has also reduced from 2.1 m/s for the original data to 0.8 m/s for the WTI-removed data.

When the Llanddulas and Formby radar measurements were combined for east and north vectors only 15 WTI-removed measurements differed from those of the original. These 15 points are plotted on figures 9.17 and 9.18 for the east and north vectors respectively. It can be seen on these two plots that any difference between the original and WTI-removed data is very small in most cases. For the east currents on figure 9.17 the measurements are in worse agreement with that of the ADCP after WTI removal and the rms difference is made slightly worse, see table 9.7. The north currents on figure 9.18 show measurements to be closer to those of the ADCP but still large unrealistic values remain and the rms difference remains large.

9.8 Wave measurements

Having assessed how the WTI removal has influenced the current measurements of the HF radar the effect on wave measurements is now considered by comparison

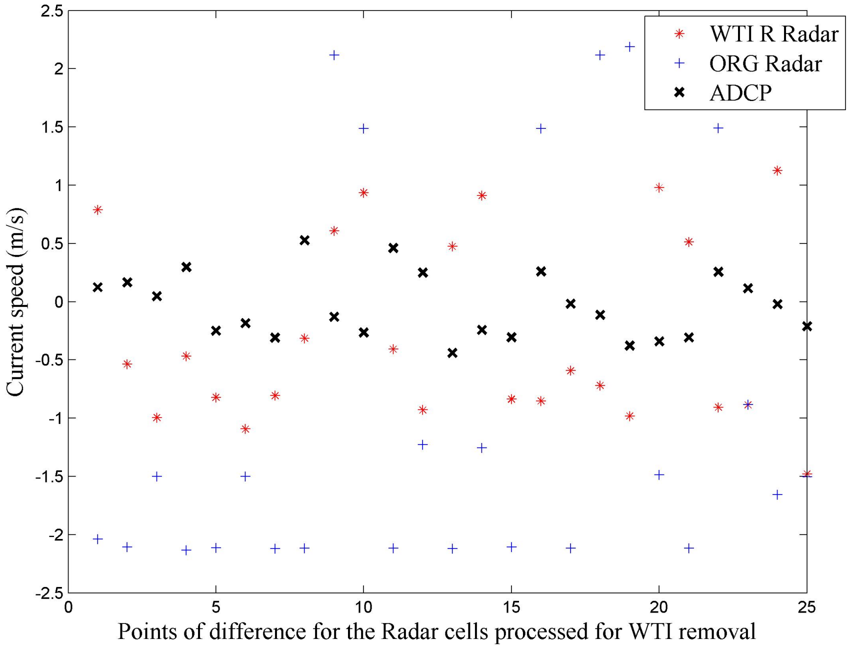

Figure 9.15: The original and WTI-removed Llanddulas radial currents when differences in their time series occurred. The ADCP current value in the look direction of the radar at the same time is shown as a black cross.

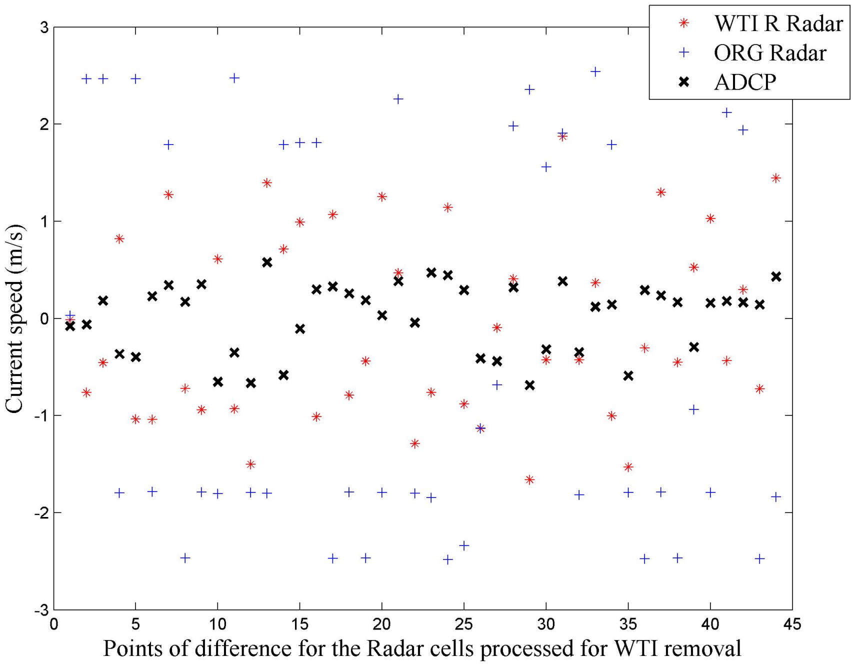

Figure 9.16: The original and WTI-removed Formby radial currents when differences in their time series occurred. The ADCP current value in the look direction of the radar at the same time is shown as a black cross.

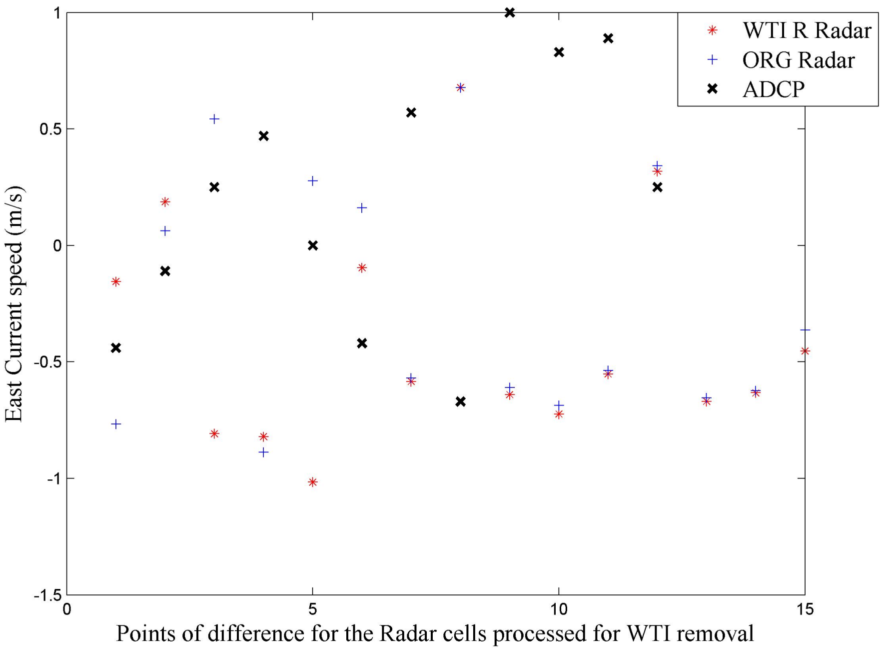

Figure 9.17: The original and WTI-removed east vector currents when differences in their time series occurred. The ADCP current value in the east direction of the radar at the same time is shown as a black cross.

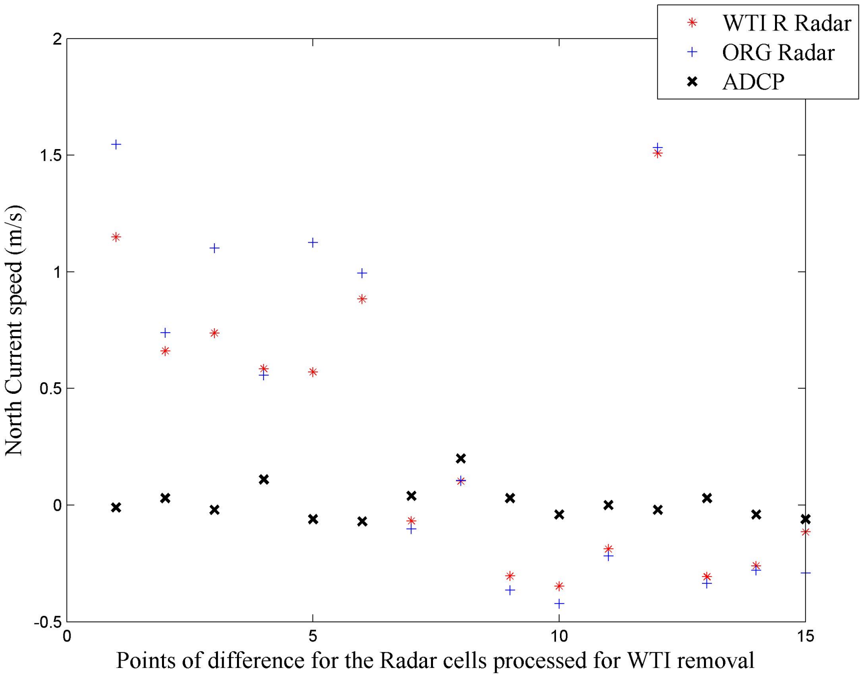

Figure 9.18: The original and WTI-removed north vector currents when differences in their time series occurred. The ADCP current value in the north direction of the radar at the same time is shown as a black cross.

with local Waverider buoy measurements located at radar cell 234. Cell 234 is not a wind farm location but it has been processed for WTI as a control and as a way of assessing the effects on data of false positive WTI identification.

As established at the start of this chapter WTI is greatest during low winds and low sea state conditions. This makes filtering for Hs $>$ 1 m, shown by Robinson *et al.* [2013] to greatly improve radar and buoy Hs correlation, inappropriate for the initial investigation of WTI effects.

Figure 9.19 shows the buoy Hs time series for the month of April 2010. It can be seen that Hs measurements are less than one metre for the majority of the time during this period and that maximum Hs measurements are, as expected, less than five metres. Any correlations will therefore appear naturally worse, not just due to WTI and spikes in the radar time series but also because of the low sea state conditions.

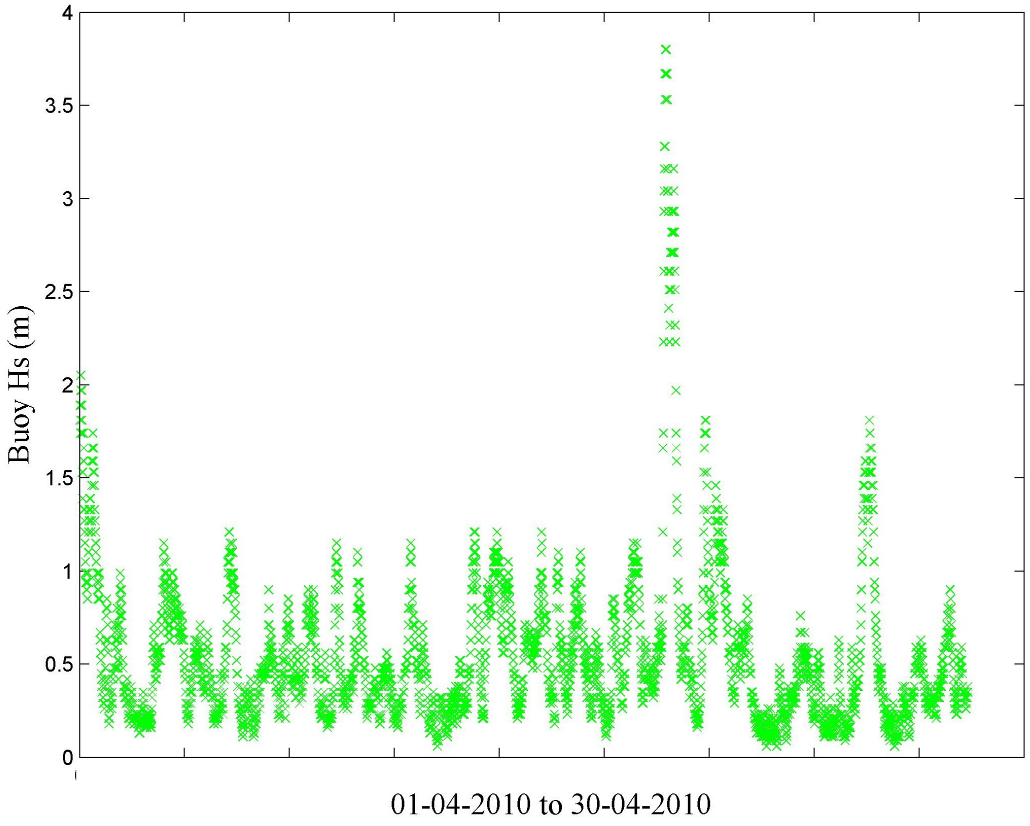

Figure 9.19: The Hs time series measured by the Waverider buoy in Liverpool Bay.

First considered are the radial measurements. Each individual Doppler spectrum produces two estimates of Hs but an individual radar does not make an estimate of wave direction. One assumes the wave is travelling parallel to the look direction of the radar and the other assumes the waves are travelling perpendicular to it. This again causes a situational difference between the Llanddulas and Formby radar measurements with wind-waves moving primarily north-eastwards in high sea states and either eastwards or westwards generally.

The number of differences between original and WTI-removed Hs measurements is more significant than for currents, with between 70% and 90% of data points altered. Availability of Hs measurements from radial data was however much less, at around 15% to 25% of Doppler spectra recorded both before and after processing for WTI.

During the month of April 2010 the buoy data recorded a maximum Hs of 3.8 m and very few measurements greater than 1.5 m. At the RFWF location, radar radial data for this period regularly exceeds the maximum buoy Hs and contains many spurious data spikes compared with the buoy data.

A significant amount of Hs values are above 5 m when differences between original and WTI-removed Hs values have occurred. The WTI removal process is therefore identifying spikes in the radar Hs time series. The buoy Hs measurements for these occurrences are however almost all below 1 m, whereas for the time period as a whole only 60% were below 1 m. This again confirms that WTI within the Doppler spectra is more prevalent in low sea states.

The changes in Hs values after WTI removal are very small in most cases and although generally closer to the buoy measurements they are not any more physically realistic. Correlations between the radar radial Hs data and buoy data are very poor and, as the data in table 9.8 show, rms differences are large. WTI removal has reduced this by a minimum of 10 cm and a maximum of 40 cm and correlations were altered by less than a hundredth of their original values. Improvements in the radial perpendicular and parallel Hs measurements from both radars were negligible and agreement remained poor.

Over 88% of full inversion wave measurements were altered by WTI removal. Figure 9.20 a) shows the Hs time series for cell 158 co located with the RFWF and figure 9.20 b) shows that of cell 234 co-located with the Waverider buoy. Hs measurements are plotted for the radar original and WTI-removed time series and that of the buoy only when simultaneous measurements existed for all three. This results in a more defined buoy and radar time series on figure 9.20 a) for cell 158 but the peaks, troughs and general shape is still evident on figure 9.20 b).

Measurement Detail	Difference Number	rmsd (m) ORG-Buoy	rmsd (m) WTI-removed-Buoy
Formby Radial Per	962	9.7	9.3
Formby Radial Par	927	3.0	2.9
Llanddulas Radial Per	924	7.5	7.1
Llanddulas Radial Per	893	2.4	2.3
Full inversion	250	2.88	2.81

Table 9.8: Summary of original (ORG) and WIT removed Hs root mean square differences, rmsd, compared with buoy data.

It is clear from figure 9.20 that the radar is best able to accurately make Hs measurements at peaks in the buoy data, and therefore maxima in the sea state. It is also instantly visible that there are more large amplitude spikes at the wind farm location, figure 9.20 a), compared with a cell not at the wind farm location, figure 9.20 b). It can also be seen that the majority of the very large spikes on figure 9.20 a) occur when the buoy is measuring Hs less than 0.5 m, as discussed in the initial investigation into the Doppler spectra (table 9.3 and figures 9.3 and 9.4).

Figure 9.21 shows a shorter time series for cell 156 when the sea state and buoy Hs values drop to very low levels (< 0.5 m). As was concluded during initial inspections of the Doppler spectra of cells surrounding the RFWF, at cell 156 the influence and amplitude of the WTI is reduced compared to cell 158. Overestimation of Hs measurements during low sea states is also much less two cells away from the RFWF compared with those at the co-located cells. This can be seen in the reduced amplitude of Hs spikes during the second week of April on figure 9.21 compared with 9.20 a). Comparing figures 9.20 and 9.21, again it can be seen that for large sections of low sea state conditions, as measured by the buoy, large spikes from the radar data are reduced but not removed. WTI-removed Hs values are smaller but no better reflect the buoy data.

Table 9.9 shows the statistics from the original and WTI-removed Hs time series compared to that of the buoys. In this it can be seen that the correlations are poor between the radar and buoy Hs both before and after WTI removal and no overall statistical improvement has been achieved. As found for the case of the radial data, rms differences are smaller but by very small amounts, with no better accuracy from the radar measurements.

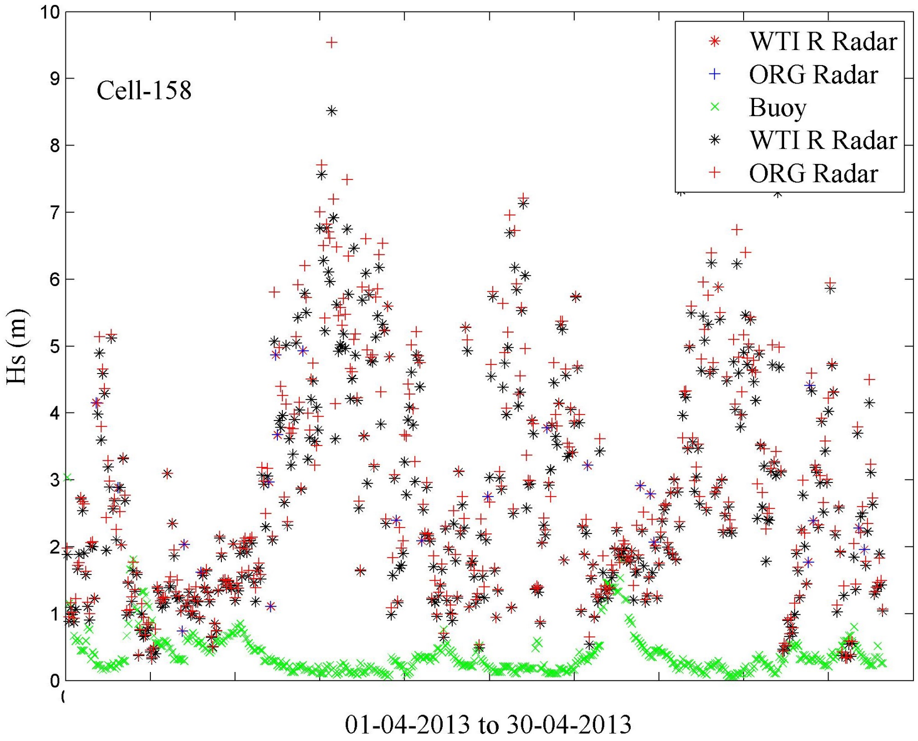

a) Cell 158

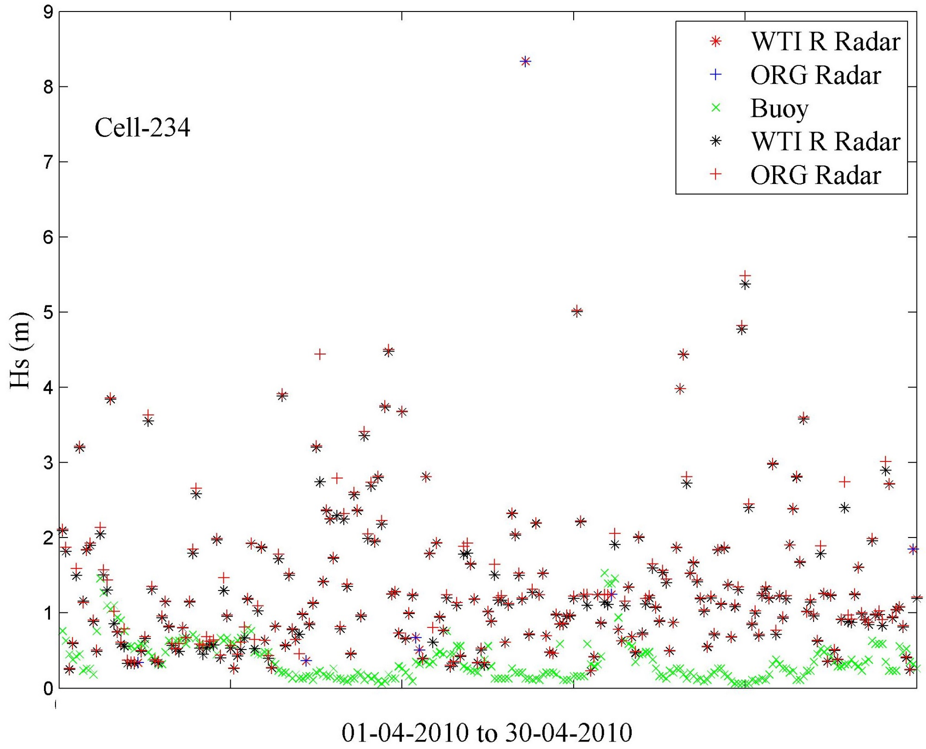

b) cell 234

Figure 9.20: The original and WTI-removed full inversion Hs time series for cells a) 158 and b)234 and the buoy Hs time series. Original and WTI-removed data points that are no different are shown in blue and red, respectively. Measurements where there was a difference are shown as a red cross for the original data and a black star for the WTI-removed data.

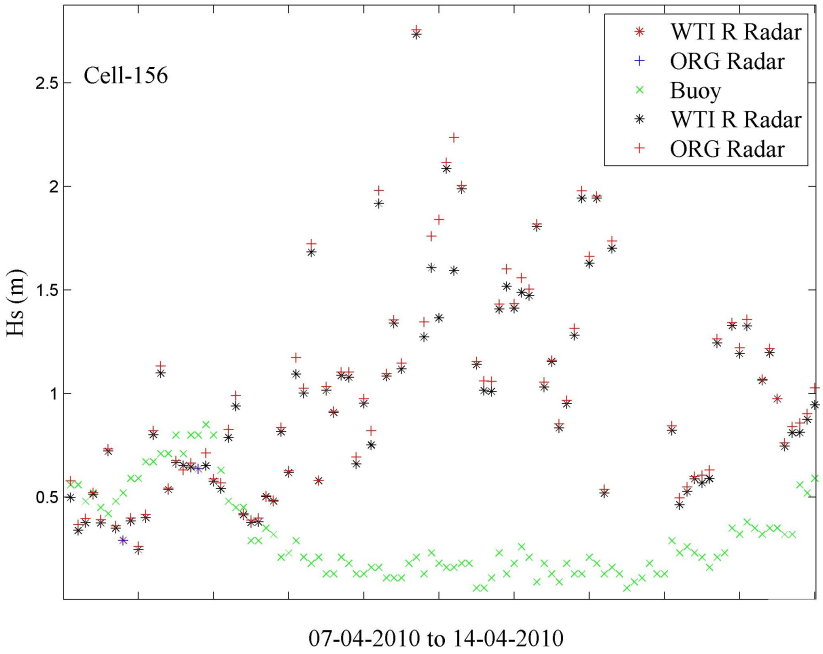

Figure 9.21: The original and WTI-removed full inversion Hs time series for cell 156 and the buoy Hs time series. Original and WTI-removed data points that are no different are shown in blue and red, respectively. Measurements where there was a difference are shown as a red cross for the original data and a black star for the WTI-removed data.

Cell	r ORG	r WTI	rmsd ORG (m)	rmsd WTI (m)
116	−0.20	−0.22	1.49	1.41
136	−0.31	−0.33	1.54	1.50
137	−0.48	−0.50	3.01	2.89
138	−0.48	−0.49	3.54	3.38
156	−0.11	−0.13	1.28	1.21
157	−0.40	−0.40	2.46	2.36
158	−0.50	−0.50	3.14	3.00
176	−0.11	−0.12	1.09	1.06
177	−0.29	−0.30	2.00	1.95
178	−0.37	−0.37	2.31	2.25
196	−0.34	−0.35	1.80	1.78
234	−0.18	−0.19	1.53	1.49

Table 9.9: Summary of original and WIT removed Hs measurements compared with all buoy data. Correlation, r, root mean square error, rmsd, Original radar data, ORG, wind turbine interference removed data, WTI.

Robinson *et al.* [2013] also found poor correlations and large rms differences between radar and buoy data in Liverpool bay. The three month data period used by Robinson *et al.* [2013] in 2010 includes the month's data investigated here but all the wave height statistics given in table 8.3 are significantly different to those in table 9.9. For example Robinson *et al.* [2013] report a correlation of 0.49 at cell 157, a reasonable value for Liverpool bay, yet the correlation calculated here is -0.4 for cell 157.

To investigate these differences, additional filtering was applied to the April 2010 time series used for the original and WTI-removed Hs comparison with buoy data. The radar and buoy Hs time series were filtered selecting simultaneous measurements only when the buoy was measuring a Hs value above 1 m. On less than 50 occurrences a buoy measurement greater than 1 m, original radar data and WTI-removed radar data occurred simultaneously, so data sets for comparison are relatively small. The consecutive measurement spike filter applied by Robinson *et al.* [2013] was not used in this instance.

Figure 9.22 shows all measurement occurrences for these large Hs measurements. The maximum Hs of the radar data is reduced to just under 4 m from close to 10 m and radar and buoy measurements are much closer together. This shows that data spikes in radar measurements can be reduced simply by filtering for high sea states. Again it can be seen that only small differences have been made to the original radar Hs time series from the WTI removal.

The correlations and rms differences given in table 9.10 are much improved compared with the all sea state values in table 9.9 and better reflect those of Robinson *et al.* [2013]. Cells further away from the location of the wind turbines, although showing WTI in their Doppler spectra, when filtered for good sea state conditions produce very reasonable correlations with buoy data. It can be seen that at a distance of two cells away from the wind turbines, cells 116, 136, 156, 176 and 196, the original Hs data series correlates well with buoy data and processing for WTI only results in small changes to correlation and rms difference. Cells in closer proximity to the wind turbines, 137, 157, and 177, as well as cells co-located with the wind turbines, 138 and 158, have low Hs correlations considering they have been filtered for good sea states. The correlations are also lower than those published by Robinson *et al.* [2013], given in table 8.4. Robinson *et al.* [2013] did however remove data where differences between consecutive measurements suggests a data spike. This would have removed at least some of the spurious data points caused by WTI but was not applied in this instance to allow the effect of WTI removal and

Cell	r ORG	r WTI	rmsd ORG (m)	rmsd WTI (m)
116	0.70	0.69	0.60	0.60
136	0.78	0.74	0.34	0.39
137	0.43	0.44	0.45	0.42
138	0.59	0.54	0.63	0.60
156	0.87	0.88	0.47	0.54
157	0.38	0.44	0.53	0.47
158	0.34	0.33	0.47	0.48
176	0.90	0.96	0.30	0.28
177	0.59	0.53	0.47	0.52
178	0.40	0.46	0.54	0.57
196	0.83	0.83	0.22	0.25
234 spike	-0.32	-0.31	1.00	0.99
234 no spike	0.42	0.46	0.38	0.34

Table 9.10: Original and WIT-removed Hs measurements compared with buoy data after filtering for buoy measurements > 1 m. Correlation, r, root mean square error, rmsd, Original radar data, ORG, wind turbine interference removed data, WTI.

filtering to be investigated.

The high sea state Hs data for cell 234 and the buoy Hs measurements are generally very close together. The correlation and rms difference values, given in table 9.10, were however initially very poor. Discounting the radar Hs spikes of 4 m, the correlations and rms differences are greatly improved. Omitting just one data point results in the correlation changing from -0.32 with the data spike to 0.42 without it. This highlights that the data sets used are perhaps too small for reliable results.

9.9 Summary

Starting with the exercise of modelling the RCS, ideas were formulated regarding how the signal backscatter would be altered in the presence of a wind turbine. Maximum RCS estimates are confirmed, as expected, to be proportional to the size of the wind turbines and returns have more energy if closer to the radar. The variation of RCS with aspect angle showed that, as the blades rotated, peak values could be expected every 60^o. Using the wind turbine manufacturers' nominal operating speed, the frequency spacing of the RCS peaks was calculated to be 0.675 Hz. The presence of a signal modulation with this frequency spacing was shown to exist in the Doppler spectra from cells co-located with the RFWF. An inspection of cells close to the wind farm showed this modulation to be sufficiently reduced from two radar cells away. The repetitive and consistent presence of this frequency modulation was confirmed by averaging a months' worth of Doppler spectra from the wind farm location.

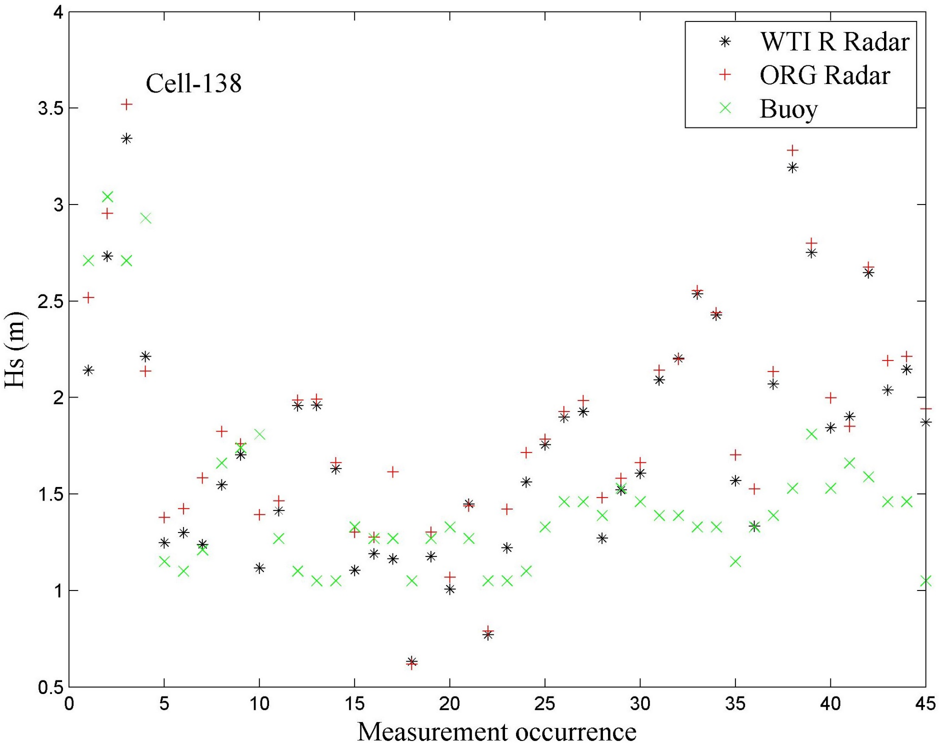

a) Cell 138

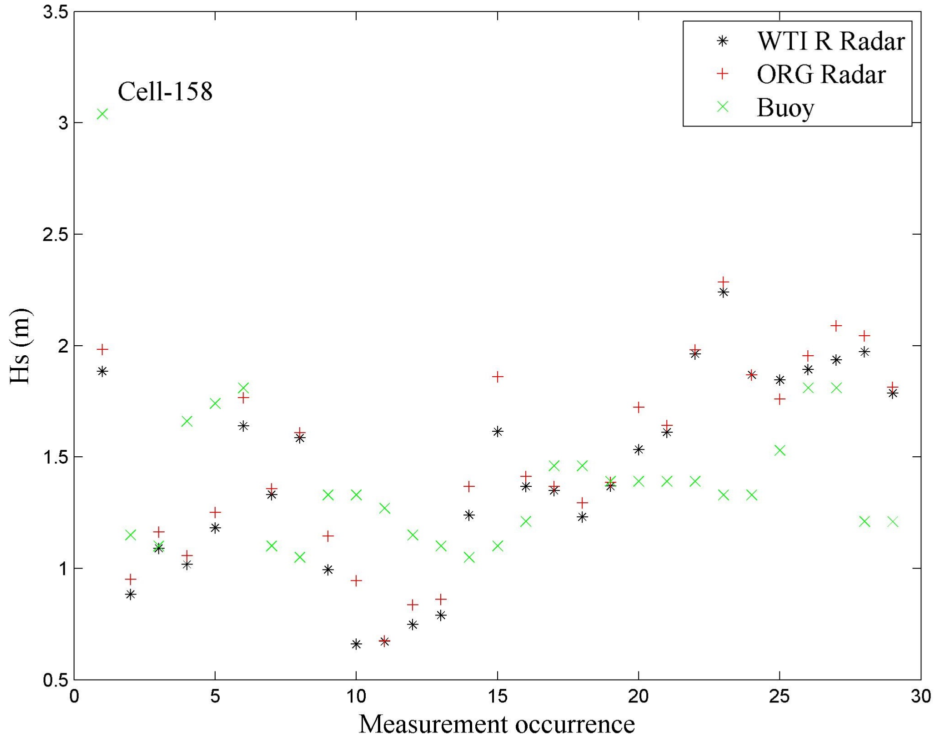

b) cell 158

Figure 9.22: Original and WTI-removed full inversion Hs time series for cells a) 138 and b)158 and the buoy Hs time series for buoy measurements > 1 m. Original and WTI-removed data points that are no different are shown in blue and red, respectively. Measurements where there was a difference are shown as a red cross for the original data and a black star for the WTI-removed data.

The movement of the frequency peaks with alternative radar chirp lengths was predicted. The Formby and Llanddulas radars were then configured to make additional measurements with the alternative chirp lengths. The resulting Doppler spectra of differing frequency range were able to confirm that frequency modulation outside the range of the Doppler spectra would propagate to the adjacent measurement cell. The frequency of modulation peaks caused by the wind turbines could then be identified and the associated energy removed from the Doppler spectra.

Using a three month period, which included the month analysed here, Robinson *et al.* [2013] reported current availability of no less than 93% for any cell. The availability of data in this shorter month analysis was then reasonably close for radial data but much less than expected for vector currents. Wave data availability was again similar to that of Robinson *et al.* [2013]. Variations in measurement values and data availability were evident when compared to published values from NOCL. Although the same Doppler spectra were processed and Seaview Sensing software used for both, there will have been differences in the configuration files used as well as the quality control parameters due to updates of the NOCL software not applied to the University of Sheffield version. A valid assessment of the WTI removal can still however be made as both original and WTI-removed Doppler spectra were processed using identical methods at The University of Sheffield.

Spatial current variability at the RFWF is very small and correlations remain high. Current magnitudes are also predictable due to the tidal dominance in the region. Wave parameter values are however in very poor agreement with buoy data. Because of the different amounts of influence on the first and second-order measurements when removing WTI from the Doppler spectra greater consideration was given to mitigating WTI influencing second-order measurements. This is reflected in the number of data points identified as WTI spikes in the current and Hs time series. Comparing original and WTI-removed current and wave data, the method used is not identifying current measurements influenced by WTI in the majority of cases. It is the opposite for Hs measurements where most of the data spikes in the time series are identified. Fewer data spikes also exist within the current time series compared to that of the Hs. It has been suggested by Robinson *et al.* [2013] that wave measurements are more sensitive to WTI than current measurements. It is possible that this is specific to Liverpool Bay due to the strong currents and low sea states, however the measurement techniques will also be contributing to this effect.

The idea that the worst effects of WTI are evident when current values are small has been discussed by Robinson *et al.* [2013] and in chapter 8, figure 8.4. This is again supported here and most current spikes correspond to small ADCP current values. Some adjustments to radial current measurements from the WTI removal have improved the data and the resulting current measurement is much closer to the values of the in situ ADCP. As discussed, some harmonics of the WTI modulation are close enough to the expected Bragg scattering frequency that it can be wrongly selected as the peak from which to measure currents. Where WTI removal is successful, in this case it results in a dramatic improvement in the current value as seen on figure 9.14 b). This is not typical though, as when comparing only measurements that were different after WTI removal for all cells processed, the radial current rms differences for Llanddulas and Formby are both large before as well as after. It is also clear that the majority of current measurements, both radial and vector, that are characteristic of those perturbed by WTI are not changed in any way by the mitigation process trialled.

As found by Robinson *et al.* [2013], the Llanddulas radial and north current vectors are unreliable measurements at the wind farm location. The very strong dominant Formby radial and east current vector however seems reasonably unaffected and when both are combined current amplitudes and phase match those of the ADCP very well. Mitigation at the current measurement stage is therefore not going to statistically improve data series, which are already highly correlated with small rms difference values. For currents the simplicity and effectiveness of filtering compared to identifying and removing WTI is very clear.

There is an increase in the number of wave measurements at the RFWF site. One possible explanation is that due to additional energy in the second order Doppler spectra region from WTI, the SNR will be greater resulting in more measurements passing the SNR thresholds. The integration, for Hs measurements, of the second-order Doppler spectra is over a greater frequency range than for currents. This results in more energy being removed from the second-order region and a lower sea state measurement is made than without WTI mitigation. With the sea state reduced, the resulting Hs measurement will always be smaller. In the majority of cases the radar Hs is however greater than that of the buoy and therefore the WTI removal will, by default, improve upon the radar measurement. Overestimation of Hs is therefore statistically reduced but the WTI-removed time series no better reflects that of the buoy than the original.

With the introduction of additional quality control measures the improvements in radar Hs measurements can be significant. In this case a simple high pass filter set at one metre is seen to improve correlations at all sites investigated. Cell 176 for example had a correlation with buoy data of -0.11 which was changed to -0.12 after WTI mitigation. After filtering however it improved to a value of 0.90. Removing unrealistic data spikes and changes between consecutive measurements that could not physically happen, as done by Robinson *et al.* [2013], may also improve these figures further and remove data perturbed by WTI from the data time series but was not done at this time to allow the effects of WTI removal and filters to be assessed.

Although there was no wind turbine present at cell 234, when the Doppler spectra for this cell was put through the WTI removal programme some data was changed. The number of occurrences of WTI identification was however much less than for cells where the WTI was actually present and in practice WTI removal would only be run on cells where WTI is expected.

What has been attempted here is a very simplistic model of how the modulation caused by one wind turbine operating at nominal speed could be identified within a Doppler spectra. The removal process is based around the shape of how RCS values, and therefore signal returns, vary with aspect angle. After WTI peak identification the energy at the associated frequencies is reduced to a local mean for the peak spectral width, estimated by that of the RCS peak. When the frequency identified is close to the Bragg frequency only two frequency bins are reduced in energy to make the energy removed from the first-order region proportional to that removed from the second. This mitigation approach appears however not to remove enough energy from either spectral region. It is also possible that the combined effect of multiple turbines is not being dealt with. Although the method used allows for the identification of multiple wind turbines operating at different frequencies it is possible multiple operating frequencies are not being mitigated during processing. If a similar rotational frequency existed from two wind turbines each frequency could have a large amplitude with subsequent harmonics but only one will be identified as the local peak if they were closer in frequency than ten spectral bins, thus only one would be removed. Multiple wind turbines all operating at very similar frequencies or slow rotations could also act to spread the WTI peaks within the Doppler spectra and the width of the peak removed may not be enough, as evident in before and after WTI removal Doppler spectra.

The processes developed are based on high winds and sea states where the turbine blades will be rotating at their nominal speed. This frequency and its subsequent harmonics are easily identifiable. These peaks tend to be over smaller spectral widths and the 5^{th} harmonic (for 0.26 s chirp length) will be small in amplitude.

The radar performs best in these conditions at the RFWF site, not just because of the high sea state but because it is only the fundamental and 5^{th} harmonic of the modulation that will fall in the region for measuring currents and waves. The fact that WTI is more prevalent during low sea states is not just caused by the poor measurement conditions, but by increased modulations in the first and second-order spectral regions. We know winds in Liverpool Bay are generally low however the investigation has so far has failed to account for the slow rotation of the wind turbines. At their maximum speed, the blades will be rotating at 13.5 rpm, corresponding to the manufacturers' maximum blade tip speed of 73 m/s. If the manufacturers' minimum blade tip speed, 28 m/s, is then considered, the blades will be turning at only 5.2 rpm. This minimum rotational speed would modulate the Doppler spectra at a fundamental frequency of 0.258 Hz. This would result in 7 harmonics being present in one Doppler spectrum, each with large but diminishing amplitude. It would also mean that potentially 4 WTI modulation frequencies could be present in the current and wave measurement regions. This could explain the shape of 9.3 f) and 9.4 f) with the low wind speeds measured at Hilbre. The slower rotation would also spread the high amplitude returns, moving away from the sharp peaks seen during high winds.

It is clear a more complex characterisation of WTI within the Doppler spectra is required for peak identification. This must account for multiple turbines operating at almost the same frequency as well as the slow rotation of the blades. A variable option for the frequency width mitigated will further reduce the amplitudes of frequencies integrated for the second order Doppler spectra but this would only be useful in addressing overestimation of the sea state. Where WTI is suspected and identified but results in no difference to current measurements, a different approach to the amplitude adjustment is required. In the method investigated there is no tapering to energy removal around the WTI peak. Fitting a Gaussian curve to the WTI peak to determine the amplitude attributed to WTI at frequencies surrounding it would more realistically reflect the RCS shape and again remove more energy due to WTI modulation. This and the issue of peak identification in low winds must be addressed to improve data provision at the location of wind turbines.

Chapter 10

Conclusions

Over the extensive 7 year HF radar deployment in Liverpool Bay, NOCL have maintained a very high level of data availability and constantly improved upon the operational accuracy of measurements produced by the radar. Using an almost continuous radar time series and very comprehensive buoy and ADCP series, the ability of the radar to measure currents and waves has been assessed at various stages of its deployment.

Where operational conditions are within guidelines, the HF radar is producing current measurements that are highly correlated with measurements from ADCP during both short and long time periods. When environmental conditions are favourable, reliable and accurate Hs measurements have been obtained and, with some additional data filtering, excellent correlations with buoy data are achieved.

The radar performance has been established by investigating a few simple operational questions, including: How much data was the radar producing? What amount of data passes the first-order thresholding? What percentage passes the second? How did these figures differ over the radar footprint? At the centre of each of these questions is the fundamental thread of determining the Doppler spectra noise level and establishing how the noise varies in each cell, day and night, at all transmitting frequencies.

Average Llanddulas noise is 6 dB higher than Formby. Separation of Doppler spectra into day and night has shown approximately 2 dB of this is caused by the close proximity of Llanddulas to a main A road (A55) and train track. For the core group of measurement cells, current radials were available for no less than 85% and no more than 99% of the time. Wave measurement availability is however highly variable over the radar footprint, from 3% to 93%. It is also highly dependent on the sea state conditions over the period being investigated. Specific measurement periods are shown to be more favourable than others. The 13.465 MHz operating frequency (20 minutes past the hour) gave a higher average buoy-radar Hs correlation. This period of time is prior to an increased averaging time being introduced at 20 past the hour, from which improved wave estimates would be expected.

The initial noise investigation clearly shows that introducing a wind turbine into the radar measurement footprint significantly elevates noise levels at the co-located measurement cell as well as those adjacent to it. This should act to reduce the first and second order SNR. However radial data availability remained high for cells co-located with the wind farm. The availability of current vectors is also not affected by WTI. More energy is added to the first and second-order regions of the Doppler spectra used for measurements as well as the elavated noise levels. In the presence of the wind farm more Doppler spectra are therefore seen to pass the SNR criteria for wave measurements. This in turn causes the number of wave measurements made at the co-located cells to remain relatively high.

Several parameters were investigated as a means of quality control for the radar. One technique used was Least Squared Harmonic Analysis for extracting tidal amplitude and phase. The results were compared between ADCP and HF radar using a two year current time series. The results, also presented by Robinson *et al.* [2011], show the ten tidal constituents used account for over 90% of the east observed current, with at least a 77% contribution from the M_2 component. The north current component is found to have a much smaller tidal element with an average of 40% of the observed current attributed to it. The M_2 tidal frequency is still however the largest component. Agreement between the ADCP and HF radar generated M_2 tidal ellipses is consistent with expected values for such a tidally dominated region and are within 3^o phase and 2 cm/s amplitude of each other.

Having established a consistent record for data provision and excellent agreement between ADCP and HF radar tidal frequency amplitudes and ellipses, the correlation of radar measurements with ADCP was investigated spatially. Radial current measurements, compared with those of the ADCP in the look direction of the radar, show similar results to those of the east and north vector currents from the ADCP. The Llanddulas radial has a large variation over the radar footprint but Formby is much more uniform due to the strong M_2 tidal constituent, with even a 0.89 correlation at NHWF. HF radar data from the NHWF, cells 198 and 217, was expected to be in worse agreement with ADCP. Statistical differences are however shown to be more consistent with cells of similar cross-over angles. The introduction of an error of magnitude 15 cm/s is calculated to be attributed to this whereas for cells within the recommended range of 60^o this error is just 3 cm/s.

It is shown that to capture surface effects from the ADCP, a bin as close to the surface as possible, but that doesn't contain sidelobe contamination, should be used. In Liverpool Bay it is shown that the 2 m or 3 m below surface time series is preferable. The best ADCP surface current time series for comparison with HF radar will however be system-specific and may change if the operating frequencies were different. For example the 5 MHz, 60 m transmit frequency and wavelength utilised by Liu *et al.* [2010] will depth average to almost 3 m and they were able to obtain good correlations between ADCP and HF radar using a 4 m below surface bin.

The ability of HF radar in Liverpool Bay to deliver current measurements with high agreement to those of ADCPs is excellent. Correlations are amongst the highest in the field with values > 0.75 and < 0.96. The large cross-over angle at cells 198 and 217 masked any effect from the NHWF on the current data. The construction of the RFWF therefore gave the opportunity for a before and after study and also eliminated 80% of cross-over angle error due to its location. Agreement of the Formby radial current component and ADCP A is found again to be excellent with correlations of approximately 0.9 during the before and after periods. The east current vector also showed slightly improved statistical agreement with ADCP A after installation. This was not the case for the Llanddulas radial or north current component, both of which showed reduced statistical agreement after the installation. A combination of factors could be contributing to these differences. Being short time series, each is more sensitive to data spikes and with the smaller current amplitudes from Llanddulas it will be even more sensitive than Formby. With predominant westerly winds the wind turbines will present a much larger RCS to Llanddulas than Formby and amplitudes of modulated frequencies will be larger. RFWF is also much closer to Llanddulas than Formby, making signal returns stronger. The very dominant east-west tidal current results in any element of wind driven surface current being a small proportion of the current measured from Formby and a larger proportion from Llanddulas. When Llanddulas and Formby radials are combined for vector magnitude and phase and compared with those of the ADCP the wind farm location showed slightly improved correlation, from 0.92 to 0.93, after the RFWF installation. The small contribution from the most affected, northerly, current component is therefore masked.

In chapter 8 and 9 it is shown that additional data filtering and quality control can improve agreement between HF radar and buoy Hs measurements. As with current vectors, at first glance it appears the introduction of the RFWF has improved Hs measurements, and for the data sets with additional filtering correlations after are greater than before. This, however, is the case when looking at cells individually. When spatial plots of the correlations were viewed the degradation of the Hs measurement at the RFWF location was much clearer (see figure 8.6).

Visual evidence of WTI in individual Doppler spectra is strong. The frequency spacing of high amplitude peaks suspected of being an imposed modulation on the backscatter signal have been shown to match the blade rotation for a nominal operating frequency. Any frequencies larger than those of the individual Doppler cell are shown to propagate into the adjacent cell. This allowed the frequency of modulation spikes from adjacent cells to be predicted if the assumption is made that they are at the same operating frequency. This was again found to be the case with large Doppler spectra amplitudes at the expected frequencies. Confirmation that this was indeed happening was obtained by extending the sweep frequency time during data collection. This gave a larger Doppler frequency range allowing the predicted 3^{rd} harmonics to be directly observed and all subsequent harmonics shifted in frequency space accordingly. Where WTI peaks were identified in the Doppler spectra, the amplitudes at these frequencies were reduced. The Doppler spectra were then reprocessed for current and wave measurements. For the few cases where the mitigation worked for current radials it has done so exceptionally well. The evidence suggests it is only effective in certain sea state and WTI conditions and not robust at removing WTI in the Doppler spectra. Mitigation against wind turbine effects in current measurements, even if 100% successful, would result in only a very small statistical improvement.

The evidence shows that the initial approach to investigating and mitigating WTI is not yielding worthwhile improvements in data and is too simplistic in its approach. Changes to the Hs estimate after WTI processing have been minor and agreement with buoy data remained poor. The WTI mitigation tested is far too simplistic in the way it identifies and reduces the energy at frequencies attributed to WTI. The peak identification and removal is designed around the nominal operating frequency of the wind turbine. In this instance modulation frequencies and the subsequent harmonics are moved away from the Doppler spectra region for current and wave measurement. The identification of WTI with smaller modulating frequencies falling within the region for measuring currents and waves poses a much more difficult problem. Better characterisation of the WTI within the Doppler spectra is required that is adaptive to multiple modulation frequencies. If this lower frequency of operation can be characterised more energy attributed to the WTI could be removed from the Doppler spectra and prevent overestimation of the sea state parameters. The possibility of WTI mitigation in the range-resolved Doppler spectra before beamforming may also prove to be more fruitful, as has been the case for weather radar [Nai *et al.*, 2011]. Future work is essential on the mitigation of WTI from HF radar Doppler spectra to maximise data availability, measurement accuracy and scientific and commercial applications.

10.1 Summary

Current measurements at the wind farm locations agree well with those of ADCP. Correlations between HF radar and ADCP current data at the RFWF remains within typical ranges reported by similar studies but are low for values reported in Liverpool Bay. The rms difference is towards the larger of reported values but is a similar percentage of the mean current magnitude. With such strong, well mixed tidal currents, as shown to exist in Liverpool Bay, taking the current reading from the nearest non-wind farm radar cell would produce a very good current estimate quickly. In regions where there is more spatial variability in currents this may not however be appropriate.

Wave measurements are more sensitive to WTI. Persistent low sea states in Liverpool Bay greatly restrict the quality of the wave measurement made with HF radar even at non-wind farm locations. Post-processing quality control parameters, such as high or low pass filters and consecutive measurement difference restrictions, are therefore recommended to improve the measurement agreement between the HF radar and in situ measurement devices for both currents and, more significantly, waves.

Although the WTI mitigation trialled here has been ineffective, it is the case that where the majority of Hs measurements are being identified as WTI no reliable wave measurement would have been possible due to environmental conditions. This is because during low sea states winds are generally low as well and WTI is much more prevalent. WTI is less evident in high sea states as modulating frequencies are minimised in the Doppler spectral region used for currents and waves. Of course operationally, for sea-based industries, it is more important to get high sea state measurements correct than low due to the higher risk to human life, vessel damage and navigational difficulties.

The production of reliable and accurate HF radar ocean current and wave measurements can be maximised through data filtering. A responsibility then falls to the user of the data to impose physically realistic conditions and to be aware of the limitations in the measurement system they are using. A multi-instrument combined measurement assessment will always produce the best estimate of the true value, hence the importance of continuous real-time provision for operational decision making.

10.2 Recommendations

HF radar measurements of ocean currents and waves were found to be within expected standards for uniform currents and high sea states. However, wave measurements are poor in low winds and for significant wave heights less than 1 m. Before HF radar data is presented for commercial use, post processing to provide the best HF radar estimate of the sea state parameters must be carried out. Additional quality control measures can clean data time series of the majority of WTI and maximise the commercial potential of HF radar. Appropriate methods include:

- Low pass current and Hs filtering.
- High pass Hs filtering for wave measurements.
- Maximum rates of change between consecutive current and significant wave height measurements.
- Presenting current data as a combined vector and not as east and north components.
- Interpolation between measurement cells for waves and currents.

These measures can be implemented at any point should a wind farm be constructed during a HF radar deployment. No alterations are required to the radar installation or processing software. With only the output measurements from the HF radar required, these steps are not radar specific and could be implemented on all HF radar systems. Data for commercial applications would be improved by requiring less scientific interpretation by the user. For WERA radar systems pre-transmit scanning and selecting the optimal sweep frequency time are also options.

Pre-transmit scanning will minimise noise in the Doppler spectra, maximise wave data availability and improve Hs agreement between HF radar and buoy. Operating the radar with a sweep frequency time that relocates any modulation away from the Bragg frequency will reduce error in the current measurement. Sweep frequency time can also be selected so that it minimises the number of modulation peaks within the Doppler spectra region utilised for current and wave measurements. This will however only be effective in high winds with WTI at the nominal operating frequency and with minimal frequency spread.

For a brand new radar system, selective placement of the HF radar footprint can optimise the scientific and commercial use of data. In choosing a site for HF radar the relative position of the antenna to the wind farm should be considered. If the antenna array can be placed so that the look direction to the wind farm is greater than 60^o off boresight it will be outside the operational range of the HF radar.

Appendix A

Table 1: A brief selection of comparative studies between HF radar and in situ measurements.

Reference	Radar	Location	Frequency (MHz)	Mooring Type	Measurement Details	r	RMSD (cm/s)		Mean current speed (cm/s) (direction deg)
Fernandez and Paduan (1996) Monterey Bay	OSCR	S.C	25.4	ADCP (bin centred at 9 m depth)	Radial Currents	0.72	5.7		
		M.L				0.58	6.4		
	CODAR	S.C	12.2		u	0.4	8.5		
		P.P	13.7		v	0.66	9.5		
Paduan and Rosenfeld (1996) Monterey Bay	CODAR	S.C	12.5	ADCP (bin centred at 9 m depth)	Vector Currents (3 radial current derived)	u 0.58	6.2		20(E)
		P.P	12.5			v 0.83	10.8		30(E)
		M.L	25.4	Ship mounted ADCP (bin centred at 12 m depth)		u −0.25	13.2		20(E)
						v 0.45	8.4		30(E)
Graber et al (1997) Cape Hatters North Carolina	OSCR	C.H.	25.4		OSCR vector currents		speed	θ(deg)	B1 18.6 ± 10.7
							-	-	B2 39.8 ± 23.5
							-	-	DE 34.9 ± 18.8
							-	-	-
		Station B1		current meter 1 (5m depth)		-	20.5	41	11.5 ± 8.2
		Station B2		current meter 1 (5m depth)		-	18.2	46	29.5 ± 16.7
		Station DE		current meter 3 (5m depth)		-	20.1	51	28.9 ± 17.8
Kelly at al. (2003) West Florida Shelf	CODAR	W.F.S.	25	ADCP					ADCP / Radar
					Along-shelf	0.92			-7 ± 12 / -9.8 ± 17
					Cross-shelf	0.62			-2 ± 5 / -0.8 ± 5
					Dual Radar, Complex current magnitude (phase (deg))	0.87(−5.7)			

Table 1 continued

Reference	Radar	Location	Frequency (MHz)	Mooring Type	Measurement Details	r	RMSD (cm/s)	Mean current speed (cm/s) (direction deg)
Kaplan at al. (2005) Bodega Bay	CODAR	B.M.L. P.R.	12.5	4 x ADCP-Buoy mounted, downward looking (bin height of 5 or 6 m depth) C090	Dual Radar, complex current magnitude (phase - degrees)	0.90(−3.1)	13.0	
				D090		0.86(−4.2)	14.1	
				D130		0.89(0.79)	15.2	
				E090		0.78(29.1)	19.1	
				C090	Along-Shore	0.89	10.1	20 (E)
				D090		0.86	12.1	
				D130		0.91	11.7	
				E090		0.87	11.4	
				C090	Cross-Shore	0.92	8.2	20 (E)
				D090		0.85	7.3	
				D130		0.83	9.6	
				E090		0.84	15.4	
Paduan et al. (2006) Monterey Bay	SeaSonde CODAR	S.C.	13	ADCP /Drifters (Downward looking) ADCP measurements 12 – 20 m below surface	Radial Currents	0.62 / 0.74	18.1 / 12.7	25 (E)
		N.P.S.	13			0.57 / 0.79	17.6 / 10.4	
		P.P.	13			0.62 / 0.77	16.6 / 10.4	
		M.L	25			0.34 / 0.72	12.4 / 10	
Ebuchi et al. (2006) Soya Strait	SeaSonde CODAR	SY	13.95	Drifter Buoy	Radial Currents	0.85	16.2	30 (E)
		SR				0.87	15.6	35 (E)
		NS				0.34	24.6	20 (E)
		SY - SR			Current vectors Zonal	0.84	17.5	Zonal 50 (E) Meridional 30 (E)
					Current vectors Meridional	0.71	19.6	
		SY		Shipboard ADCP 5 – 10 m below surface	Radial Currents	0.77	26.6	
		SR				0.85	25.2	
		NS				0.38	36.6	
		SY - SR			Current vectors Zonal	0.79	22.4	
					Current vectors Meridional	0.73	25.0	

Table 1 continued

Reference	Radar	Location	Frequency (MHz)	Mooring Type	Measurement Details	r	RMSD (cm/s)	Mean current speed (cm/s) (direction deg)
Teague et al. (2001) Chesapeak bay	MFCR	C.B	4.8	ADCP	u	0.87	8.1	$\approx 25(E)$
					v		13.3	
			13.4		u	0.92	6.9	$\approx 25(E)$
					v		6.3	
Emery at al. (2004) Santa Maria Basin	CODAR	RFG	13	ADCP	Radial Currents	0.5	12	20 (E)
		COP				0.6	11	20 (E)
Howarth et al. (2007)	WERA	L.B.	13	ADCP A_{ab3}	Dual radar complex current measurement (phase degrees)	0.93(0.8)	-	ADCP / Radar
				ADCP A_{ab18}		0.94(1.5)	-	$3(-8)$ / $5(32)$
				ADCP B_{ab3}		0.92(5.4)	-	
				ADCP B_{ab18}		0.93(6.9)	-	$4(8)$ / $6(35)$

note:

---

r is the correlation coefficient between the radars and moored current meters or ADCP's and RMSD is the root mean square difference. θ is in reference to direction and is given in degrees. Mean current speeds are given where possible, however some are estimated (E) from current plots and should be treated with caution. Locations are Santa Cruz, SC, Moss Landing, ML, Points Pinos, PP, Chesapeak Bay, CB, Cape Hatteras, CH,West Florida Shelf,WFS, Refugio Beach, RFG, Coal Oil Point, COP, Santa Maria Basin, SM, Naval Postgraduate School, NPS, Bogega Marine Lab, BML, Point Reyes, PR, Noshappu, NS, Soya, SY, Sarufutsu, SR, and Liverpool Bay, LB. Radars are Ocean Surface Current Radar, OSCR, Coastal Ocean Dynamics Applications Radar, CODAR, Multi-Frequency Coastal Radar and WEllan RAdar,WERA.

Acronyms and Symbols

Acronyms

ADCP	Acoustic Doppler Current Profiler
BBWF	Burbo Bank Wind Farm
CEFAS	Centre for Environment, Fisheries and Aquaculture Science
CODAR	Coastal Ocean Dynamics Application Radar
dB	Deci Bels
DFT	Discrete Fourier Transform
EM	ElectroMagnetic
Fby	Formby radar
FFT	Fast Fourier Transform
FMCW	Frequency Modulated Continuous Wave
FMICW	Frequency Modulated Interrupted Continuous Wave
fwt	wind turbine modulation frequency
GLOSS	Global Sea Level Observing System
GYMWF	Gwynt y Mor Wind Farm
HF	High Frequency
Hz	Hertz (cycles per second)
LBCO	Liverpool Bay Coastal Observatory
Ldl	Llanddulas radar
MTI	Moving Target Indicator
NAE	North Atlantic European
NOAA	National Oceanic and Atmospheric Administration
NOC	National Oceanography Centre
NOCL	National Oceanography Centre Liverpool
NOCS	National Oceanography Centre Southampton
NHWF	North Hoyle Wind Farm
NERC	Natural Environmental Research Council
NMMP	National Marine Monitoring Programme
OSCR	Ocean Surface Current Radar
POL	Proudman Oceanography Centre
POLCOMS	Proudman Oceanography Centre Coastal Ocean Modelling System
Radar	RAdio Detection and Ranging
RCS	Radar Cross Section (sigma)
RFI	Radio Frequency Interference
RFWF	Rhyl Flats Wind Farm
rmsd	Root mean square difference
SCAWVEX	Surface Current and Wave Variability EXperiment
SNR	Signal to Noise Ratio
WERA	WEllan RAdar
WTI	Wind Turbine Interference

Symbols

A	Amplitude
ab	Above bed
b	Bandwidth
bs	Below Surface
c	Speed of light
c_p	Phase velocity
D	Antenna spacing
E_s	Scattered electric field strength
f	Frequency
g	Acceleration due to gravity ($9.81\ \mathrm{m/s^2}$) G_t Antenna gain
h	Water depth
H	Ocean wave height
Hs	Significant wave height
$\boldsymbol{k}$	Wave vector
λ	Wavelength
P_t	Power of pulse transmitted by the radar
r	Correlation
R_{max}	Maximum radar range
S_{min}	Minimum detectable signal
σ	radar cross section
T	Wave period
T_1	First moment period
T_1	Peak period
u	East current vector
v	North current vector
v	wave speed
ω_b	Bragg frequency

References

Note: A page number where the citation has been used follows each reference, e.g. pages 5.

ABASCAL, A.J., CASTANEDO, S., MEDINA, R., LOSADA, I.J. & ALVAREZ-FANJUL, E. (2009). Application of HF radar currents to oil spill modelling. *Marine Pollution Bulletin*, **58**, 238–248. pages 3

AUSTIN, B.A. (1999). Precursors to radar - the Watson-Watt memorandum and the Daventry experiment. *International Journal of Electrical Engineering Education*, **36**, 365–372. pages 8

BARBER, N.F., URSELL, F., DARBYSHIRE, J. & TUCKER, M.J. (1945). A frequency analyser used in the study of ocean waves. *Nature*, **158**, 329–332. pages 16

BARRICK, D.E. (1972a). First-order theory and analysis of MF/HF/VHF scatter from the sea. *IEEE Transactions on Antennas and Propagation*, **20**, 2–10. pages 3, 16, 22, 25

BARRICK, D.E. (1972b). Remote sensing of sea state by radar. *Remote Sensing of the Troposphere*, 1–46. pages 3

BARRICK, D.E. (1973). FM/CW radar signals and digital processing. Tech. rep., National Oceanic and Atmospheric Administration, technical Report REL 283-WPL 26. pages 3

BARRICK, D.E. & WEBER, B. (1977). On the nonlinear theory for gravity waves on the ocean surface. part 2: Interpretation and applications. *Journal of Physical Oceanography*, **7**, 11–21. pages 22

BARRICK, D.E., EVANS, M.W. & WEBER, B. (1977). Ocean surface currents mapped by radar. *Science*, **198**, 138–144. pages 9

BUTLER, M.M. (2003). Feasibility of mitigating the effects of windfarms on primary radar. *Alenia Marconi Systems Limited, DTI PUB URN No 03/976*. pages 6, 10, 13

CEFAS (2004). UK National Marine Monitoring Programme - Second Report(1999-2001) - http://jncc.defra.gov.uk/pdf/nmmp2ndreport.pdf. pages 1

CEFAS (2011). Cefas website: http://www.cefas.defra.gov.uk. Accessed July 2011. pages 2

CHAPMAN, R.D. & GRABER, H.C. (1997). Validation of HF radar measurements. *Oceanography*, **10**, 76–79. pages 77

CHRISTIANSEN, M.B. & HASAGER, C.B. (2005). Wake effects of large offshore wind farms identified from satellite SAR. *Remote Sensing of Environment*, **98**, 251–268. pages 6

COS (2010a). Codar Ocean Sensors - A look back in time... the birth of CODAR at NOAA: hhtp//www.codar.com. pages 25

COS (2010b). Codar Ocean Sensors - SeaSonde General Specification: http://www.codar.com/. pages 26

CROMBIE, D.D. (1955). Doppler spectrum of sea echo at 13.56 Mc./s. *Nature*, **175**, 681–682. pages 3, 16

CROMBIE, D.D. (1971). Backscatter of HF radio waves from the sea. *Electromagnetic Probing in Geophysics, J.R. Wait, ed.*, 131–162. pages 3

DYBDAL, R.B. (1987). Radar cross section measurements. *IEEE Trans. on Antennas and Propagation*, **75**. pages 11

DZVONKOVSKAYA, A., GURGEL, K.W., ROHLING, H. & SCHLICK, T. (2009). HF radar WERA application for ship detection and tracking. *European Journal of Navigation*, **7**, 18–25. pages 3, 26

EBUCHI, N., FUKAMACHI, Y., OHSHIMA, K.I., SHIRASAWA, K., ISHIKAWA, M., TAKATSUKA, T., DAIBO, T. & WAKATSUCHI, M. (2006). Observation of the Soya warm current using HF ocean radar. *Journal of Oceanography*, **62**, 47–61. pages 59, 66, 68

EMERY, B.M., WASHBURN, L. & HARLAN, J.A. (2004). Evaluating radial current measurements from CODAR high-frequency radars with moored current meters. *Journal of Atmospheric and Oceanic Technology*, **21**, 1259–1271. pages 70

EMERY, W.J. & THOMSON, R.E. (2001). *Data Analysis Methods in Physical Oceanography*. Elsevier, Amsterdam, 2nd edn. pages 30, 58, 59

FERNANDEZ, D.M. & PADUAN, J.D. (1996). Simultaneous CODAR and OSCR measurements of ocean surface currents in monterey bay. *Proceedings, IEEE IGARSS'96, Lincoln, NE,*, **3**, 1749–1752. pages 26, 70, 72

GOMMENGINGER, C.P., WARD, N.P., FISHER, G.J., ROBINSON, I.S. & BOXALL, S.R. (2000). Quantitative microwave backscatter measurements from the ocean surface using digital marine radar images. *Journal of Atmospheric and Ocean Technology*, **17**, 665–678. pages 11

GRABER, H.C., HAUS, B.K., CHAPMAN, R.D. & SHAY, L.K. (1997). HF radar comparisons with moored estimates of current speed and direction: Expected differences and implications. *Journal of Geophysical Research*, **102**, 18,749–18,766. pages 2, 59

GURGEL, K.W. & ANTONISCHKI, G. (1997). Remote Sensing of Surface Currents and Waves by the HF Radar WERA. *IEE Proceedings, Electronic Engineering in Oceanography*, **439**, 211–217. pages 26

GURGEL, K.W., ANTONISCHKI, G., ESSEN, H.H. & SCHLICK, T. (1999a). Wellen radar (WERA): a new ground-wave HF radar for ocean remote sensing. *Coastal Engineering*, **37**, 219–234. pages 9, 26, 27, 28, 29, 31

GURGEL, K.W., ESSEN, H.H. & KINGSLEY, S.P. (1999b). High-frequency radars: physical limitations and recent developments. *Coastal Engineering*, **37**, 201–218. pages 30

HAUS, B.K., GRABER, H.C. & SHAY, L.K. (1997). Synoptic measurement of dynamic oceanic features. *Oceanography*, **10**, 45–48. pages 3

HAUSER, D., KAHMA, K., KROGSTAD, H.E., LEHNER, S., MONBALIU, J. & WYATT, L.R. (2005). *Measuring and analysing the directional spectrum of ocean waves, COST Action 714, Working Group 3*. COST. pages 20, 21, 22, 23

HAWKES, P.J., ATKINS, R., BRAMPTON, A.H., FORTUNE, D., GARBETT, R. & B. P, G. (2001). Wavenet: Nearshore wave recording network for England and Wales. *Feasibility Study. HR Wallingford Report TR 122 April 2001.*. pages 41

HELZEL, T., MARRIETTE, V. & PAVEC, M. (2010). Coastal radar 'WERA', a tool for harbour management. *European Journal of Navigation*, **8**. pages 3

HELZEL, T., KNIEPHOFF, M., PETERSEN, L., MARIETTE, V. & THOMAS, N. (2011). Accuracy and reliability of ocean radar WERA in beam forming or direction finding mode. IEEE CWTMC Workshop Monterey. pages 26

HERON, M.L. & HERON, S.F. (2001). Cumulative probability noise analysis in geophsical spectral records. *International Journal of Remote Sensing*, **22**, 2537–2544. pages 15

HILDEBRAND, P.H. & SEKHON, R.S. (1974). Objective determination of the noise level in doppler spectra. *IEEE Journal of Oceanic Engineering*, **18**, 296–305. pages 15

HOLDEN, G.J. & WYATT, L.R. (1992). Measurement of ocean wave spectra using narrow beam HF radar. *Journal of Applied Meteorology*, **13**, 808–811. pages 22, 24

HOLT, J.T. & JAMES, I.D. (2001). An s coordinate density evolving model of the northwest European continental shelf: 1. model description and density structure. *Journal of Geophysical Research*, **106**, 14,015–14,034. pages 2

HOWARD, M. & BROWN, C. (2004). Results of the electromagnetic investigations and assessments of marine radar, communications and positioning systems undertaken at the North Hoyle wind farm by QinetiQ and the Maritime and Coastguard Agency. *QINETIQ/03/00297/1.1 Contract Number MCA MNA 53/10/366*. pages 7

HOWARTH, M.J., PROCTOR, R., KNIGHT, P.J. & SMITHSON, M.J. (2006). The Liverpool Bay Coastal Observatory-towards the goals. *Proceedings of Oceans 2006, 18-21 September, Boston IEEE, pp6.*. pages 42

HOWARTH, M.J., PLAYER, R.J., WOLF, J. & A.SIDDONS, L. (2007). HF radar measurements in Liverpool Bay, Irish Sea. *Proceedings of Oceans2007, 18-21 June, Aberdeen IEEE, pp6*. pages 2, 42, 43, 57, 59, 63, 73, 74, 78, 79, 85, 88

HULBURT, E.O. (1957). Variations of the ionosphere and of the solar intensity with sunspots. *Geophysics*, **43**, 92–95. pages 47

JONES, W., SCHROEDER, L. & MITCHELL, J. (1997). Aircraft measurements of the microwave scattering signature of the ocean. *IEEE Transactions*, **AP-25**, 52–61. pages 11

KAPLAN, D.M., LARGIER, J. & BOTSFORD, L.W. (2005). HF radar observations of surface circulation off Bodega Bay (northern California, USA). *Journal of Geophysical Research*, **110**, C10020. pages 26, 43

KELLY, F.J., BONNER, S.J., PEREZ, J.C., TRUJILLO, D., WEISBERG, R.H., LUTHER, M.E. & HE, R. (2003). A comparison of near-surface current measurements by ADCP and HF-radar on the west Florida Shelf. *IEEE/OES Proceedings of the Seventh Working Conference on Current Measurement Technology AP-25(1)*, 52–61. pages 26, 43, 59

KENT, B.M., HILL, K.C., BUTERBAUGH, A., ZELINSKIL, G., HAWLEY, R., CRAVENS, L., TRI-VAN, VOGEL, C. & COVEYOU, T. (2008). Dynamic radar cross section and radar doppler measurements of commercial general electric windmill power turbines part 1: Predicted and measured radar signatures. *IEEE Antennas and Propagation Magazine*, **50**, 211–219. pages 6

KING, J.W., BENNET, F.D.G., BLACKE, R., ECCLES, D., GIBSON, A.J., HOWES, G.M. & SLATER, K. (1984). OSCR (ocean surface current radar) observations of currents off the coasts of Northern Ireland, England, Wales, and Scotland, in current measurements offshore, Proc. one-day conf., London, England. *Society of Underwater Technology*. pages 26

KJELAAS, A.G. & WHELAN, C. (2011). Rapidly deployable SeaSonde for modeling oil spill response. pages 3, 26

KRAUS, J. & FLEISCH, D. (1999). *Electromagnetics with Applications*. Chapter 5, Section 12, McGraw-Hill Book Co,Singapore (5). pages 9, 11

L. ZHANG, N.L.J.R., K. DING (2010). High-resolution RCS measurement inside an anechoic chamber. *International Forum on Information Technology and Applications*, **58**, 252–255. pages 11

LANE, A., KNIGHT, P.J. & PLAYER, R.J. (1999). Current measurement technology for near-shore waters. *Coastal Engineering*, **37**, 334–368. pages 42

LIPA, B.J. & BARRICK, D.E. (1986). Extraction of sea state from HF radar sea echo: Mathematical theory and modeling. *Radio Science*, **21**, 81–100. pages 23

LIU, Y., WEISBERG, R.H., MERZ, C.R., LICHTENWALNER, S. & KIRKPATRICK, G.J. (2010). HF radar performance in a low-energy environment: CODAR SeaSonde experience on the west Florida Shelf. *Journal of Atmospheric and Oceanic Technology*, **27**, 1689–1710. pages 82, 86, 135

MARIANO, A.J., KOURAFALOU, V.H., SRINIVASAN, A., KANG, H., HALLIWELL, G.R., RYAN, E.H. & ROFFER, M. (2011). On the modeling of the 2010 Gulf of Mexico oil spill. *Dynamics of Atmospheres and Oceans*, **52**, 322–340. pages 3

NAI, F., PALMER, R.D. & TORRES, S.M. (2011). Range-doppler domain signal processing to mitigate wind turbine clutter. *Radar Conference (RADAR), 2011 IEEE*, 1738–1741. pages 137

NOC (2011a). National Oceanography Centre Setting course: a community vision and priorities for marine research: http://noc.ac.uk/about-us/noc-association/vision-priorities. pages 1

NOC (2011b). Strategy 2009-2014, sea level and shelf sea science: Solutions for a sustainable future. *http://www.pol.ac.uk/home/documents/POL-Strategy.pdf*. pages 1, 2

OTT, M.W. (2002). An improvement in the calculation of ADCP velocities. *Journal of Atmospheric and Oceanic Technology*, **19**, 841–845. pages 42

PADUAN, J.D. & GRABER, H.C. (1997). Introduction to High-Frequency radar: Reality and myth. *Oceanography*, **10**, 36–39. pages 3, 72, 76

PADUAN, J.D. & ROSENFELD, L.K. (1996). Remotely sensed surface currents in Monterey Bay from shore based HF radar (Coastal Ocean Dynamics Application Radar). *Journal of Geophysical Research*, **101(C9)**, 669–686. pages 26, 72

PADUAN, J.D., KIM, K.C., COOK, M.S. & CHAVEZ, F.P. (2006). Calibration and validation of direction-finding high-frequency radar ocean surface current observations. *IEEE Journal of Oceanic Engineering*, **31**, 862–875. pages 70

POWER, D. & RANDELL, C. (1999). Coherent ultra high frequency(UHF) radar, new search and rescue initiatives fund, final report. Tech. rep., Contract report for the Department of Fisheries and Oceans, Canadian Coast Guard Search and Rescue, St. John's, Newfoundland, c-CORE Contract number 99-C33. pages 11

PRANDLE, D. (1985). Measuring currents at the sea surface by HF radar (OSCR). *Underwater Technology*, **11**, 25–27. pages 26

PRANDLE, D. (1987). The fine-structure of nearshore tidal and residual circulations revealed by H.F. radar surface current measurements. *American Meteorological Society*, **17**, 231–245. pages 59, 65

PRANDLE, D. (1991). A new view of near-shore dynamics based on observations from HF radar. *Progressive Oceanography*, **27**, 403–438. pages 57, 75, 77

PUGH, D.T. (1996). *Tides, Surges and Mean Sea-Level*. John Wiley and Sons, Chichester, 2nd edn. pages 57, 59

RABNIER, L.R. & GOLD, B. (1975). *Theory and Application of Digital Signal Processing*. Prentice-Hall, INC. Englewood Cliffs, New Jersey. pages 61

RADOCK, D.R. (1999). Mahidol Physics Education Centre. pages 58

RICKARDS, L. (2001). *The UK National Tide Gauge Network*. British Oceanographic Data Centre, UK. pages 2

RIDDOLLS, R.J. (2005). Effects of wind turbines on high frequency surface wave radar. Tech. rep., Defence R & D Canada. pages ix, 6, 14, 94, 95, 96

ROBINSON, A., WYATT, L.R. & HOWARTH, M. (2011). A two year comparison between HF radar and ADCP current measurements in Liverpool Bay. *Journal of Operational Oceanography*, **4**, 33–45. pages 6, 42, 43, 59, 63, 70, 78, 80, 82, 83, 84, 85, 93, 98, 115, 134

ROBINSON, A., WYATT, L.R. & HOWARTH, M. (2013). HF radar data availability and measurement accuracy in Liverpool Bay before and after the construction of Rhyl-Flats wind farm. *Journal of Operational Oceanography*, **8**, 33–45. pages 6, 81, 93, 98, 109, 121, 126, 129, 130, 131

SHEARMAN, E.D.R. & MOORHEAD, M.D. (1988). Pisces: A coastal groundwave radar for current, wind and wave mapping to 200km ranges. *IGRASS'88 proceedings*. pages 9, 26

SKOLNIK, M. (1990). *Radar Handbook*. McGraw-Hill Publishing Company, New York, 2nd edn. pages 10, 11, 12

STEWART, R.H. & JOY, J.W. (1974). HF radio measurements of ocean surface currents. *Deep Sea Research*, **21**, 1039–1049. pages 24

TEAGUE, C.C., VESECKY, J.F. & HALLOCK, Z.R. (2001). A comparison of multifrequency HF radar and ADCP measurements of near-surface currents during COPE-3. *Journal of Oceanic Engineering*, **26**, 399–405. pages 41, 72

TENNANT, A. & CHANBERS, B. (2006). Signature management of radar returns from wind turbine generators. *Smart Materials and Structures*, **15**, 468–472. pages 15, 95, 96

TICE, T.E. (1990). An overview of radar cross section measurement techniques. *Instrumentation and Measurement, IEEE Transactions*, **39**, 205–207. pages 11

TRINZA, D.B. & JENSEN, R.E. (1997). High-Frequency radar remote sensing: The new revolution in coastal oceanography. *Oceanography*, **10**, 34. pages 3

TUCKER, M.J. (2000). Recommended standard for wave data sampleing and near-real-time processing. *Ocean Engineering*, **20**, 459–474. pages 25

VALENTIN, M., HELZEL, T., MARIETTE, V. & THOMAS, N. (2010). Coastal radar WERA, a tool for search and rescue and oil spill management. *US/EU Baltic 2010, Riga, International Symposium (BALTIC 2010)*. pages 3

WARD, J.F. (1969). Power spectra from ocean movements measured remotely by ionospheric radio backscatter. *Nature*, **223**, 1335–1330. pages 3

WEBER, B. & BARRICK, D.E. (1977). On the nonlinear theory for gravity waves on the oceans surface. part I: Derivations. *Journal of Physical Oceanography*, **7**, 3–10. pages 22

WOLF, J., OSUNA, P., HOWARTH, M.J. & SOUZA, A. (2007). Modelling and measuring waves in coastal waters. *Proceedings of ICCE 2006, San Diego*, **1**, 539–551. pages 43, 88

WOODWORTH, P.L. & SMITH, D.E. (2003). A one year comparison of radar and bubbler tide gauges at Liverpool. *International Hydrographic Review*, **4**. pages 2

WYATT, L.R. (1990). Progress in the interpretation of HF sea echo: HF radar as a remote sensing tool. *IEE Proceedings*, **137**, 139–148, part F. pages 26

WYATT, L.R. (2002). An evaluation of wave parameters measured using a single HF radar system. *Can. J. Remote Sensing*, **28**, 205–218. pages 3

WYATT, L.R. (2006). Monitoring waves, currents and winds with phased-array HF radar. *Workshop on Monitoring Techniques for Marine Wnvironment, Taiwan, 27/10/2006*. pages 3

WYATT, L.R. & GREEN, J.J. (2002). The availability and accuracy of HF radar wave measurements. *Proceedings of IGARSS'02, Toronto, Canada, June 24-28 2002*, 515–517. pages 43

WYATT, L.R. & GREEN, J.J. (2009). Measuring high and low waves with HF radar. *Proceedings of IEEE Oceans Conference, Bremen*. pages 3, 43

WYATT, L.R., GURGEL, K.W., KROGSTAD, H.E., PETERS, H.C., PRANDLE, D. & WENSINK, G.J. (1995). Surface Current and Wave Variability Experiments (SCAWVEX). *Second MAST days and Euromar Market, Sorrento, 7-10 Nov 1995, Project Reports, Volume 1*, 153–185. pages 26

WYATT, L.R., GREEN, J.J., GRUGEL, K.W., BORGE, J.C.N., REICHERT, K., HESSNER, K., GUNTHER, H., ROSENTHAL, W., SAETRA, O. & REISTAD, M. (2003). Validation and intercomparisons of wave measurements and models during the EuroROSE experiments. *Coastal Engineering*, **48**, 1–28. pages 3, 43

WYATT, L.R., GREEN, J.J., MIDDLEDITCH, A., MOORHEAD, M.D., HOWARTH, J., HOLT, M. & KEOGH, S. (2006). Operational wave, current, and wind measurements with the Pisces HF radar. *IEEE Journal of Oceanic Engineering*, **31**, 819–834. pages 1, 3, 26, 43

WYATT, L.R., GREEN, J.J. & MIDDLEDITCH, A. (2011). HF radar data quality requirements for wave measurement. *Coastal Engineering*, **58**, 327–336. pages 3, 88

YOUNG, D.H. & FREEDMAN, R.A. (2000). *University Physics, with Modern Physics*. Addison-Wesley series in physics, Addison-Wesley, New York, 10th edn. pages 9, 19